

1 SEARCH FOR PRODUCTION OF A HIGGS BOSON AND A SINGLE TOP
2 QUARK IN MULTILEPTON FINAL STATES IN pp COLLISIONS AT $\sqrt{s} = 13$
3 TeV.

4 by

5 Jose Andres Monroy MontaÑez

6 A DISSERTATION

7 Presented to the Faculty of

8 The Graduate College at the University of Nebraska

In Partial Fulfilment of Requirements

10 For the Degree of Doctor of Philosophy

11 Major: Physics and Astronomy

12 Under the Supervision of Kenneth Bloom and Aaron Dominguez

13 Lincoln, Nebraska

14 July, 2018

15 SEARCH FOR PRODUCTION OF A HIGGS BOSON AND A SINGLE TOP
16 QUARK IN MULTILEPTON FINAL STATES IN pp COLLISIONS AT $\sqrt{s} = 13$
17 TeV.

18 Jose Andres Monroy Montañez, Ph.D.
19 University of Nebraska, 2018

20 Adviser: Kenneth Bloom and Aaron Dominguez

₂₁ Table of Contents

₂₂ Table of Contents	iii
₂₃ List of Figures	vii
₂₄ List of Tables	x
₂₅ 1 INTRODUCTION	1
₂₆ 2 Theoretical approach	2
₂₇ 2.1 Introduction	2
₂₈ 2.2 Standard model of particle physics	3
₂₉ 2.2.1 Fermions	5
₃₀ 2.2.1.1 Leptons	6
₃₁ 2.2.1.2 Quarks	8
₃₂ 2.2.2 Fundamental interactions	12
₃₃ 2.2.3 Gauge invariance.	15
₃₄ 2.2.4 Gauge bosons	18
₃₅ 2.3 Electroweak unification and the Higgs mechanism	19
₃₆ 2.3.1 Spontaneous symmetry breaking (SSB)	27
₃₇ 2.3.2 Higgs mechanism	31

38	2.3.3	Masses of the gauge bosons	34
39	2.3.4	Masses of the fermions	35
40	2.3.5	The Higgs field	36
41	2.3.6	Production of Higgs bosons at LHC	37
42	2.3.7	Higgs boson decay channels	41
43	2.4	Experimental status of the anomalous Higgs-fermion coupling	42
44	2.5	Associated production of a Higgs boson and a single top quark	44
45	2.6	CP-mixing in tH processes	49
46	3	The CMS experiment at the LHC	54
47	3.1	Introduction	54
48	3.2	The LHC	55
49	3.3	The CMS experiment	65
50	3.3.1	Coordinate system	67
51	3.3.2	Pixels detector	68
52	3.3.3	Silicon strip tracker	70
53	3.3.4	Electromagnetic calorimeter	72
54	3.3.5	Hadronic calorimeter	73
55	3.3.6	Superconducting solenoid magnet	75
56	3.3.7	Muon system	76
57	3.3.8	CMS trigger system	77
58	3.3.9	CMS computing	79
59	4	Event generation, simulation and reconstruction	83
60	4.1	Event generation	84
61	4.2	Monte Carlo Event Generators.	88
62	4.3	CMS detector simulation.	89

63	4.4 Event reconstruction	91
64	4.4.1 Particle-Flow Algorithm.	91
65	4.4.1.1 Missing transverse energy.	103
66	4.4.2 Event reconstruction examples	104
67	5 Statistical methods	107
68	5.1 Multivariate analysis	107
69	5.1.1 Decision trees	110
70	5.1.2 Boosted decision trees (BDT).	113
71	5.1.3 Overtraining.	116
72	5.1.4 Variable ranking.	116
73	5.1.5 BDT output example.	117
74	5.2 Statistical inference.	118
75	5.2.1 Nuisance parameters.	118
76	5.2.2 Maximum likelihood estimation method	119
77	5.2.3 Hypothesis test	120
78	5.3 exclusion limits	121
79	5.4 asymptotic limits	121
80	6 Search for production of a Higgs boson and a single top quark in multilepton final states in pp collisions at $\sqrt{s} = 13$ TeV	122
82	6.1 Introduction	122
83	6.2 tHq signature	124
84	6.3 Background processes	126
85	6.4 Data and MC Samples	128
86	6.4.1 Full 2016 dataset and MC samples	128
87	6.4.2 Triggers	129

88	6.5 Object Identification	133
89	6.5.1 Jets and b -jet tagging.	133
90	6.5.2 Missing Energy MET.	134
91	6.5.3 Lepton reconstruction and identification	135
92	6.5.4 Lepton selection efficiency	143
93	6.6 Event selection	145
94	6.7 Background predictions	146
95	6.8 Signal discrimination	148
96	6.8.1 Classifiers response	150
97	6.9 Additional discriminating variables	154
98	Bibliography	156
99	References	158

¹⁰⁰ List of Figures

101	2.1 Standard Model of particle physics.	4
102	2.2 Transformations between quarks	12
103	2.3 Fundamental interactions in nature.	13
104	2.4 SM interactions diagrams	14
105	2.5 Neutral current processes	20
106	2.6 Spontaneous symmetry breaking mechanism	28
107	2.7 SSB Potential form	29
108	2.8 Potential for complex scalar field	30
109	2.9 SSB mechanism for complex scalar field	31
110	2.10 Proton-Proton collision	37
111	2.11 Higgs boson production mechanism Feynman diagrams	39
112	2.12 Higgs boson production cross section and decay branching ratios	40
113	2.13 Two dimensional κ_t - κ_V plot of the coupling modifiers. ATLAS and CMS combination.	43
115	2.14 Higgs boson production in association with a top quark mechanism Feyn- man diagrams	45
117	2.15 Cross section for tHq process as a function of κ_t	48
118	2.16 Cross section for tHW process as a function of κ_{Htt}	48

119	2.17 NLO cross section for tX_0 and $t\bar{t}X_0$.	52
120	2.18 NLO cross section for tWX_0 , $t\bar{t}X_0$.	53
121	3.1 CERN accelerator complex	55
122	3.2 LHC protons source. First acceleration stage.	56
123	3.3 The LINAC2 accelerating system at CERN.	57
124	3.4 LHC layout and RF cavities module.	58
125	3.5 LHC dipole magnet.	60
126	3.6 Integrated luminosity delivered by LHC and recorded by CMS during 2016	62
127	3.7 LHC interaction points	64
128	3.8 Multiple pp collision bunch crossing at CMS.	65
129	3.9 Layout of the CMS detector	66
130	3.10 CMS detector coordinate system	67
131	3.11 CMS pixel detector schematic view.	70
132	3.12 SST Schematic view.	71
133	3.13 CMS ECAL schematic view	72
134	3.14 CMS HCAL schematic view	74
135	3.15 CMS solenoid magnet	75
136	3.16 CMS Muon system schematic view	76
137	3.17 CMS Level-1 trigger architecture	78
138	3.18 WLCG structure	80
139	3.19 Data flow from CMS detector through hardware Tiers	82
140	4.1 Event generation process.	84
141	4.2 Particle flow algorithm.	92
142	4.3 Jet reconstruction.	100
143	4.4 Jet energy corrections.	101

144	4.5	Secondary vertex in a b-hadron decay.	102
145	4.6	HIG-13-004 Event 1 reconstruction.	104
146	4.7	$e\mu$ event reconstruction.	105
147	4.8	Recorded event reconstruction.	106
148	5.1	Scatter plots-MVA event classification.	109
149	5.2	Scalar test statistical.	109
150	5.3	Decision tree.	111
151	5.4	Decision tree output example.	114
152	5.5	BDT output example.	117
153	6.1	tHq event signature.	125
154	6.2	$t\bar{t}$ and $t\bar{t}W$ events signature.	127
155	6.3	Tight vs loose lepton selection efficiencies in the 2lss channel.	143
156	6.4	Tight vs loose lepton selection efficiencies in the 3l channel.	144
157	6.5	Input variables to the BDT for signal discrimination normalized.	149
158	6.6	Input variables to the BDT for signal discrimination not normalized.	151
159	6.7	BDT inputs as seen by TMVA against $t\bar{t}$.	152
160	6.8	BDT inputs as seen by TMVA against $t\bar{t}V$.	153
161	6.9	Correlation matrices for the input variables in the TMVA.	154
162	6.10	MVA classifiers performance.	154
163	6.11	Additional discriminating variables distributions.	156

¹⁶⁴ List of Tables

165	2.1	Fermions of the SM.	5
166	2.2	Fermion masses.	6
167	2.3	Lepton properties.	8
168	2.4	Quark properties.	9
169	2.5	Fermion weak isospin and weak hypercharge multiplets.	11
170	2.6	Fundamental interactions features.	15
171	2.7	SM gauge bosons.	19
172	2.8	Higgs boson properties.	37
173	2.9	Predicted branching ratios for a SM Higgs boson with $m_H = 125 \text{ GeV}/c^2$	41
174	2.10	Predicted SM cross sections for tH production at $\sqrt{s} = 13 \text{ TeV}$	46
175	2.11	Predicted enhancement of the tHq and tHW cross sections at LHC	49
176	6.1	Signal samples and their cross section and branching fraction.	129
177	6.2	κ_V and κ_t combinations.	130
178	6.3	List of background samples used in this analysis (CMSSW 80X).	131
179	6.4	Leading-order $t\bar{t}W$ and $t\bar{t}Z$ samples used in the signal BDT training.	131
180	6.5	Table of high-level triggers that we consider in the analysis.	132
181	6.6	Trigger efficiency scale factors and associated uncertainties.	133
182	6.7	Effective areas, for electrons and muons.	139

183	6.8 Requirements on each of the three muon selections.	142
184	6.9 Criteria for each of the three electron selections.	142
185	6.10 MVA input discriminating variables	150
186	6.11 TMVA input variables ranking for BDTA_GRAD method	155
187	6.12 TMVA configuration used in the BDT training.	155
188	6.13 ROC-integral for all the testing cases.	157

¹⁸⁹ Chapter 1

¹⁹⁰ INTRODUCTION

₁₉₁ **Chapter 2**

₁₉₂ **Theoretical approach**

₁₉₃ **2.1 Introduction**

₁₉₄ The physical description of the universe is a challenge that physicists have faced by
₁₉₅ making theories that refine existing principles and proposing new ones in an attempt
₁₉₆ to embrace emerging facts and phenomena.

₁₉₇ At the end of 1940s Julian Schwinger [1] and Richard P. Feynman [2], based on
₁₉₈ the work of Sin-Itiro Tomonaga [3], developed an electromagnetic theory consistent
₁₉₉ with special relativity and quantum mechanics that describes how matter and light
₂₀₀ interact; the so-called *quantum electrodynamics* (QED) was born.

₂₀₁ QED has become the guide in the development of theories that describe the uni-
₂₀₂ verse. It was the first example of a quantum field theory (QFT), which is the theore-
₂₀₃ tical framework for building quantum mechanical models that describes particles and
₂₀₄ their interactions. QFT is composed of a set of mathematical tools that combines
₂₀₅ classical fields, special relativity and quantum mechanics, while keeping the quantum
₂₀₆ point particles and locality ideas.

₂₀₇ This chapter gives an overview of the standard model of particle physics, starting

208 with a description of the particles and interactions that compose it, followed by a
 209 description of the electroweak interaction, the Higgs boson and the associated pro-
 210 duction of Higgs boson and a single top quark (tH). The description contained in
 211 this chapter is based on References [4–6].

212 2.2 Standard model of particle physics

213 Particle physics at the fundamental level is modeled in terms of a collection of inter-
 214 acting particles and fields in a theory known as the *standard model of particle physics*
 215 (*SM*). The full picture of the SM is composed of three fields¹ whose excitations are
 216 interpreted as particles called mediators or force-carriers, a set of fields whose excita-
 217 tions are interpreted as elementary particles interacting through the exchange of those
 218 mediators, and a field that gives the mass to elementary particles. Figure 2.1 shows
 219 the scheme of the SM particles’ organization. In addition, for each of the particles
 220 in the scheme there exists an antiparticle with the same mass and opposite quantum
 221 numbers. The existence of antiparticles is a prediction of the relativistic quantum
 222 mechanics from the solution of the Dirac equation for which a negative energy solu-
 223 tion is also possible. In some cases a particle is its own anti-particle, like photon or
 224 Higgs boson.

225 The mathematical formulation of the SM is based on group theory and the use of
 226 Noether’s theorem [8] which states that for a physical system modeled by a Lagrangian
 227 that is invariant under a group of transformations a conservation law is expected. For
 228 instance, a system described by a time-independent Lagrangian is invariant (symmet-
 229 ric) under time changes (transformations) with the total energy conservation law as

¹ The formal and complete treatment of the SM is out of the scope of this document, however a plenty of textbooks describing it at several levels are available in the literature. The treatment in References [5, 6] is quite comprehensive and detailed. Note that gravitational field is not included in the standard model formulation

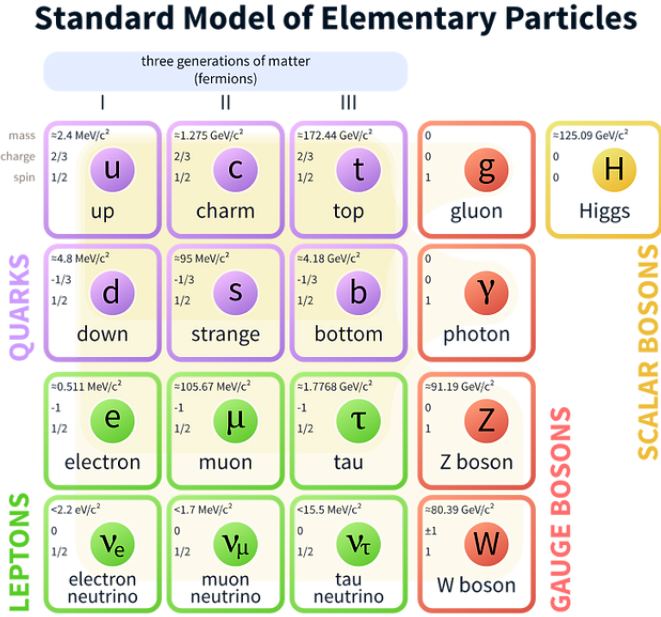


Figure 2.1: Schematic representation of the Standard Model of particle physics. The SM is a theoretical model intended to describe three of the four fundamental forces of the universe in terms of a set of particles and their interactions. [7].

the expected conservation law. In QED, the charge operator (Q) is the generator of the $U(1)$ symmetry which according to the Noether's theorem means that there is a conserved quantity; this conserved quantity is the electric charge and thus the law of conservation of electric charge is established.

In the SM, the symmetry group $SU(3)_C \otimes SU(2)_L \otimes U(1)_Y$ describes three of the four fundamental interactions in nature (see Section 2.2.2): strong interaction (SI), weak interaction (WI) and electromagnetic interactions (EI) in terms of symmetries associated to physical quantities:

- Strong: $SU(3)_C$ associated to color charge
 - Weak: $SU(2)_L$ associated to weak isospin and chirality
 - Electromagnetic: $U(1)_Y$ associated to weak hypercharge and electric charge

241 It will be shown that the electromagnetic and weak interactions are combined in
 242 the so-called electroweak interaction where chirality, hypercharge, weak isospin and
 243 electric charge are the central concepts.

244 **2.2.1 Fermions**

245 The basic constituents of the ordinary matter at the lowest level, which form the set
 246 of elementary particles in the SM formulation, are quarks and leptons. All of them
 247 have spin 1/2, therefore they are classified as fermions since they obey Fermi-Dirac
 248 statistics. There are six *flavors* of quarks and three of leptons organized in three
 249 generations, or families, as shown in Table 2.1.

		Generation		
		1st	2nd	3rd
Leptons	Charged	Electron (e)	Moun(μ)	Tau (τ)
	Neutral	Electron neutrino (ν_e)	Muon neutrino (ν_μ)	Tau neutrino (ν_τ)
Quarks	Up-type	Up (u)	Charm (c)	Top (t)
	Down-type	Down (d)	Strange (s)	Bottom (b)

Table 2.1: Fermions of the SM. There are six flavors of quarks and three of leptons, organized in three generations, or families, composed of two pairs of closely related particles. The close relationship is motivated by the fact that each pair of particles is a member of an $SU(2)_L$ doublet that has an associated invariance under isospin transformations. WI between leptons is limited to the members of the same generation; WI between quarks is not limited but greatly favored, to same generation members.

250

251 There is a mass hierarchy between generations (see Table 2.2), where the higher
 252 generation particles decays to the lower one, which can explain why the ordinary
 253 matter is made of particles from the first generation. In the SM, neutrinos are modeled
 254 as massless particles so they are not subject to this mass hierarchy; however, today it
 255 is known that neutrinos are massive so the hierarchy could be restated. The reason
 256 behind this mass hierarchy is one of the most important open questions in particle

257 physics, and it becomes more puzzling when noticing that the mass difference between
 258 first and second generation fermions is small compared to the mass difference with
 259 respect to the third generation.

Lepton	Mass (MeV/c ²)	Quark	Mass (MeV/c ²)
e	0.51	u	2.2
μ	105.65	c	1.28×10^3
τ	1776.86	t	173.1×10^3
ν_e	Unknown	d	4.7
ν_μ	Unknown	s	96
τ_μ	Unknown	b	4.18×10^3

Table 2.2: Fermion masses [9]. Generations differ by mass in a way that has been interpreted as a mass hierarchy. Approximate values with no uncertainties are used, for comparison purpose.

260

261 Usually, the second and third generation fermions are produced in high energy
 262 processes, like the ones recreated in particle accelerators.

263 2.2.1.1 Leptons

264 A lepton is an elementary particle that is not subject to the SI. As seen in Table 2.1,
 265 there are two types of leptons, the charged ones (electron, muon and tau) and the
 266 neutral ones (the three neutrinos). The electric charge (Q) is the property that gives
 267 leptons the ability to participate in the EI. From the classical point of view, Q plays
 268 a central role determining, among others, the strength of the electric field through
 269 which the electromagnetic force is exerted. It is clear that neutrinos are not affected
 270 by EI because they don't carry electric charge.

271 Another feature of the leptons that is fundamental in the mathematical description
 272 of the SM is the chirality, which is closely related to spin and helicity. Helicity
 273 defines the handedness of a particle by relating its spin and momentum such that

274 if they are parallel then the particle is right-handed; if spin and momentum are
 275 antiparallel the particle is said to be left-handed. The study of parity conservation
 276 (or violation) in β -decay has shown that only left-handed electrons/neutrinos or right-
 277 handed positrons/anti-neutrinos are created [10]; the inclusion of that feature in the
 278 theory was achieved by using projection operators for helicity, however, helicity is
 279 frame dependent for massive particles which makes it not Lorentz invariant and then
 280 another related attribute has to be used: *chirality*.

281 Chirality is a purely quantum attribute which makes it not so easy to describe in
 282 graphical terms but it defines how the wave function of a particle transforms under
 283 certain rotations. As with helicity, there are two chiral states, left-handed chiral (L)
 284 and right-handed chiral (R). In the highly relativistic limit where $E \approx p \gg m$ helicity
 285 and chirality converge, becoming exactly the same for massless particles.

286 In the following, when referring to left-handed (right-handed) it will mean left-
 287 handed chiral (right-handed chiral). The fundamental fact about chirality is that
 288 while EI and SI are not sensitive to chirality, in WI left-handed and right-handed
 289 fermions are treated asymmetrically, such that only left-handed fermions and right-
 290 handed anti-fermions are allowed to couple to WI mediators, which is a violation of
 291 parity. The way to translate this statement in a formal mathematical formulation is
 292 based on the isospin symmetry group $SU(2)_L$.

293 Each generation of leptons is seen as a weak isospin doublet.² The left-handed
 294 charged lepton and its associated left-handed neutrino are arranged in doublets of
 295 weak isospin $T=1/2$ while their right-handed partners are singlets:

$$\begin{pmatrix} \nu_l \\ l \end{pmatrix}_L, l_R := \begin{pmatrix} \nu_e \\ e \end{pmatrix}_L, \begin{pmatrix} \nu_\mu \\ \mu \end{pmatrix}_L, \begin{pmatrix} \nu_\tau \\ \tau \end{pmatrix}_L, e_R, \mu_R, \tau_R, \nu_{eR}, \nu_{\mu R}, \nu_{\tau R} \quad (2.1)$$

² The weak isospin is an analogy of the isospin symmetry in strong interaction where neutron and proton are affected equally by strong force but differ in their charge.

296 The isospin third component refers to the eigenvalues of the weak isospin operator
 297 which for doublets is $T_3 = \pm 1/2$, while for singlets it is $T_3 = 0$. The physical meaning
 298 of this doublet-singlet arrangement falls in that the WI couples the two particles in
 299 the doublet by exchanging the interaction mediator while the singlet member is not
 300 involved in WI. The main properties of the leptons are summarized in Table 2.3.

301 Although all three flavor neutrinos have been observed, their masses remain un-
 302 known and only some estimations have been made [11]. The main reason is that
 303 the flavor eigenstates are not the same as the mass eigenstates which implies that
 304 when a neutrino is created its mass state is a linear combination of the three mass
 305 eigenstates and experiments can only probe the squared difference of the masses. The
 306 Pontecorvo-Maki-Nakagawa-Sakata (PMNS) mixing matrix encodes the relationship
 307 between flavor and mass eigenstates.

Lepton	$Q(e)$	T_3	L_e	L_μ	L_τ	Lifetime (s)
Electron (e)	-1	-1/2	1	0	0	Stable
Electron neutrino(ν_e)	0	1/2	1	0	0	Unknown
Muon (μ)	-1	-1/2	0	1	0	2.19×10^{-6}
Muon neutrino (ν_μ)	0	1/2	0	1	0	Unknown
Tau (τ)	-1	-1/2	0	0	1	290.3×10^{-15}
Tau neutrino (τ_μ)	0	1/2	0	0	1	Unknown

Table 2.3: Lepton properties [9]. Q: electric charge, T_3 : weak isospin. Only left-handed leptons and right-handed anti-leptons participate in the WI. Anti-particles with inverted T_3 , Q and lepton number complete the leptons set but are not listed. Right-handed leptons and left-handed anti-leptons, neither listed, form weak isospin singlets with $T_3 = 0$ and do not take part in the weak interaction.

308

309 2.2.1.2 Quarks

310 Quarks are the basic constituents of protons and neutrons. The way quarks join to
 311 form bound states, called *hadrons*, is through the SI. Quarks are affected by all the

312 fundamental interactions which means that they carry all the four types of charges:
 313 color, electric charge, weak isospin and mass.

Flavor	$Q(e)$	I_3	T_3	B	C	S	T	B'	Y	Color
Up (u)	2/3	1/2	1/2	1/3	0	0	0	0	1/3	r,b,g
Charm (c)	2/3	0	1/2	1/3	1	0	0	0	4/3	r,b,g
Top(t)	2/3	0	1/2	1/3	0	0	1	0	4/3	r,b,g
Down(d)	-1/3	-1/2	-1/2	1/3	0	0	0	0	1/3	r,b,g
Strange(s)	-1/3	0	-1/2	1/3	0	-1	0	0	-2/3	r,b,g
Bottom(b)	-1/3	0	-1/2	1/3	0	0	0	-1	-2/3	r,b,g

Table 2.4: Quark properties [9]. Q : electric charge, I_3 : isospin, T_3 : weak isospin, B: baryon number, C: charmness, S: strangeness, T: topness, B' : bottomness, Y: hypercharge. Anti-quarks posses the same mass and spin as quarks but all charges (color, flavor numbers) have opposite sign.

314

315 Table 2.4 summarizes the features of quarks, among which the most remarkable
 316 is their fractional electric charge. Note that fractional charge is not a problem, given
 317 that quarks are not found isolated, but serves to explain how composed particles are
 318 formed out of two or more valence quarks³.

319 Color charge is responsible for the SI between quarks and is the symmetry ($SU(3)_C$)
 320 that defines the formalism to describe SI. There are three colors: red (r), blue (b)
 321 and green (g) and their corresponding three anti-colors; thus each quark carries one
 322 color unit while anti-quarks carries one anti-color unit. As explained in Section 2.2.2,
 323 quarks are not allowed to be isolated due to the color confinement effect, hence, their
 324 features have been studied indirectly by observing their bound states created when

- 325 • one quark with a color charge is attracted by an anti-quark with the correspond-
 326 ing anti-color charge forming a colorless particle called a *meson*.

³ Hadrons can contain an indefinite number of virtual quarks and gluons, known as the quark and gluon sea, but only the valence quarks determine hadrons' quantum numbers.

327 • three quarks (anti-quarks) with different color (anti-color) charges are attracted
 328 among them forming a colorless particle called a *baryon* (*anti-baryon*).

329 In practice, when a quark is left alone isolated a process called *hadronization* occurs
 330 where the quark emits gluons (see Section 2.2.4) which eventually will generate new
 331 quark-antiquark pairs and so on; those quarks will recombine to form hadrons that
 332 will decay into leptons. This proliferation of particles looks like a *jet* coming from
 333 the isolated quark. More details about the hadronization process and jet structure
 334 will be given in chapter4.

335 In the first version of the quark model (1964), M. Gell-Mann [12] and G. Zweig
 336 [13, 14] developed a consistent way to classify hadrons according to their properties.
 337 Only three quarks (u, d, s) were involved in a scheme in which all baryons have baryon
 338 number $B=1$ and therefore quarks have $B=1/3$; non-baryons have $B=0$. Baryon
 339 number is conserved in SI and EI which means that single quarks cannot be created
 340 but in pairs $q - \bar{q}$.

341 The scheme organizes baryons in a two-dimensional space (I_3 - Y); Y (hyper-
 342 charge) and I_3 (isospin) are quantum numbers related by the Gell-Mann-Nishijima
 343 formula [15, 16]:

$$Q = I_3 + \frac{Y}{2} \quad (2.2)$$

344 where $Y = B + S + C + T + B'$ are the quantum numbers listed in Table 2.4.

345 There are six quark flavors organized in three generations (see Table 2.1) fol-
 346 lowing a mass hierarchy which, again, implies that higher generations decay to first
 347 generation quarks.

	Quarks			T_3	Y_W	Leptons			T_3	Y_W
Doublets	$(\frac{u}{d'})_L$	$(\frac{c}{s'})_L$	$(\frac{t}{b'})_L$	$(\frac{1/2}{-1/2})$	$1/3$	$(\nu_e)_L$	$(\nu_\mu)_L$	$(\nu_\tau)_L$	$(\frac{1/2}{-1/2})$	-1
Singlets	u_R	c_R	t_R	0	$4/3$	ν_{eR}	$\nu_{\mu R}$	$\nu_{\tau R}$		
	d'_R	s'_R	b'_R	0	$-2/3$	e_R	μ_R	τ_R	0	-2

Table 2.5: Fermion weak isospin and weak hypercharge multiplets. Weak hypercharge is calculated through the Gell-Mann-Nishijima formula 2.2 but using the weak isospin and charge for quarks.

349 Isospin doublets of quarks are also defined (see Table 2.5), and same as for neutrinos,
350 the WI eigenstates are not the same as the mass eigenstates which means that
351 members of different quark generations are connected by the WI mediator; thus, up-
352 type quarks are coupled not to down-type quarks (the mass eigenstates) directly but
353 to a superposition of down-type quarks (q'_d ; *the weak eigenstates*) via WI according
354 to:

$$355 \quad q'_d = V_{CKM} q_d$$

$$\begin{pmatrix} d' \\ s' \\ b' \end{pmatrix} = \begin{pmatrix} V_{ud} & V_{us} & V_{ub} \\ V_{cd} & V_{cs} & V_{cb} \\ V_{td} & V_{ts} & V_{tb} \end{pmatrix} \begin{pmatrix} d \\ s \\ b \end{pmatrix} \quad (2.3)$$

356 where V_{CKM} is known as Cabibbo-Kobayashi-Maskawa (CKM) mixing matrix [17,18]
357 given by

$$\begin{pmatrix} |V_{ud}| & |V_{us}| & |V_{ub}| \\ |V_{cd}| & |V_{cs}| & |V_{cb}| \\ |V_{td}| & |V_{ts}| & |V_{tb}| \end{pmatrix} = \begin{pmatrix} 0.97427 \pm 0.00015 & 0.22534 \pm 0.00065 & 0.00351^{+0.00015}_{-0.00014} \\ 0.22520 \pm 0.00065 & 0.97344 \pm 0.00016 & 0.0412^{+0.0011}_{-0.0005} \\ 0.00867^{+0.00029}_{-0.00031} & 0.0404^{+0.0011}_{-0.0005} & 0.999146^{+0.000021}_{-0.000046} \end{pmatrix}. \quad (2.4)$$

358 The weak decays of quarks are represented in the diagram of Figure 2.2; again
359 the CKM matrix plays a central role since it contains the probabilities for the differ-

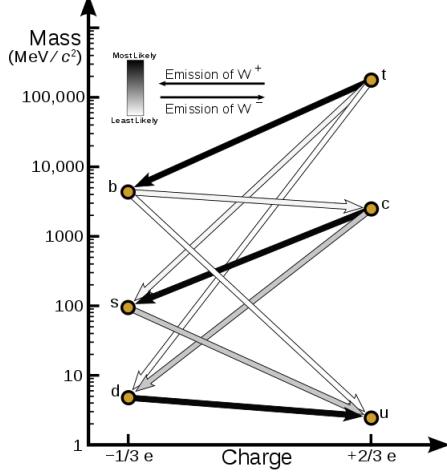


Figure 2.2: Transformations between quarks through the exchange of a WI. Higher generations quarks decay to first generation quarks by emitting a W boson. The arrow color indicates the likelihood of the transition according to the grey scale in the top left side which represent the CKM matrix parameters [19].

360 ent quark decay channels, in particular, note that quark decays are greatly favored
361 between generation members.

362 CKM matrix is a 3×3 unitary matrix parametrized by three mixing angles and
363 the *CP-mixing phase*; the latter is the parameter responsible for the Charge-Parity
364 symmetry violation (CP-violation) in the SM. The fact that the top quark decays
365 almost all the time to a bottom quark is exploited in this thesis when making the
366 selection of the signal events by requiring the presence of a jet tagged as a jet coming
367 from a *b* quark in the final state.

368 2.2.2 Fundamental interactions

369 Even though there are many manifestations of force in nature, like the ones repre-
370 sented in Figure 2.3, we can classify all of them in four fundamental interactions:

- 371 • *Electromagnetic interaction (EI)* affects particles that are *electrically charged*,
372 like electrons and protons. Figure 2.4a. shows a graphical representation, known

Fundamental interactions.

Illustration: Typoform

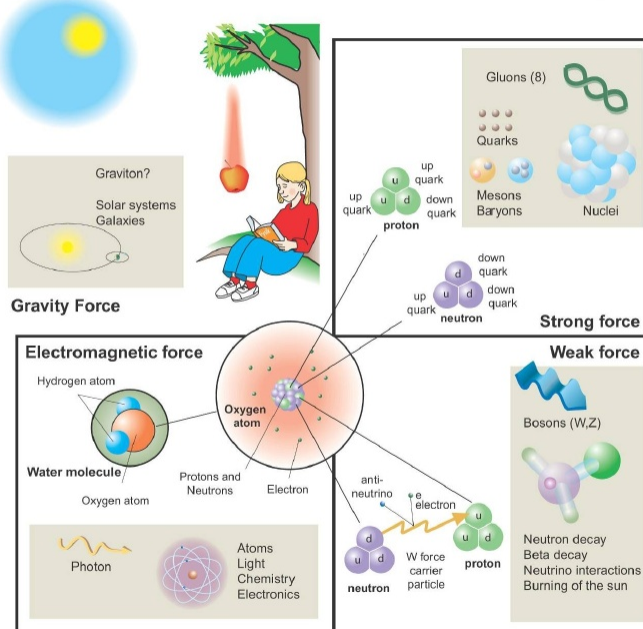


Figure 2.3: Fundamental interactions in nature. Despite the many manifestations of forces in nature, we can track all of them back to one of the fundamental interactions. The most common forces are gravity and electromagnetic given that all of us are subject and experience them in everyday life.

373 as *Feynman diagram*, of electron-electron scattering.

- 374 • *Strong interaction (SI)* described by Quantum Chromodynamics (QCD). Hadrons
 375 like the proton and the neutron have internal structure given that they are com-
 376 posed of two or more valence quarks⁴. Quarks have fractional electric charge
 377 which means that they are subject to electromagnetic interaction and in the case
 378 of the proton they should break apart due to electrostatic repulsion; however,
 379 quarks are held together inside the hadrons against their electrostatic repulsion
 380 by the *Strong Force* through the exchange of *gluons*. The analog to the electric
 381 charge is the *color charge*. Electrons and photons are elementary particles as

⁴ Particles made of four and five quarks are exotic states not so common.

382 quarks but they don't carry color charge, therefore they are not subject to SI. A
 383 Feynman diagram for gluon exchange between quarks is shown in Figure 2.4b.

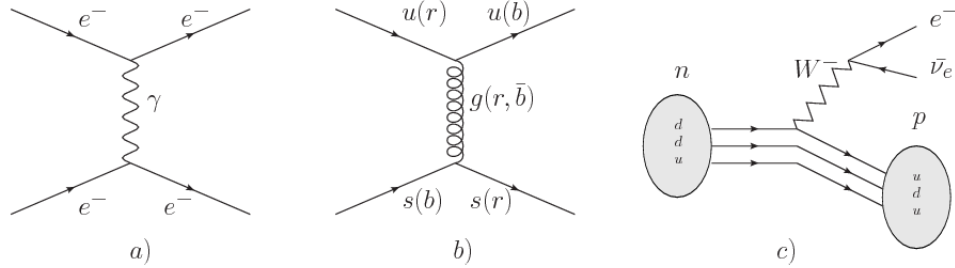


Figure 2.4: Feynman diagrams representing the interactions in SM; a) EI: e - e scattering; b) SI: gluon exchange between quarks ; c) WI: β -decay

384 • *Weak interaction (WI)* described by the weak theory (WT), is responsible, for
 385 instance, for the radioactive decay in atoms and the deuterium production
 386 within the sun. Quarks and leptons are the particles affected by the weak
 387 interaction; they possess a property called *flavor charge* (see 2.2.1) which can
 388 be changed by emitting or absorbing one weak force mediator. There are three
 389 mediators of the *weak force* known as Z boson in the case of electrically neutral
 390 flavor changes and W^\pm bosons in the case of electrically charged flavor changes.
 391 The *weak isospin* is the WI analog to electric charge in EI, and color charge in
 392 SI, and defines how quarks and leptons are affected by the weak force. Figure
 393 2.4c. shows the Feynman diagram of β -decay where a neutron (n) is transformed
 394 in a proton (p) by emitting a W^- particle.

395 • *Gravitational interaction (GI)* described by General Theory of Relativity (GR).
 396 It is responsible for the structure of galaxies and black holes as well as the
 397 expansion of the universe. As a classical theory, in the sense that it can be
 398 formulated without even appeal to the concept of quantization, it implies that
 399 the space-time is a continuum and predictions can be made without limitation

400 to the precision of the measurement tools. The latter represents a direct con-
 401 tradiction of the quantum mechanics principles. Gravity is deterministic while
 402 quantum mechanics is probabilistic; despite that, efforts to develop a quantum
 403 theory of gravity have predicted the *graviton* as mediator of the gravitational
 404 force⁵.

Interaction	Acts on	Relative strength	Range (m)	Mediators
Electromagnetic (QED)	Electrically charged particles	10^{-2}	Infinite	Photon
Strong (QCD)	Quarks and gluons	1	10^{-15}	Gluon
Weak (WI)	Leptons and quarks	10^{-6}	10^{-18}	W^\pm, Z
Gravitational (GI)	Massive particles	10^{-39}	Infinite	Graviton

Table 2.6: Fundamental interactions features [20].

405

406 Table 2.6 summarizes the main features of the fundamental interactions. The
 407 relative strength of the fundamental forces reveals the meaning of strong and weak;
 408 in a context where the relative strength of the SI is 1, the EI is about hundred times
 409 weaker and WI is about million times weaker than the SI. A good description on how
 410 the relative strength and range of the fundamental interactions are calculated can
 411 be found in References [20, 21]. In the everyday life, only EI and GI are explicitly
 412 experienced due to the range of these interactions; i.e., at the human scale distances
 413 only EI and GI have appreciable effects, in contrast to SI which at distances greater
 414 than 10^{-15} m become negligible.

415 2.2.3 Gauge invariance.

416 QED was built successfully on the basis of the classical electrodynamics theory (CED)
 417 of Maxwell and Lorentz, following theoretical and experimental requirements imposed

⁵ Actually a wide variety of theories have been developed in an attempt to describe gravity; some famous examples are string theory and supergravity.

418 by

- 419 • Lorentz invariance: independence on the reference frame.
- 420 • Locality: interacting fields are evaluated at the same space-time point to avoid
421 action at a distance.
- 422 • Renormalizability: physical predictions are finite and well defined.
- 423 • Particle spectrum, symmetries and conservation laws already known must emerge
424 from the theory.
- 425 • Local gauge invariance.

426 The gauge invariance requirement reflects the fact that the fundamental fields
427 cannot be directly measured but associated fields which are the observables. Electric
428 (**E**) and magnetic (**B**) fields in CED are associated with the electric scalar potential
429 V and the vector potential **A**. In particular, **E** can be obtained by measuring the
430 change in the space of the scalar potential (ΔV); however, two scalar potentials
431 differing by a constant f correspond to the same electric field. The same happens
432 in the case of the vector potential **A**; thus, different configurations of the associated
433 fields result in the same set of values of the observables. The freedom in choosing one
434 particular configuration is known as *gauge freedom*; the transformation law connecting
435 two configurations is known as *gauge transformation* and the fact that the observables
436 are not affected by a gauge transformation is called *gauge invariance*.

437 When the gauge transformation:

$$\begin{aligned} \mathbf{A} &\rightarrow \mathbf{A} - \Delta f \\ V &\rightarrow V - \frac{\partial f}{\partial t} \end{aligned} \tag{2.5}$$

438 is applied to Maxwell equations, they are still satisfied and the fields remain invariant.
 439 Thus, CED is invariant under gauge transformations and is called a *gauge theory*.
 440 The set of all gauge transformations form the *symmetry group* of the theory, which
 441 according to the group theory, has a set of *group generators*. The number of group
 442 generators determine the number of *gauge fields* of the theory.

443 As mentioned in the first lines of Section 2.2, QED has one symmetry group ($U(1)$)
 444 with one group generator (the Q operator) and one gauge field (the electromagnetic
 445 field A^μ). In CED there is not a clear definition, beyond the historical convention,
 446 of which fields are the fundamental and which are the associated, but in QED the
 447 fundamental field is A^μ . When a gauge theory is quantized, the gauge fields are
 448 quantized and their quanta are called *gauge bosons*. The word boson characterizes
 449 particles with integer spin which obey Bose-Einstein statistics.

450 As will be detailed in Section 2.3, interactions between particles in a system can
 451 be obtained by considering first the Lagrangian density of free particles in the sys-
 452 tem, which of course is incomplete because the interaction terms have been left out,
 453 and demanding global phase transformation invariance. Global phase transforma-
 454 tion means that a gauge transformation is performed identically to every point
 455 in the space⁶ and the Lagrangian remains invariant. Then, the global transforma-
 456 tion is promoted to a local phase transformation (this time the gauge transforma-
 457 tion depends on the position in space) and again invariance is required.

⁶ Here space corresponds to the 4-dimensional space i.e. space-time.

458 Due to the space dependence of the local transformation, the Lagrangian density is
 459 not invariant anymore. In order to reinstate the gauge invariance, the gauge covariant
 460 derivative is introduced in the Lagrangian and with it the gauge field responsible for
 461 the interaction between particles in the system. The new Lagrangian density is gauge
 462 invariant, includes the interaction terms needed to account for the interactions and
 463 provides a way to explain the interaction between particles through the exchange of
 464 the gauge boson.

465 This recipe was used to build QED and the theories that aim to explain the
 466 fundamental interactions.

467 2.2.4 Gauge bosons

468 The importance of the gauge bosons comes from the fact that they are the force
 469 mediators or force carriers. The features of the gauge bosons reflect those of the fields
 470 they represent and they are extracted from the Lagrangian density used to describe
 471 the interactions. In Section 2.3, it will be shown how the gauge bosons of the EI and
 472 WI emerge from the electroweak Lagrangian. The SI gauge bosons features are also
 473 extracted from the SI Lagrangian but it is not detailed in this document. The main
 474 features of the SM gauge bosons will be briefly presented below and summarized in
 475 Table 2.7.

- 476 • **Photon.** EI occurs when the photon couples to (is exchanged between) parti-
 477 cles carrying electric charge; however, The photon itself does not carry electric
 478 charge, therefore, there is no coupling between photons. Given that the photon
 479 is massless the EI is of infinite range, i.e., electrically charged particles interact
 480 even if they are located far away one from each other; this also implies that
 481 photons always move with the speed of light.

- 482 • **Gluon.** SI is mediated by gluons which just as photons are massless. They
 483 carry one unit of color charge and one unit of anticolor charge, hence, gluons
 484 can couple to other gluons. As a result, the range of the SI is not infinite
 485 but very short due to the attraction between gluons, giving rise to the *color*
 486 *confinement* which explains why color charged particles cannot be isolated but
 487 live within composite particles, like quarks inside protons.
- 488 • **W, Z.** W^\pm and Z, are massive which explains their short-range. Given that
 489 the WI is the only interaction that can change the flavor of the interacting
 490 particles, the W boson is the responsible for the nuclear transmutation where
 491 a neutron is converted into a proton or vice versa with the involvement of an
 492 electron and a neutrino (see Figure 2.4c). The Z boson is the responsible for the
 493 neutral weak processes like neutrino elastic scattering where no electric charge
 494 but momentum transference is involved. WI gauge bosons carry isospin charge
 495 which makes interaction between them possible.

Interaction	Mediator	Electric charge (e)	Color charge	Weak Isospin	mass (GeV/c ²)
Electromagnetic	Photon (γ)	0	No	0	0
Strong	Gluon (g)	0	Yes -octet	No	0
Weak	W^\pm	± 1	No	± 1	80.385 ± 0.015
	Z	0	No	0	91.188 ± 0.002

Table 2.7: SM gauge bosons main features [9].

496

497 **2.3 Electroweak unification and the Higgs 498 mechanism**

499 Physicists dream of building a theory that contains all the interactions in one single
 500 interaction, i.e., showing that at some scale in energy all the four fundamental inter-

actions are unified and only one interaction emerges in a *Theory of everything*. The first sign of the feasibility of such unification came from success in the construction of the CED. Einstein spent years trying to reach that full unification, which by 1920 only involved electromagnetism and gravity, with no success; however, a new partial unification was achieved in the 1960's, when S.Glashow [22], A.Salam [23] and S.Weinberg [24] independently proposed that electromagnetic and weak interactions are two manifestations of a more general interaction called *electroweak interaction* (EWI). EWI was developed by following the useful prescription provided by QED and the gauge invariance principles.

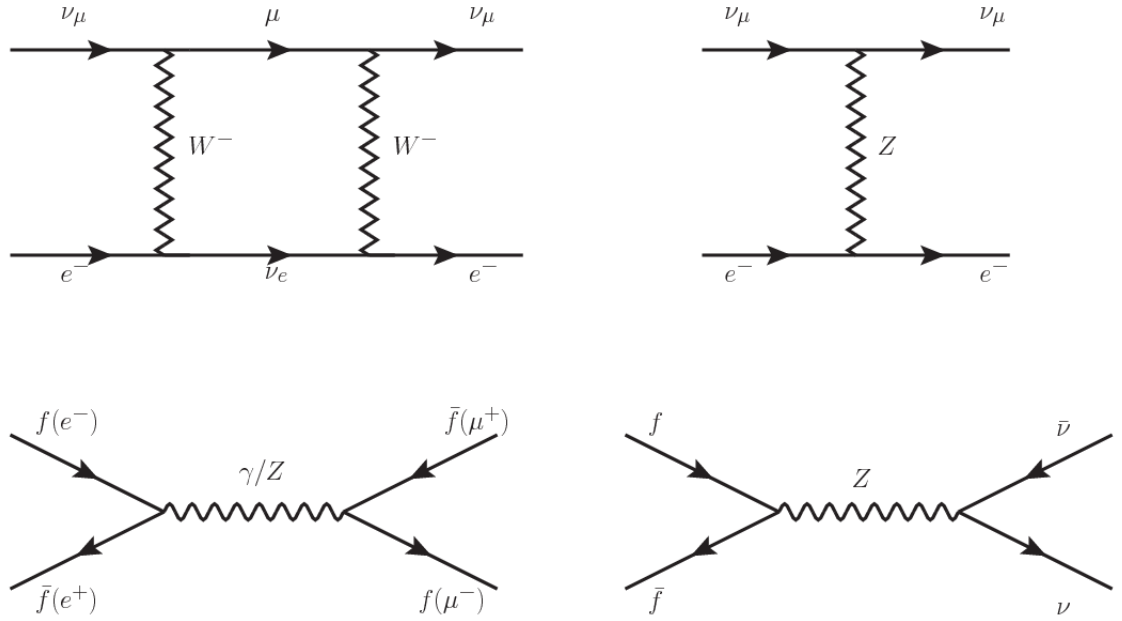


Figure 2.5: Top: $\nu_\mu - e^-$ scattering going through charged currents (left) and neutral currents (right). Bottom: neutral current processes for charged fermions (left) and involving neutrinos (right). While neutral current processes involving only charged fermions can proceed through EI or WI, those involving neutrinos can only proceed via WI.

The *classic* weak theory developed by Fermi, did not have the concept of the W boson but instead it was treated as a point interaction with the dimensionful constant G_F associated with it. It works really well at low energies very far off the W mass

513 shell. When going up in energy, the theory of weak interactions involving the W
 514 boson is capable of explaining the β -decay and in general the processes mediated by
 515 W^\pm bosons. However, there were some processes like the $\nu_\mu - e$ scattering which
 516 would require the exchange of two W bosons (see Figure 2.5 top diagrams) giving
 517 rise to divergent loop integrals and then non-finite predictions. The EWI theory, by
 518 including neutral currents involving fermions via the exchange of a neutral bosons Z,
 519 overcomes those divergences and the predictions become realistic.

520 Neutral weak interaction vertices conserve flavor in the same way as the electro-
 521 magnetic vertices do, but additionally, the Z boson can couple to neutrinos which
 522 implies that processes involving charged fermions can proceed through EI or WI but
 523 processes involving neutrinos can proceed only through WI.

524 The prescription to build a gauge theory of the WI consists of proposing a free
 525 field Lagrangian density that includes the particles involved; next, by requesting
 526 invariance under global phase transformations first and generalizing to local phase
 527 transformations invariance later, the conserved currents are identified and interactions
 528 are generated by introducing gauge fields. Given that the goal is to include the EI
 529 and WI in a single theory, the group symmetry considered should be a combination of
 530 $SU(2)_L$ and $U(1)_{em}$, however the latter cannot be used directly because the EI treats
 531 left and right-handed particles indistinctly in contrast to the former. Fortunately, the
 532 weak hypercharge, which is a combination of the weak isospin and the electric charge
 533 (Eqn. 2.2) is suitable to be used since it is conserved by the EI and WI. Thus, the
 534 symmetry group to be considered is

$$G \equiv SU(2)_L \otimes U(1)_Y \quad (2.6)$$

535 The following treatment applies to any of the fermion generations, but for sim-

536 plicity the first generation of leptons will be considered [5, 6, 25, 26].

537 Given the first generation of leptons

$$\psi_1 = \begin{pmatrix} \nu_e \\ e^- \end{pmatrix}_L, \quad \psi_2 = \nu_{eR}, \quad \psi_3 = e_R^- \quad (2.7)$$

538 the charged fermionic currents are given by

$$J_\mu \equiv J_\mu^+ = \bar{\nu}_{eL} \gamma_\mu e_L, \quad J_\mu^\dagger \equiv J_\mu^- = \bar{e}_L \gamma_\mu \nu_{eL} \quad (2.8)$$

539 and the free Lagrangian is given by

$$\mathcal{L}_0 = \sum_{j=1}^3 i\bar{\psi}_j(x) \gamma^\mu \partial_\mu \psi_j(x). \quad (2.9)$$

540 Mass terms are included directly in the QED free Lagrangians since they preserve
 541 the invariance under the symmetry transformations involved which treat left and right
 542 handed particles similarly, however mass terms of the form

$$m_W^2 W_\mu^\dagger(x) W^\mu(x) + \frac{1}{2} m_Z^2 Z_\mu(x) Z^\mu(x) - m_e \bar{\psi}_e(x) \psi_e(x) \quad (2.10)$$

543 which represent the mass of W^\pm , Z and electrons, are not invariant under G trans-
 544 formations, therefore the gauge fields described by the EWI are in principle massless.

545 Experiments have shown that the EWI gauge fields are not massless [27–30];
 546 however, they have to acquire mass through a mechanism compatible with the gauge
 547 invariance; that mechanism is known as the *Higgs mechanism* and will be considered
 548 later in this Section. The global transformations in the combined symmetry group G
 549 can be written as

$$\begin{aligned}
\psi_1(x) &\xrightarrow{G} \psi'_1(x) \equiv U_Y U_L \psi_1(x), \\
\psi_2(x) &\xrightarrow{G} \psi'_2(x) \equiv U_Y \psi_2(x), \\
\psi_3(x) &\xrightarrow{G} \psi'_3(x) \equiv U_Y \psi_3(x)
\end{aligned} \tag{2.11}$$

550 where U_L represent the $SU(2)_L$ transformation acting only on the weak isospin dou-
 551 blet and U_Y represent the $U(1)_Y$ transformation acting on all the weak isospin mul-
 552 tiplets. Explicitly

$$U_L \equiv \exp\left(i \frac{\sigma_i}{2} \alpha^i\right), \quad U_Y \equiv \exp(i y_i \beta) \quad (i = 1, 2, 3) \tag{2.12}$$

553 with σ_i the Pauli matrices and y_i the weak hypercharges. In order to promote the
 554 transformations from global to local while keeping the invariance, it is required that
 555 $\alpha^i = \alpha^i(x)$, $\beta = \beta(x)$ and the replacement of the ordinary derivatives by the covariant
 556 derivatives

$$\begin{aligned}
D_\mu \psi_1(x) &\equiv \left[\partial_\mu + ig\sigma_i W_\mu^i(x)/2 + ig'y_1 B_\mu(x) \right] \psi_1(x) \\
D_\mu \psi_2(x) &\equiv \left[\partial_\mu + ig'y_2 B_\mu(x) \right] \psi_2(x) \\
D_\mu \psi_3(x) &\equiv \left[\partial_\mu + ig'y_3 B_\mu(x) \right] \psi_3(x)
\end{aligned} \tag{2.13}$$

557 introducing in this way four gauge fields, $W_\mu^i(x)$ and $B_\mu(x)$, in the process. The
 558 covariant derivatives (Eqn. 2.13) are required to transform in the same way as fermion
 559 fields $\psi_i(x)$ themselves, therefore, the gauge fields transform as:

$$\begin{aligned} B_\mu(x) &\xrightarrow{G} B'_\mu(x) \equiv B_\mu(x) - \frac{1}{g'} \partial_\mu \beta(x) \\ W_\mu^i(x) &\xrightarrow{G} W_\mu^{i\prime}(x) \equiv W_\mu^i(x) - \frac{i}{g} \partial_\mu \alpha_i(x) - \varepsilon_{ijk} \alpha_i(x) W_\mu^j(x). \end{aligned} \quad (2.14)$$

560 The G invariant version of the Lagrangian density 2.9 can be written as

$$\mathcal{L}_0 = \sum_{j=1}^3 i \bar{\psi}_j(x) \gamma^\mu D_\mu \psi_j(x) \quad (2.15)$$

561 where free massless fermion and gauge fields and fermion-gauge boson interactions
 562 are included. The EWI Lagrangian density must additionally include kinetic terms
 563 for the gauge fields (\mathcal{L}_G) which are built from the field strengths, according to

$$B_{\mu\nu}(x) \equiv \partial_\mu B_\nu - \partial_\nu B_\mu \quad (2.16)$$

$$W_{\mu\nu}^i(x) \equiv \partial_\mu W_\nu^i(x) - \partial_\nu W_\mu^i(x) - g \varepsilon^{ijk} W_\mu^j W_\nu^k \quad (2.17)$$

564 the last term in Eqn. 2.17 is added in order to hold the gauge invariance; therefore,

$$\mathcal{L}_G = -\frac{1}{4} B_{\mu\nu}(x) B^{\mu\nu}(x) - \frac{1}{4} W_{\mu\nu}^i(x) W_i^{\mu\nu}(x) \quad (2.18)$$

565 which contains not only the free gauge fields contributions, but also the gauge fields
 566 self-interactions and interactions among them.

567 The three weak isospin conserved currents resulting from the $SU(2)_L$ symmetry
 568 are given by

$$J_\mu^i(x) = \frac{1}{2} \bar{\psi}_1(x) \gamma_\mu \sigma^i \psi_1(x) \quad (2.19)$$

569 while the weak hypercharge conserved current resulting from the $U(1)_Y$ symmetry is
 570 given by

$$J_\mu^Y = \sum_{j=1}^3 \bar{\psi}_j(x) \gamma_\mu y_j \psi_j(x) \quad (2.20)$$

571 In order to evaluate the electroweak interactions modeled by an isos triplet field
 572 W_μ^i that couples to isospin currents J_μ^i with strength g and additionally the singlet
 573 field B_μ which couples to the weak hypercharge current J_μ^Y with strength $g'/2$. The
 574 interaction Lagrangian density to be considered is

$$\mathcal{L}_I = -g J^{i\mu}(x) W_\mu^i(x) - \frac{g'}{2} J^{Y\mu}(x) B_\mu(x) \quad (2.21)$$

575 Note that the weak isospin currents are not the same as the charged fermionic cur-
 576 rents that were used to describe the WI (Eqn. 2.8), since the weak isospin eigenstates
 577 are not the same as the mass eigenstates, but they are closely related

$$J_\mu = \frac{1}{2}(J_\mu^1 + iJ_\mu^2), \quad J_\mu^\dagger = \frac{1}{2}(J_\mu^1 - iJ_\mu^2). \quad (2.22)$$

578 The same happens with the gauge fields W_μ^i which are related to the mass eigen-
 579 states W^\pm by

$$W_\mu^+ = \frac{1}{\sqrt{2}}(W_\mu^1 - iW_\mu^2), \quad W_\mu^- = \frac{1}{\sqrt{2}}(W_\mu^1 + iW_\mu^2). \quad (2.23)$$

580 The fact that there are three weak isospin conserved currents is an indication that
 581 in addition to the charged fermionic currents, which couple charged to neutral leptons,
 582 there should be a neutral fermionic current that does not involve electric charge
 583 exchange; therefore, it couples neutral fermions or fermions of the same electric charge.
 584 The third weak isospin current contains a term that is similar to the electromagnetic

585 current (j_μ^{em}), indicating that there is a relation between them and resembling the
 586 Gell-Mann-Nishijima formula 2.2 adapted to electroweak interactions

$$Q = T_3 + \frac{Y_W}{2}. \quad (2.24)$$

587 Just as Q generates the $U(1)_{em}$ symmetry, the weak hypercharge generates the
 588 $U(1)_Y$ symmetry as said before. It is possible to write the relationship in terms of
 589 the currents as

$$j_\mu^{em} = J_\mu^3 + \frac{1}{2} J_\mu^Y. \quad (2.25)$$

590 The neutral gauge fields W_μ^3 and B_μ cannot be directly identified with the Z
 591 and the photon fields since the photon interacts similarly with left and right-handed
 592 fermions; however, they are related through a linear combination given by

$$\begin{aligned} A_\mu &= B_\mu \cos \theta_W + W_\mu^3 \sin \theta_W \\ Z_\mu &= -B_\mu \sin \theta_W + W_\mu^3 \cos \theta_W \end{aligned} \quad (2.26)$$

where θ_W is known as the *Weinberg angle*. The interaction Lagrangian is now given by

$$\begin{aligned} \mathcal{L}_I = -\frac{g}{\sqrt{2}}(J^\mu W_\mu^+ + J^{\mu\dagger} W_\mu^-) - &\left(g \sin \theta_W J_\mu^3 + g' \cos \theta_W \frac{J_\mu^Y}{2}\right) A^\mu \\ &- \left(g \cos \theta_W J_\mu^3 - g' \sin \theta_W \frac{J_\mu^Y}{2}\right) Z^\mu \end{aligned} \quad (2.27)$$

593 the first term is the weak charged current interaction, while the second term is the

594 electromagnetic interaction under the condition

$$g \sin \theta_W = g' \cos \theta_W = e, \quad \frac{g'}{g} = \tan \theta_W \quad (2.28)$$

595 contained in the Eqn.2.25; the third term is the neutral weak current.

596

597 Note that the neutral fields transformation given by the Eqn. 2.26 can be written
 598 in terms of the coupling constants g and g' as:

$$A_\mu = \frac{g' W_\mu^3 + g B_\mu}{\sqrt{g^2 + g'^2}}, \quad Z_\mu = \frac{g W_\mu^3 - g' B_\mu}{\sqrt{g^2 + g'^2}}. \quad (2.29)$$

599 So far, the Lagrangian density describing the non-massive EWI is:

$$\mathcal{L}_{nmEWI} = \mathcal{L}_0 + \mathcal{L}_G \quad (2.30)$$

600 where fermion and gauge fields have been considered massless because their regular
 601 mass terms are manifestly non invariant under G transformations; therefore, masses
 602 have to be generated in a gauge invariant way. The mechanism by which this goal is
 603 achieved is known as the *Higgs mechanism* and is closely connected to the concept of
 604 *spontaneous symmetry breaking*.

605 2.3.1 Spontaneous symmetry breaking (SSB)

606 Figure 2.6 left shows a steel nail (top) which is subject to an external force; the form
 607 of the potential energy is also shown (bottom).

608 Before reaching the critical force value, the system has rotational symmetry with
 609 respect to the nail axis; however, after the critical force value is reached the nail buck-

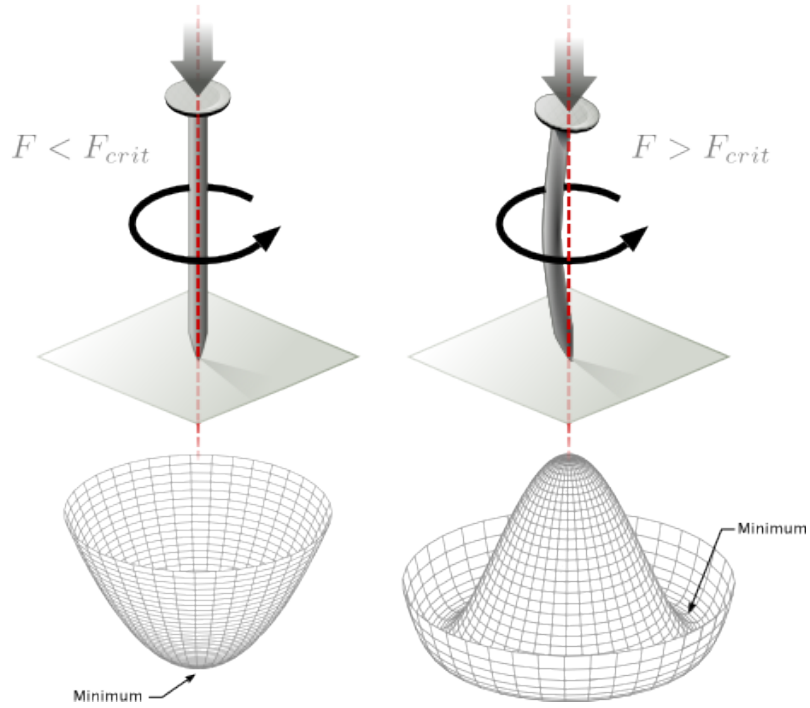


Figure 2.6: Spontaneous symmetry breaking mechanism. The steel nail, subject to an external force (top left), has rotational symmetry with respect to its axis. When the external force overcomes a critical value the nail buckles (top right) choosing a minimal energy state (ground state) and thus *breaking spontaneously the rotational symmetry*. The potential energy (bottom) changes but holds the rotational symmetry; however, an infinite number of asymmetric ground states are generated and circularly distributed in the bottom of the potential [31].

610 les (top right). The form of the potential energy (bottom right) changes appearing a
 611 set of infinity minima but preserving its rotational symmetry. Right before the nail
 612 buckles there is no indication of the direction the nail will bend because any of the
 613 directions are equivalent, but once the nail bends, choosing a direction, an arbitrary
 614 minimal energy state (ground state) is selected and it does not share the system's
 615 rotational symmetry. This mechanism for reaching an asymmetric ground state is
 616 known as *spontaneous symmetry breaking*.

617 The lesson from this analysis is that the way to introduce the SSB mechanism
 618 into a system is by adding the appropriate potential to it.

619 Figure 2.7 shows a plot of the potential $V(\phi)$ in the case of a scalar field ϕ

$$V(\phi) = \mu^2 \phi^\dagger \phi + \lambda (\phi^\dagger \phi)^2 \quad (2.31)$$

620 If $\mu^2 > 0$ the potential has only one minimum at $\phi = 0$ and describes a scalar field
 621 with mass μ . If $\mu^2 < 0$ the potential has a local maximum at $\phi = 0$ and two minima
 622 at $\phi = \pm\sqrt{-\mu^2/\lambda}$ which enables the SSB mechanism to work.

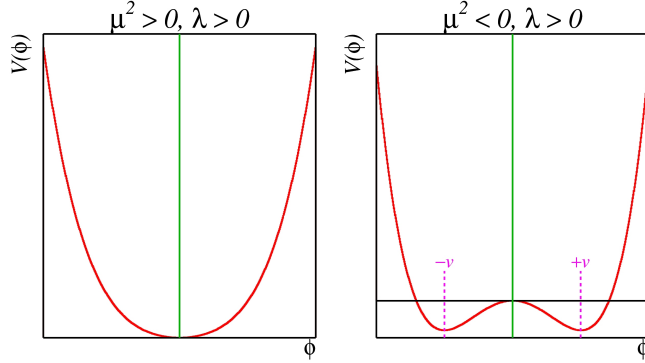


Figure 2.7: Shape of the potential $V(\phi)$ for $\lambda > 0$ and: $\mu^2 > 0$ (left) and $\mu^2 < 0$ (right). The case $\mu^2 < 0$ corresponds to the potential suitable for introducing the SSB mechanism by choosing one of the two ground states which are connected via reflection symmetry. [31].

623 In the case of a complex scalar field $\phi(x)$

$$\phi(x) = \frac{1}{\sqrt{2}}(\phi_1 + i\phi_2) \quad (2.32)$$

624 the Lagrangian (invariant under global $U(1)$ transformations) is given by

$$\mathcal{L} = (\partial_\mu \phi)^\dagger (\partial^\mu \phi) - V(\phi), \quad V(\phi) = \mu^2 \phi^\dagger \phi + \lambda (\phi^\dagger \phi)^2 \quad (2.33)$$

625 where an appropriate potential has been added in order to introduce the SSB.

626 As seen in Figure 2.8, the potential has now an infinite number of minima circularly
 627 distributed along the ξ -direction which makes possible the occurrence of the SSB by
 628 choosing an arbitrary ground state; for instance, $\xi = 0$, i.e. $\phi_1 = v, \phi_2 = 0$

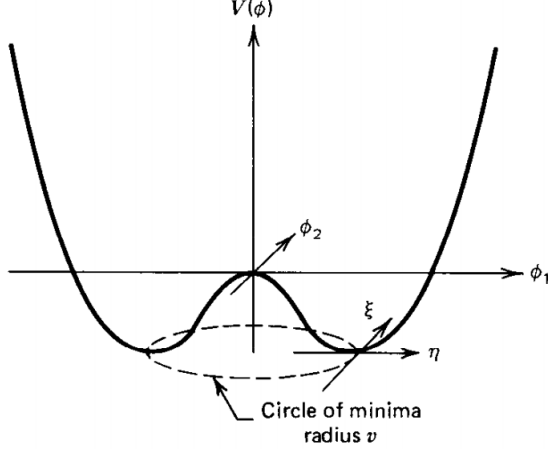


Figure 2.8: Potential for complex scalar field. There is a circle of minima of radius v along the ξ -direction [6].

$$\phi_0 = \frac{v}{\sqrt{2}} \exp(i\xi) \quad \xrightarrow{\text{SSB}} \quad \phi_0 = \frac{v}{\sqrt{2}} \quad (2.34)$$

629 As usual, excitations over the ground state are studied by making an expansion
 630 about it; thus, the excitations can be parametrized as:

$$\phi(x) = \frac{1}{\sqrt{2}}(v + \eta(x) + i\xi(x)) \quad (2.35)$$

631 which when substituted into Eqn. 2.33 produces a Lagrangian in terms of the new
 632 fields η and ξ

$$\mathcal{L}' = \frac{1}{2}(\partial_\mu \xi)^2 + \frac{1}{2}(\partial_\mu \eta)^2 + \mu^2 \eta^2 - V(\phi_0) - \lambda v \eta (\eta^2 + \xi^2) - \frac{\lambda}{4}(\eta^2 + \xi^2)^2 \quad (2.36)$$

633 where the last two terms represent the interactions and self-interaction between the
 634 two fields η and ξ . The particular feature of the SSB mechanism is revealed when
 635 looking to the first three terms of \mathcal{L}' . Before the SSB, only the massless ϕ field is

636 present in the system; after the SSB there are two fields of which the η -field has
 637 acquired mass $m_\eta = \sqrt{-2\mu^2}$ while the ξ -field is still massless (see Figure 2.9).

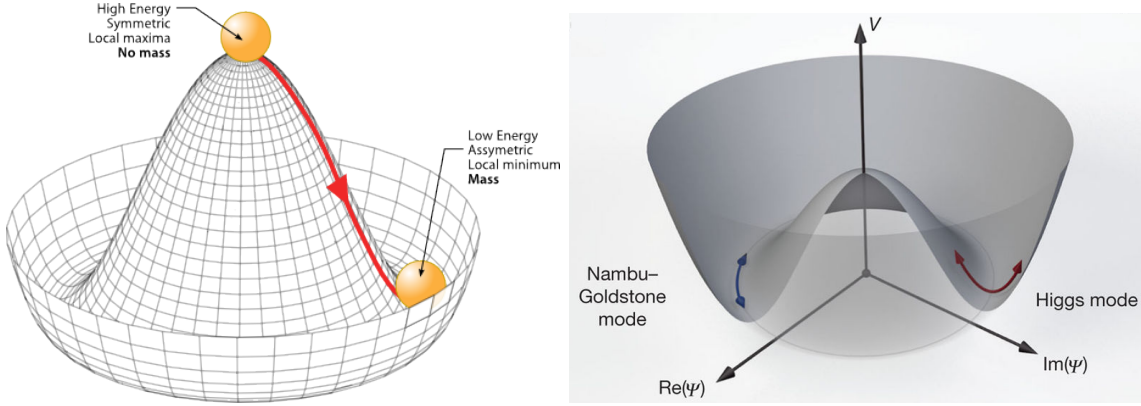


Figure 2.9: SSB mechanism for a complex scalar field [31, 32].

638 Thus, the SSB mechanism serves as a method to generate mass but as a side ef-
 639 fect a massless field is introduced in the system. This fact is known as the Goldstone
 640 theorem and states that a massless scalar field appears in the system for each con-
 641 tinuous symmetry spontaneously broken. Another version of the Goldstone theorem
 642 states that “if a Lagrangian is invariant under a continuous symmetry group G , but
 643 the vacuum is only invariant under a subgroup $H \subset G$, then there must exist as many
 644 massless spin-0 particles (Nambu-Goldstone bosons) as broken generators.” [26] The
 645 Nambu-Goldstone boson can be understood considering that the potential in the ξ -
 646 direction is flat so excitations in that direction are not energy consuming and thus
 647 represent a massless state.

648 2.3.2 Higgs mechanism

649 When the SSB mechanism is introduced in the formulation of the EWI in an attempt
 650 to generate the mass of the so far massless gauge bosons and fermions, an interesting
 651 effect is revealed. In order to keep the G symmetry group invariance and generate

652 the mass of the EW gauge bosons, a G invariant Lagrangian density (\mathcal{L}_S) has to be
 653 added to the non massive EWI Lagrangian (Eqn. 2.30)

$$\mathcal{L}_S = (D_\mu \phi)^\dagger (D^\mu \phi) - \mu^2 \phi^\dagger \phi - \lambda (\phi^\dagger \phi)^2, \quad \lambda > 0, \mu^2 < 0 \quad (2.37)$$

$$D_\mu \phi = \left(i\partial_\mu - g \frac{\sigma_i}{2} W_\mu^i - g' \frac{Y}{2} B_\mu \right) \phi \quad (2.38)$$

654 ϕ has to be an isospin doublet of complex scalar fields so it preserves the G invariance;
 655 thus ϕ can be defined as:

$$\phi = \begin{pmatrix} \phi^+ \\ \phi^0 \end{pmatrix} \equiv \frac{1}{\sqrt{2}} \begin{pmatrix} \phi_1 + i\phi_2 \\ \phi_3 + i\phi_4 \end{pmatrix}. \quad (2.39)$$

656 The minima of the potential are defined by

$$\phi^\dagger \phi = \frac{1}{2} (\phi_1^2 + \phi_2^2 + \phi_3^2 + \phi_4^2) = -\frac{\mu^2}{2\lambda}. \quad (2.40)$$

657 The choice of the ground state is critical. By choosing a ground state, invariant
 658 under $U(1)_{em}$ gauge symmetry, the photon will remain massless and the W^\pm and Z
 659 bosons masses will be generated which is exactly what is needed. In that sense, the
 660 best choice corresponds to a weak isospin doublet with $T_3 = -1/2$, $Y_W = 1$ and $Q = 0$
 661 which defines a ground state with $\phi_1 = \phi_2 = \phi_4$ and $\phi_3 = v$:

$$\phi_0 \equiv \frac{1}{\sqrt{2}} \begin{pmatrix} 0 \\ v \end{pmatrix}, \quad v^2 \equiv -\frac{\mu^2}{\lambda}. \quad (2.41)$$

662 where the vacuum expectation value v is fixed by the Fermi coupling G_F according
 663 to $v = (\sqrt{2}G_F)^{1/2} \approx 246$ GeV.

664 The G symmetry has been broken and three Nambu-Goldstone bosons will appear.

665 The next step is to expand ϕ about the chosen ground state as:

$$\phi(x) = \frac{1}{\sqrt{2}} \exp\left(\frac{i}{v} \sigma_i \theta^i(x)\right) \begin{pmatrix} 0 \\ v + H(x) \end{pmatrix} \approx \frac{1}{\sqrt{2}} \begin{pmatrix} \theta_1(x) + i\theta_2(x) \\ v + H(x) - i\theta_3(x) \end{pmatrix} \quad (2.42)$$

666 to describe fluctuations from the ground state ϕ_0 . The fields $\theta_i(x)$ represent the
 667 Nambu-Goldstone bosons while $H(x)$ is known as *Higgs field*. The fundamental fea-
 668 ture of the parametrization used is that the dependence on the $\theta_i(x)$ fields is factored
 669 out in a global phase that can be eliminated by taking the physical *unitary gauge*
 670 $\theta_i(x) = 0$. Therefore the expansion about the ground state is given by:

$$\phi(x) \frac{1}{\sqrt{2}} \begin{pmatrix} 0 \\ v + H(x) \end{pmatrix} \quad (2.43)$$

671 which when substituted into \mathcal{L}_S (Eqn. 2.37) results in a Lagrangian containing the
 672 now massive three gauge bosons W^\pm, Z , one massless gauge boson (photon) and
 673 the new Higgs field (H). The three degrees of freedom corresponding to the Nambu-
 674 Goldstone bosons are now integrated into the massive gauge bosons as their lon-
 675 gitudinal polarizations which were not available when they were massless particles.
 676 The effect by which vector boson fields acquire mass after an spontaneous symmetry
 677 breaking, but without an explicit gauge invariance breaking is known as the *Higgs*
 678 *mechanism*.

679 The mechanism was proposed by three independent groups: F.Englert and R.Brout
 680 in August 1964 [33], P.Higgs in October 1964 [34] and G.Guralnik, C.Hagen and
 681 T.Kibble in November 1964 [35]; however, its importance was not realized until
 682 S.Glashow [22], A.Salam [23] and S.Weinberg [24], independently, proposed that elec-
 683 tromagnetic and weak interactions are two manifestations of a more general interac-
 684 tion called *electroweak interaction* in 1967.

685 **2.3.3 Masses of the gauge bosons**

686 The masses of the gauge bosons are extracted by evaluating the kinetic part of La-
 687 grangian \mathcal{L}_S in the ground state (known also as the vacuum expectation value), i.e.,

$$\left| \left(\partial_\mu - ig \frac{\sigma_i}{2} W_\mu^i - i \frac{g'}{2} B_\mu \right) \phi_0 \right|^2 = \left(\frac{1}{2} v g \right)^2 W_\mu^+ W^{-\mu} + \frac{1}{8} v^2 (W_\mu^3, B_\mu) \begin{pmatrix} g^2 & -gg' \\ -gg' & g'^2 \end{pmatrix} \begin{pmatrix} W^{3\mu} \\ B^\mu \end{pmatrix} \quad (2.44)$$

688 comparing with the typical mass term for a charged boson $M_W^2 W^+ W^-$

$$M_W = \frac{1}{2} v g. \quad (2.45)$$

The second term in the right side of the Eqn.2.44 comprises the masses of the neutral bosons, but it needs to be written in terms of the gauge fields Z_μ and A_μ in order to be compared to the typical mass terms for neutral bosons, therefore using Eqn. 2.29

$$\begin{aligned} \frac{1}{8} v^2 [g^2 (W_\mu^3)^2 - 2gg' W_\mu^3 B^\mu + g'^2 B_\mu^2] &= \frac{1}{8} v^2 [g W_\mu^3 - g' B_\mu]^2 + 0[g' W_\mu^3 + g B_\mu]^2 \quad (2.46) \\ &= \frac{1}{8} v^2 [\sqrt{g^2 + g'^2} Z_\mu]^2 + 0[\sqrt{g^2 + g'^2} A_\mu]^2 \end{aligned}$$

689 and then

$$M_Z = \frac{1}{2} v \sqrt{g^2 + g'^2}, \quad M_A = 0 \quad (2.47)$$

690 **2.3.4 Masses of the fermions**

691 The lepton mass terms can be generated by introducing a gauge invariant Lagrangian
 692 term describing the Yukawa coupling between the lepton field and the Higgs field

$$\mathcal{L}_{Yl} = -G_l \left[(\bar{\nu}_l, \bar{l})_L \begin{pmatrix} \phi^+ \\ \phi^0 \end{pmatrix} l_R + \bar{l}_R (\phi^-, \bar{\phi}^0) \begin{pmatrix} \nu_l \\ l \end{pmatrix} \right], \quad l = e, \mu, \tau. \quad (2.48)$$

693 After the SSB and replacing the usual field expansion about the ground state
 694 (Eqn.2.41) into \mathcal{L}_{Yl} , the mass term arises

$$\mathcal{L}_{Yl} = -m_l (\bar{l}_L l_R + \bar{l}_R l_L) - \frac{m_l}{v} (\bar{l}_L l_R + \bar{l}_R l_L) H = -m_l \bar{l} \left(1 + \frac{H}{v} \right) \quad (2.49)$$

695

$$m_l = \frac{G_l}{\sqrt{2}} v \quad (2.50)$$

696 where the additional term represents the lepton-Higgs interaction. The quark masses
 697 are generated in a similar way as lepton masses but for the upper member of the
 698 quark doublet a different Higgs doublet is needed:

$$\phi_c = -i\sigma_2 \phi^* = \begin{pmatrix} -\bar{\phi}^0 \\ \phi^- \end{pmatrix}. \quad (2.51)$$

699 Additionally, given that the quark isospin doublets are not constructed in terms
 700 of the mass eigenstates but in terms of the flavor eigenstates, as shown in Table 2.5,
 701 the coupling parameters will be related to the CKM matrix elements; thus the quark
 702 Lagrangian is given by:

$$\mathcal{L}_{Yq} = -G_d^{i,j} (\bar{u}_i, \bar{d}'_i)_L \begin{pmatrix} \phi^+ \\ \phi^0 \end{pmatrix} d_{jR} - G_u^{i,j} (\bar{u}_i, \bar{d}'_i)_L \begin{pmatrix} -\bar{\phi}^0 \\ \phi^- \end{pmatrix} u_{jR} + h.c. \quad (2.52)$$

703 with $i, j = 1, 2, 3$. After SSB and expansion about the ground state, the diagonal form

704 of \mathcal{L}_{Yq} is:

$$\mathcal{L}_{Yq} = -m_d^i \bar{d}_i d_i \left(1 + \frac{H}{v}\right) - m_u^i \bar{u}_i u_i \left(1 + \frac{H}{v}\right) \quad (2.53)$$

705 Fermion masses depend on arbitrary couplings G_l and $G_{u,d}$ and are not predicted
706 by the theory.

707 2.3.5 The Higgs field

708 After the characterization of the fermions and gauge bosons as well as their interac-
709 tions, it is necessary to characterize the Higgs field itself. The Lagrangian \mathcal{L}_S in Eqn.
710 2.37 written in terms of the gauge bosons is given by

$$\mathcal{L}_S = \frac{1}{4} \lambda v^4 + \mathcal{L}_H + \mathcal{L}_{HV} \quad (2.54)$$

711

$$\mathcal{L}_H = \frac{1}{2} \partial_\mu H \partial^\mu H - \frac{1}{2} m_H^2 H^2 - \frac{1}{2v} m_H^2 H^3 - \frac{1}{8v^2} m_H^2 H^4 \quad (2.55)$$

712

$$\mathcal{L}_{HV} = m_H^2 W_\mu^+ W^{\mu-} \left(1 + \frac{2}{v} H + \frac{2}{v^2} H^2\right) + \frac{1}{2} m_Z^2 Z_\mu Z^\mu \left(1 + \frac{2}{v} H + \frac{2}{v^2} H^2\right) \quad (2.56)$$

713 The mass of the Higgs boson is deduced as usual from the mass term in the Lagrangian
714 resulting in:

$$m_H = \sqrt{-2\mu^2} = \sqrt{2\lambda}v \quad (2.57)$$

715 however, it is not predicted by the theory either. The experimental efforts to find the
716 Higgs boson, carried out by the *Compact Muon Solenoid (CMS)* experiment and the *A*
717 *Toroidal LHC Appartus (ATLAS)* experiments at the *Large Hadron Collider (LHC)*,
718 gave great results by July of 2012 when the discovery of a new particle compatible
719 with the Higgs boson predicted by the electroweak theory [36, 37] was announced.
720 Although at the announcement time there were some reservations about calling the
721 new particle the *Higgs boson*, today this name is widely accepted. The Higgs mass

722 measurement, reported by both experiments [38], is in Table 2.8.

Property	Value
Electric charge	0
Color charge	0
Spin	0
Weak isospin	-1/2
Weak hypercharge	1
Parity	1
Mass (GeV/c ²)	125.09±0.21 (stat.)±0.11 (syst.)

Table 2.8: Higgs boson properties. Higgs mass is not predicted by the theory and the value here corresponds to the experimental measurement.

723

724 2.3.6 Production of Higgs bosons at LHC

725 At the LHC, Higgs bosons are produced as a result of the collision of two counter-
726 rotating protons beams. A detailed description of the LHC machine will be presented
in chapter 3.

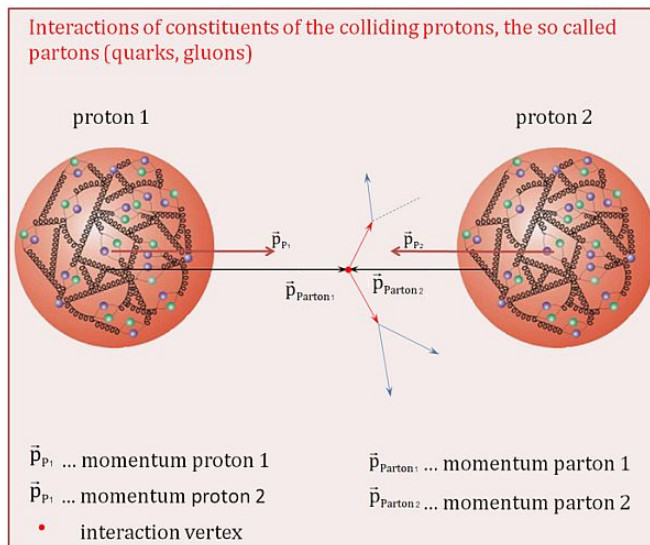


Figure 2.10: Proton-proton collision. Protons are composed of 3 valence quarks, a sea of quarks and gluons; therefore in a proton-proton collision, quarks and gluons are those who collide. [39].

727

728 Protons are composed of quarks and these quarks are bound by gluons; however,
729 what is commonly called the quark content of the proton makes reference to the
730 valence quarks. In fact, a proton is not just a rigid entity with three balls in it all
731 tied up with springs, but the gluons exchanged by the valence quarks tend to split
732 spontaneously into quark-antiquark pairs or more gluons, creating *sea of quarks and*
733 *gluons* as represented in Figure 2.10.

734 In a proton-proton (pp) collision, the proton's constituents, quarks and gluons, are
735 those that collide. The pp cross section depends on the momentum of the colliding
736 particles, reason for which it is needed to know how the momentum is distributed
737 inside the proton. Quarks and gluons are known as partons, hence, the functions that
738 describe how the proton momentum is distributed among partons inside it are called
739 *parton distribution functions (PDFs)*; PDFs are determined from experimental data
740 obtained in experiments where the internal structure of hadrons is tested.

741 In addition, in physics, a common approach to study complex systems consists
742 of starting with a simpler version of them, for which a well known description is
743 available, and adding an additional *perturbation* which represents a small deviation
744 from the known behavior. If the perturbation is small enough, the physical quantities
745 associated with the perturbed system are expressed as a series of corrections to those
746 of the simpler system. The perturbation series corresponds to an expansion in power
747 series of a small parameter, therefore, the more terms are considered in the series (the
748 higher order in the perturbation series), the more precise is the the description of the
749 complex system. If the perturbation does not get progressively smaller, the strategy
750 cannot be applied and new methods have to be employed.

751 High energy systems, like the Higgs production at LHC explored in this thesis,
752 usually can be treated perturbatively with the expansion made in terms of the cou-
753 pling constants. The overview presented here will be oriented specifically to the Higgs

754 boson production mechanisms in pp collisions at LHC.

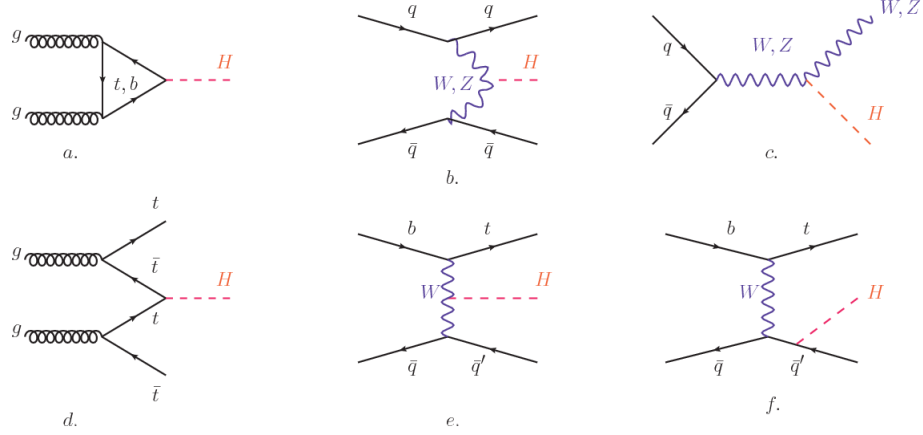


Figure 2.11: Main Higgs boson production mechanism Feynman diagrams. a. gluon-gluon fusion, b. vector boson fusion (VBF), c. Higgs-strahlung, d. Associated production with a top or bottom quark pair, e-f. associated production with a single top quark.

755 Figure 2.11 shows the Feynman diagrams for the leading order (first order) Higgs
 756 production processes at LHC, while the cross section for Higgs production as a func-
 757 tion of the center of mass-energy (\sqrt{s}) for pp collisions is showed in Figure 2.12 left.
 758 The tags NLO (next to leading order), NNLO (next to next to leading order) and
 759 N3LO (next to next to next to leading order) make reference to the order at which
 760 the perturbation series have been considered while the tags QCD and EW correspond
 761 to the strong and electroweak coupling constants respectively.

762 The main production mechanism is the gluon fusion (Figure 2.11a and $pp \rightarrow H$ in
 763 Figure 2.12) given that gluons carry the highest fraction of momentum of the protons
 764 in pp colliders. Since the Higgs boson does not couple to gluons, the mechanism
 765 proceeds through the exchange of a virtual top-quark loop. Note that in this process
 766 the Higgs boson is produced alone, turning out to be problematic for some Higgs
 767 decays, because such absence of anything produced in association with the Higgs
 768 represent a trouble for triggering, however, this mechanism is experimentally clean
 769 when combined with the two-photon or the four-lepton decay channels (see Section

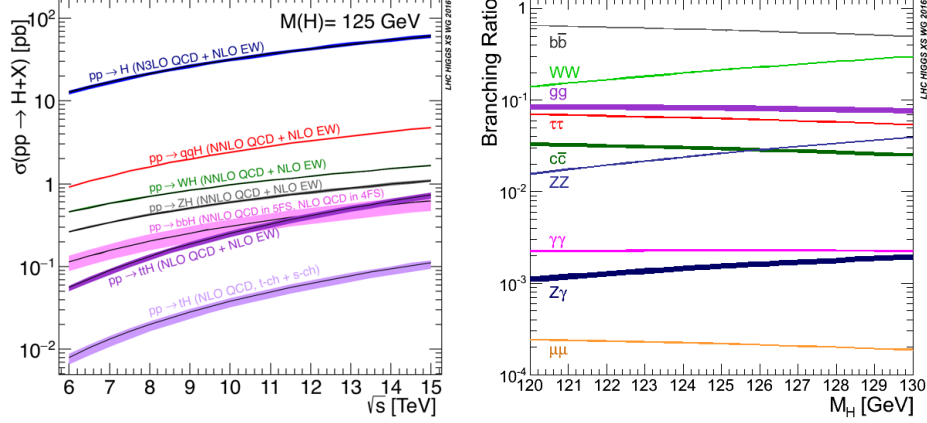


Figure 2.12: Higgs boson production cross sections (left) and decay branching ratios (right) for the main mechanisms. The VBF is indicated as qqH [40].

770 2.3.7).

771 Vector boson fusion (Figure 2.11b and $pp \rightarrow qqH$ in Figure 2.12) has the second
 772 largest production cross section. The scattering of two fermions is mediated by a weak
 773 gauge boson which later emits a Higgs boson. In the final state, the two fermions tend
 774 to be located in the central region of the detector; this kind of features are generally
 775 used as a signature when analyzing the datasets provided by the experiments⁷.

776 The next production mechanism is Higgs-strahlung (Figure 2.11c and $pp \rightarrow WH, pp \rightarrow$
 777 ZH in Figure 2.12) where two fermions annihilate to form a weak gauge boson. If the
 778 initial fermions have enough energy, the emergent boson might emit a Higgs boson.

779 The associated production with a top or bottom quark pair and the associated
 780 production with a single top quark (Figure 2.11d-f and $pp \rightarrow bbH, pp \rightarrow t\bar{t}H, pp \rightarrow tH$
 781 in Figure 2.12) have a smaller cross section than the main three mechanisms above,
 782 but they provide a good opportunity to test the Higgs-top coupling. The analysis
 783 reported in this thesis is developed using these production mechanisms. A detailed
 784 description of the tH mechanism will be given in Section 2.5.

⁷ More details about how to identify events of interest in this analysis will be given in chapter 6.

785 2.3.7 Higgs boson decay channels

786 When a particle can decay through several modes, also known as channels, the prob-
 787 ability of decaying through a given channel is quantified by the *branching ratio (BR)*
 788 of the decay channel; thus, the BR is defined as the ratio of number of decays go-
 789 ing through that given channel to the total number of decays. In regard to the
 790 Higgs boson decay, the BR can be predicted with accuracy once the Higgs mass is
 791 known [41,42]. In Figure 2.12 right, a plot of the BR as a function of the Higgs mass
 792 is presented; the largest predicted BR corresponds to the $b\bar{b}$ pair decay channel (see
 793 Table 2.9) given that it is the heaviest particle pair whose on-shell⁸ production is
 794 kinematically allowed in the decay.

Decay channel	Branching ratio	Rel. uncertainty
$H \rightarrow b\bar{b}$	5.84×10^{-1}	$+3.2\% - 3.3\%$
$H \rightarrow W^+W^-$	2.14×10^{-1}	$+4.3\% - 4.2\%$
$H \rightarrow \tau^+\tau^-$	6.27×10^{-2}	$+5.7\% - 5.7\%$
$H \rightarrow ZZ$	2.62×10^{-2}	$+4.3\% - 4.1\%$
$H \rightarrow \gamma\gamma$	2.27×10^{-3}	$+5.0\% - 4.9\%$
$H \rightarrow Z\gamma$	1.53×10^{-3}	$+9.0\% - 8.9\%$
$H \rightarrow \mu^+\mu^-$	2.18×10^{-4}	$+6.0\% - 5.9\%$

Table 2.9: Predicted branching ratios and the relative uncertainty for some decay channels of a SM Higgs boson with $m_H = 125\text{GeV}/c^2$ [9]; the uncertainties are driven by theoretical uncertainties for the different Higgs boson partial widths and by parametric uncertainties associated to the strong coupling and the masses of the quarks which are the input parameters. Further details on these calculations can be found in Reference [43]

795

796 Decays to other lepton and quark pairs, like electron, strange, up, and down
 797 quark pairs not listed in the table, are also possible but their likelihood is too small

⁸ In general, on-shell or real particles are those which satisfy the energy-momentum relation ($E^2 - |\vec{p}|^2 c^2 = m^2 c^4$); off-shell or virtual particles does not satisfy it which is possible under the uncertainty principle of quantum mechanics. Usually, virtual particles correspond to internal propagators in Feynman diagrams.

798 to measure since they are very lightweight, hence, their interaction with the Higgs
 799 boson is very weak. On other hand, the decay to top quark pairs is heavily suppressed
 800 due to the top quark mass ($\approx 173 \text{ GeV}/c^2$).

801 Decays to gluons proceed indirectly through a virtual top quark loop while the
 802 decays to photons proceed through a virtual W boson loop, therefore, their branching
 803 ratio is smaller compared to direct interaction decays. Same is true for the decay to
 804 a photon and a Z boson.

805 In the case of decays to pairs of W and Z bosons, the decay proceed with one of
 806 the bosons being on-shell and the other being off-shell. The likelihood of the process
 807 diminish depending on how far off-shell are the virtual particles involved, hence, the
 808 branching ratio for W boson pairs is bigger than for Z boson pairs since Z boson mass
 809 is bigger than W boson mass.

810 Note that the decay to a pair of virtual top quarks is possible, but the probability
 811 is way too small.

812 **2.4 Experimental status of the anomalous**

813 **Higgs-fermion coupling**

814 ATLAS and CMS have performed analyses of the anomalous H-f coupling by making
 815 likelihood scans for the two coupling modifiers, κ_t and κ_V , under the assumption
 816 that $\kappa_Z = \kappa_W \equiv \kappa_V$ and $\kappa_t = \kappa_\tau = \kappa_b \equiv \kappa_f$. Figure 2.13 shows the result of the
 817 combination of ATLAS and CMS fits; also the individual decay channels combination
 818 and the global combination results are shown. Note that from this plot there is limited
 819 information on the sign of the coupling since the only information available about the
 820 sign of the coupling comes from decays rather than production.

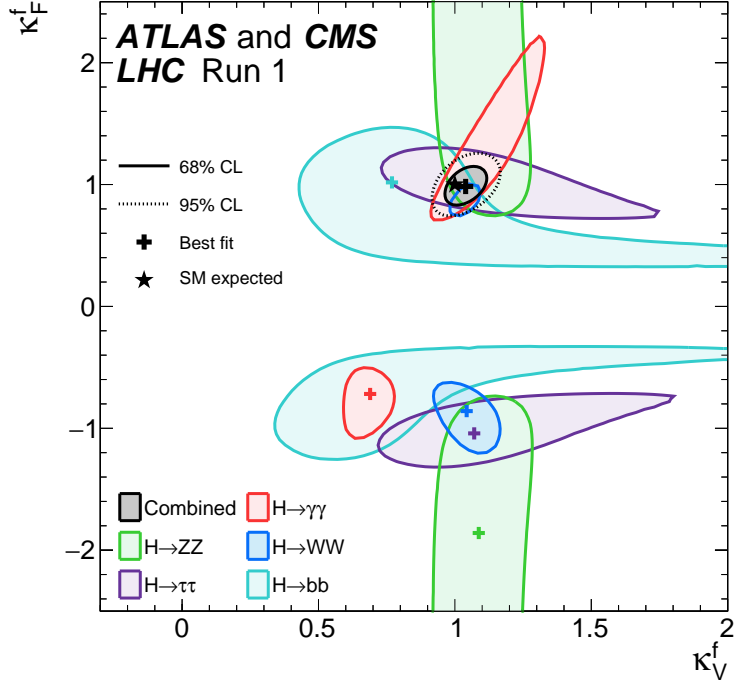


Figure 2.13: Combination of the ATLAS and CMS fits for coupling modifiers $\kappa_t - \kappa_V$; also shown the individual decay channels combination and their global combination. No assumptions have been made on the sign of the coupling modifiers [58].

While all the channels are compatible for positive values of the modifiers, for negative values of κ_t there is no compatibility. The best fit for individual channels is compatible with negative values of κ_t except for the $H \rightarrow bb$ channel. The best fit for the global fit yields $\kappa_t \geq 0$ in contrast to the yields from the individual channels; the reason of this resides in the $H \rightarrow \gamma\gamma$ coupling parameter. $H \rightarrow \gamma\gamma$ decay proceeds through a loop of either top quarks or W bosons, hence, this channel is sensitive to κ_t due to the interference of these two amplitude contributions. Under the assumption that no beyond SM particles take part in the loops, a flipped sign of κ_t will increase the $H \rightarrow \gamma\gamma$ branching fraction by a factor of ~ 2.4 which is not supported by measurements; thus, this large asymmetry between the positive and negative coupling ratios in the $H \rightarrow \gamma\gamma$ channel drives the yield of the global fit. Nevertheless, since the

832 $H \rightarrow bb$ channel is expected to be the most sensitive channel and its best fit value of
 833 κ_t is positive, the global fit is well supported as shown in Reference [58].

834 Although the contributions from all the other decay channels are small compared
 835 to the $H \rightarrow bb$ the anomalous H-t coupling cannot be excluded completely, thus, that
 836 motivates to look at tH processes, which can help with both, the limited information
 837 on the sign of the H-t coupling and the access to information from the Higgs boson
 838 production rather than from its decays.

839 **2.5 Associated production of a Higgs boson and a 840 single top quark**

841 The production of Higgs boson in association with a top quark has been extensively
 842 studied [44–48]. While measurements of the main Higgs production mechanisms rates
 843 are sensitive to the strength of the Higgs coupling to W boson or top quark, they are
 844 not sensitive to the relative sign between the two couplings. In this thesis, the Higgs
 845 boson production mechanism explored is the associated production with a single top
 846 quark (tH) which offers sensitivity to the relative sign of the Higgs couplings to W
 847 boson and to top quark. The description given here is based on Reference [46]

A process where two incoming particles interact and produce a final state with two particles can proceed in three called channels (see, for instance, Figure 2.14 omitting the red line). The t-channel represents processes where an intermediate particle is emitted by one of the incoming particles and absorbed by the other. The s-channel represents processes where the two incoming particles merge into an intermediate particle which eventually will split into the particles in the final state. The third channel, u-channel, is similar to the t-channel but the two outgoing particles interchange their

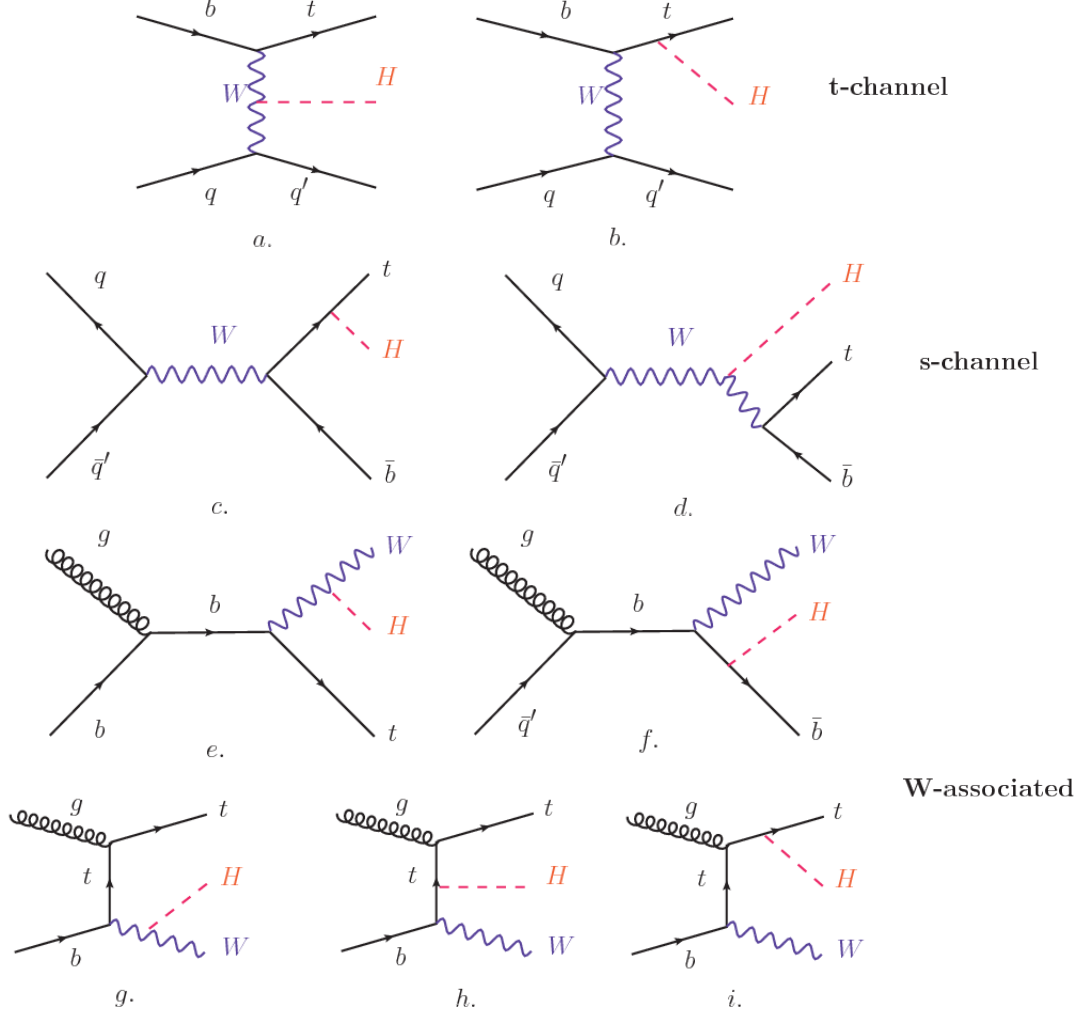


Figure 2.14: Associated Higgs boson production with a top quark mechanism Feynman diagrams. a.,b. t-channel (tHq), c.,d. s-channel (tHb), e-i. W-associated.

roles. These three channels are connected to the so-called Mandelstam variables

$$s = (p_1 + p_2)^2 = (p'_1 + p'_2)^2 \rightarrow \text{square of the center mass-energy.} \quad (2.58)$$

$$t = (p_1 - p'_1)^2 = (p'_2 - p_2)^2 \rightarrow \text{square of the four-momentum transfer.} \quad (2.59)$$

$$u = (p_1 - p'_2)^2 = (p'_1 - p_2)^2 \rightarrow \text{square of the crossed four-momentum transfer.} \quad (2.60)$$

$$s + t + u = m_1^2 + m_2^2 + m'_1^2 + m'_2^2 \quad (2.61)$$

which relate the momentum, energy and the angles of the incoming and outgoing particles in an scattering process of two particles to two particles. The importance of the Mandelstam variables reside in that they form a minimum set of variables needed to describe the kinematics of this scattering process; they are Lorentz invariant which makes them very useful when doing calculations.

The tH production, where Higgs boson can be radiated either from the top quark or from the W boson, is represented by the leading order Feynman diagrams in Figure 2.14. The cross section for the tH process is calculated, as usual, summing over the contributions from the different Feynman diagrams; therefore it depends on the interference between the contributions. In the SM, the interference for t-channel (tHq process) and W-associated (tHW process) production is destructive [44] resulting in the small cross sections presented in Table 2.10.

tH production channel	Cross section (fb)
t-channel ($pp \rightarrow tHq$)	$70.79^{+2.99}_{-4.80}$
W-associated ($pp \rightarrow tHW$)	$15.61^{+0.83}_{-1.04}$
s-channel($pp \rightarrow tHb$)	$2.87^{+0.09}_{-0.08}$

Table 2.10: Predicted SM cross sections for tH production at $\sqrt{s} = 13$ TeV [49, 50].

860

The s-channel contribution can be neglected. It will be shown that a deviation from the SM destructive interference would result in an enhancement of the tH cross section compared to that in SM, which could be used to get information about the sign of the Higgs-top coupling [46, 47]. In order to describe tH production processes, Feynman diagram 2.14b will be considered; there, the W boson is radiated by a quark in the proton and eventually it will interact with the b quark. In the high energy regime, the effective W approximation [51] is used to describe the process as the

868 emission of an approximately on-shell W and its hard scattering with the b quark;
 869 i.e. $Wb \rightarrow th$. The scattering amplitude for the process is given by

$$\mathcal{A} = \frac{g}{\sqrt{2}} \left[(\kappa_t - \kappa_V) \frac{m_t \sqrt{s}}{m_W v} A \left(\frac{t}{s}, \varphi; \xi_t, \xi_b \right) + \left(\kappa_V \frac{2m_W s}{v t} + (2\kappa_t - \kappa_V) \frac{m_t^2}{m_W v} \right) B \left(\frac{t}{s}, \varphi; \xi_t, \xi_b \right) \right], \quad (2.62)$$

870 where $\kappa_V \equiv g_{HVV}/g_{HVV}^{SM}$ and $\kappa_t \equiv g_{Ht}/g_{Ht}^{SM} = y_t/y_t^{SM}$ are scaling factors that quantify
 871 possible deviations of the couplings from the SM values, Higgs-Vector boson (H-
 872 W) and Higgs-top (H-t) respectively, from the SM couplings; $s = (p_W + p_b)^2$, $t =$
 873 $(p_W - p_H)^2$, φ is the Higgs azimuthal angle around the z axis taken parallel to the
 874 direction of motion of the incoming W; A and B are functions describing the weak
 875 interaction in terms of the chiral states (ξ_t, ξ_b) of the quarks b and t . Terms that
 876 vanish in the high energy limit have been neglected as well as the Higgs and b quark
 877 masses⁹.

878 The scattering amplitude grows with energy like \sqrt{s} for $\kappa_V \neq \kappa_t$, in contrast to
 879 the SM ($\kappa_t = \kappa_V = 1$), where the first term in 2.62 cancels out and the amplitude
 880 is constant for large s ; therefore, a deviation from the SM predictions represents an
 881 enhancement in the tHq cross section. In particular, for a SM H-W coupling and a
 882 H-t coupling of inverted sign with respect to the SM ($\kappa_V = -\kappa_t = 1$) the tHq cross
 883 section is enhanced by a factor greater 10 as seen in the Figure 2.15 taken from
 884 Reference [46]; Reference [52] has reported similar enhancement results.

885 A similar analysis is valid for the W-associated channel but, in that case, the in-
 886 terference is more complicated since there are more than two contributions and an ad-
 887 ditional interference with the production of Higgs boson and a top pair process($t\bar{t}H$).
 888 The calculations are made using the so-called Diagram Removal (DR) technique where

⁹ A detailed explanation of the structure and approximations used to derive \mathcal{A} can be found in Reference [46]

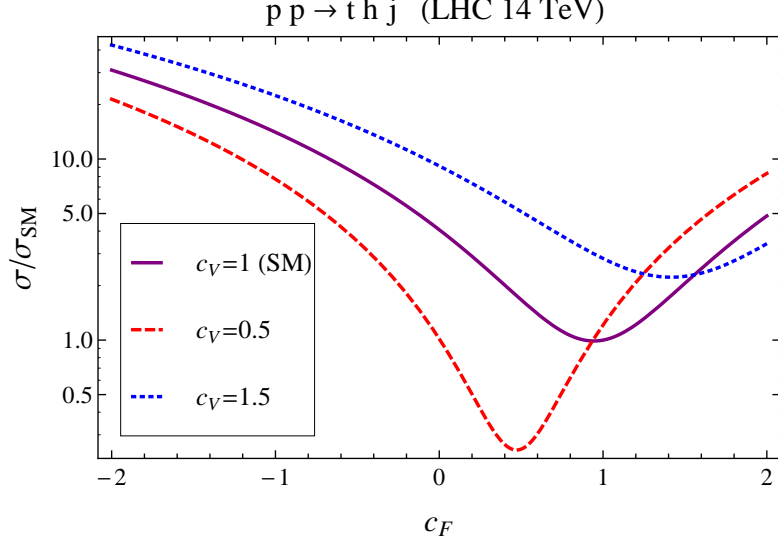


Figure 2.15: Cross section for tHq process as a function of κ_t , normalized to the SM, for three values of κ_V . In the plot c_f refers to the Higgs-fermion coupling which is dominated by the H-t coupling and represented here by κ_t . Solid, dashed and dotted lines correspond to $c_V \rightarrow \kappa_V = 1, 0.5, 1.5$ respectively. Note that for the SM ($\kappa_V = \kappa_t = 1$), the destructive effect of the interference is maximal.

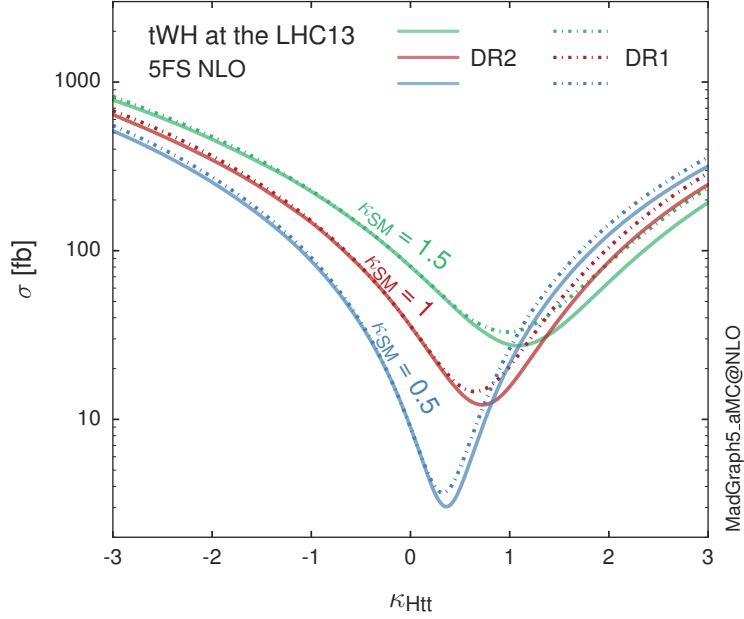


Figure 2.16: Cross section for tHW process as a function of κ_{Htt} , for three values of κ_{SM} at $\sqrt{s} = 13$ TeV. $\kappa_{Htt}^2 = \sigma_{Htt}/\sigma_{Htt}^{SM}$ is a simple re-scaling of the SM Higgs interactions.

interfering diagrams are removed (or added) from the calculations in order to evaluate the impact of the removed contributions. DR1 was defined to neglect $t\bar{t}H$ interference while DR2 was defined to take $t\bar{t}H$ interference into account [53]. As shown in Figure 2.16, the tHW cross section is enhanced from about 15 fb (SM: $\kappa_{Htt} = 1$) to about 150 fb ($\kappa_{Htt} = -1$). Differences between curves for DR1 and DR2 help to gauge the impact of the interference with $t\bar{t}H$. Results of the calculations of the tHq and tHW cross sections at $\sqrt{s} = 13$ TeV can be found in Reference [54] and a summary of the results is presented in Table 2.11.

	\sqrt{s} TeV	$\kappa_t = 1$	$\kappa_t = -1$
$\sigma^{LO}(tHq)(fb)$ [46]	8	≈ 17.4	≈ 252.7
	14	≈ 80.4	≈ 1042
$\sigma^{NLO}(tHq)(fb)$ [46]	8	$18.28^{+0.42}_{-0.38}$	$233.8^{+4.6}_{-0.0}$
	14	$88.2^{+1.7}_{-0.0}$	$982.8^{+28}_{-0.0}$
$\sigma^{LO}(tHq)(fb)$ [52]	14	≈ 71.8	≈ 893
$\sigma^{LO}(tHW)(fb)$ [52]	14	≈ 16.0	≈ 139
$\sigma^{NLO}(tHq)(fb)$ [54]	8	$18.69^{+8.62\%}_{-17.13\%}$	-
	13	$74.25^{+7.48\%}_{-15.35\%}$	$848^{+7.37\%}_{-13.70\%}$
	14	$90.10^{+7.34\%}_{-15.13\%}$	$1011^{+7.24\%}_{-13.39\%}$
$\sigma^{LO}(tHW)(fb)$ [53]	13	$15.77^{+15.91\%}_{-15.76\%}$	-
$\sigma^{NLO}DR1(tHW)(fb)$ [53]	13	$21.72^{+6.52\%}_{-5.24\%}$	≈ 150
$\sigma^{NLO}DR2(tHW)(fb)$ [53]	13	$16.28^{+7.34\%}_{-15.13\%}$	≈ 150

Table 2.11: Predicted enhancement of the tHq and tHW cross sections at LHC for $\kappa_V = 1$ and $\kappa_t = \pm 1$ at LO and NLO; the cross section enhancement of more than a factor of 10 is due to the flipping in the sign of the H-t coupling with respect to the SM one.

897

2.6 CP-mixing in tH processes

In addition to the sensitivity to sign of the H-t coupling, the tHq and tHW processes have been proposed as a tool to investigate the possibility of a H-t coupling that does

901 not conserve CP [48, 53, 55].

902 In this thesis, the sensitivity of tH processes to CP-mixing is also studied on the
 903 basis of References [48, 53] using the effective field theory framework where a generic
 904 particle (X_0) of spin-0 and a general CP violating interaction with the top quark
 905 (Htt coupling), can couple to scalar and pseudo-scalar fermionic densities. The H-W
 906 interaction is assumed to be SM-like. The Lagrangian modeling the H-t interaction
 907 is given by

$$\mathcal{L}_0^t = -\bar{\psi}_t (c_\alpha \kappa_{Htt} g_{Htt} + i s_\alpha \kappa_{Att} g_{Att} \gamma_5) \psi_t X_0, \quad (2.63)$$

908 where α is the CP-mixing phase, $c_\alpha \equiv \cos \alpha$ and $s_\alpha \equiv \sin \alpha$, κ_{Htt} and κ_{Att} are real
 909 dimensionless re-scaling parameters¹⁰ used to parametrize the magnitude of the CP-
 910 violating and CP-conserving parts of the amplitude. The model defines $g_{Htt} =$
 911 $g_{Att} = m_t/v = y_t/\sqrt{2}$ with $v \sim 246$ GeV the Higgs vacuum expectation value. In
 912 this parametrization, three special cases can be recovered

913 • CP-even coupling $\rightarrow \alpha = 0^\circ$

914 • CP-odd coupling $\rightarrow \alpha = 90^\circ$

915 • SM coupling $\rightarrow \alpha = 0^\circ$ and $\kappa_{Htt} = 1$

916 The loop induced X_0 coupling to gluons can also be described in terms of the
 917 parametrization above, according to

$$\mathcal{L}_0^g = -\frac{1}{4} \left(c_\alpha \kappa_{Hgg} g_{Hgg} G_{\mu\nu}^a G^{a,\mu\nu} + s_\alpha \kappa_{Agg} g_{Agg} G_{\mu\nu}^a \tilde{G}^{a,\mu\nu} \right) X_0. \quad (2.64)$$

918 where $g_{Hgg} = -\alpha_s/3\pi v$ and $g_{Agg} = \alpha_s/2\pi v$ and $G_{\mu\nu}$ is the gluon field strength tensors.

919 Under the assumption that the top quark dominates the gluon-fusion process at LHC

¹⁰ analog to κ_t and κ_V

energies, $\kappa_{Hgg} \rightarrow \kappa_{Htt}$ and $\kappa_{Agg} \rightarrow \kappa_{Att}$, so that the ratio between the gluon-gluon fusion cross section for X_0 and for the SM Higgs prediction can be written as

$$\frac{\sigma_{NLO}^{gg \rightarrow X_0}}{\sigma_{NLO,SM}^{gg \rightarrow H}} = c_\alpha^2 \kappa_{Htt}^2 + s_\alpha^2 \left(\kappa_{Att} \frac{g_{Agg}}{g_{Hgg}} \right)^2. \quad (2.65)$$

If the re-scaling parameters are set to

$$\kappa_{Htt} = 1, \quad \kappa_{Att} = \left| \frac{g_{Hgg}}{g_{Agg}} \right| = \frac{2}{3}. \quad (2.66)$$

the gluon-fusion SM cross section is reproduced for every value of the CP-mixing angle α ; therefore, by imposing that condition to the Lagrangian density 2.63, the CP-mixing angle is not constrained by current data. Figure 2.17 shows the NLO cross sections for t-channel tX_0 (blue) and $t\bar{t}X_0$ (red) associated production processes as a function of the CP-mixing angle α . X_0 is a generic spin-0 particle with top quark CP-violating coupling. Re-scaling factors κ_{Htt} and κ_{Att} have been set to reproduce the SM gluon-fusion cross sections.

It is interesting to notice that the tX_0 cross section is enhanced, by a factor of about 10, when a continuous rotation in the scalar-pseudoscalar plane is applied; this enhancement is similar to the enhancement produced when the H-t coupling is flipped in sign with respect to the SM ($y_t = -y_{t,SM}$ in the plot), as showed in Section 2.5. In contrast, the degeneracy in the $t\bar{t}X_0$ cross section is still present given that it depends quadratically on the H-t coupling, but more interesting is to notice that $t\bar{t}X_0$ cross section is exceeded by tX_0 cross section after $\alpha \sim 60^\circ$.

A similar parametrization can be used to investigate the tHW process sensitivity to CP-violating H-t coupling. As said in 2.5, the interference in the W-associated channel is more complicated because there are more than two contributions and also there is interference with the $t\bar{t}H$ production process.

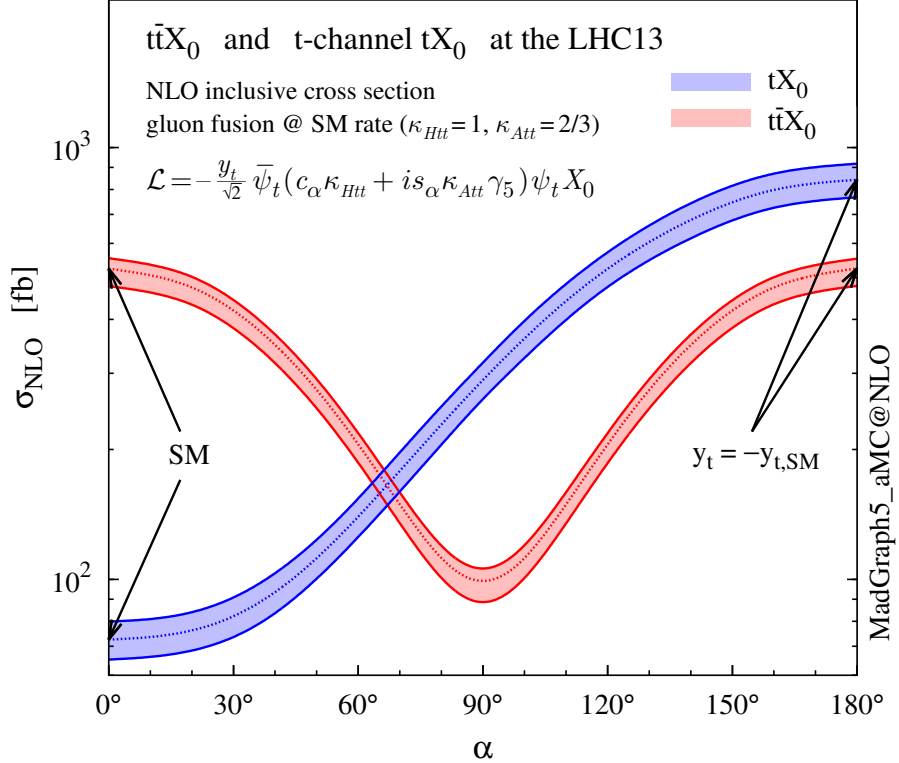


Figure 2.17: NLO cross sections for t-channel tX_0 (blue) and $t\bar{t}X_0$ (red) associated production processes as a function of the CP-mixing angle α . X_0 is a generic spin-0 particle with top quark CP-violating coupling [48].

941 Figure 2.18 shows the NLO cross sections for t-channel tX_0 (blue), $t\bar{t}X_0$ (red)
942 associated production and for the combined $tWX_0+t\bar{t}X_0+interference$ (orange) as
943 a function of the CP-mixing angle. It is clear that the effect of the interference in the
944 combined case is the lifting of the degeneracy present in the $t\bar{t}X_0$ production. The
945 constructive interference enhances the cross section from about 500 fb at SM ($\alpha = 0$)
946 to about 600 fb ($\alpha = 180^\circ \rightarrow y_t = -y_{t,SM}$).

947 An analysis combining tHq and tHW processes will be made in this thesis taking
948 advantage of the sensitivity improvement.

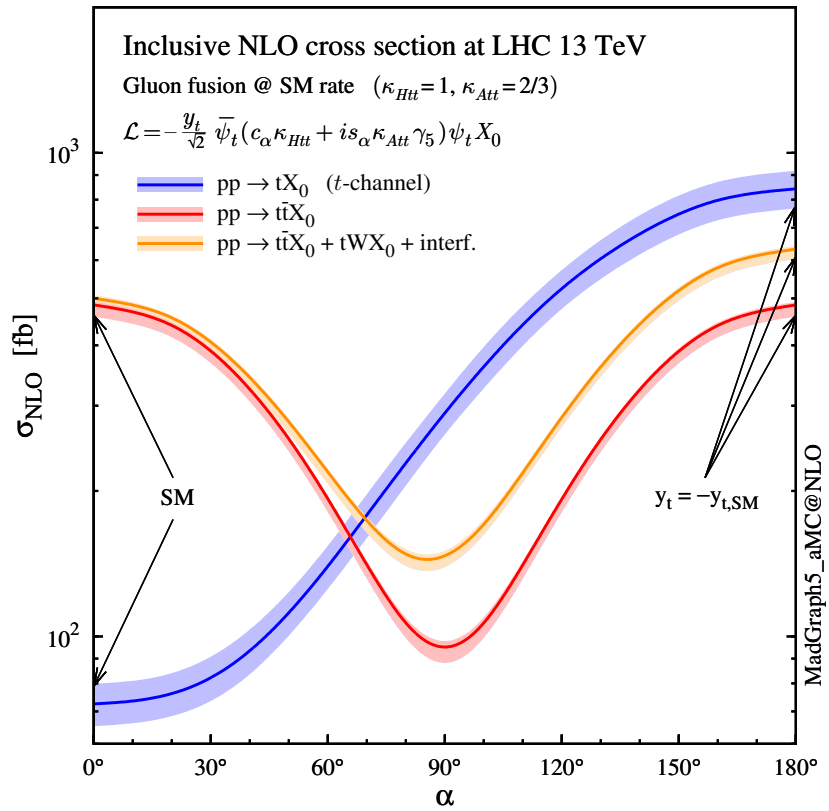


Figure 2.18: NLO cross sections for t-channel tX_0 (blue), $t\bar{t}X_0$ (red) associated production processes and combined $tWX_0 + t\bar{t}X_0$ (including interference) production as a function of the CP-mixing angle α [48].

949 **Chapter 3**

950 **The CMS experiment at the LHC**

951 **3.1 Introduction**

952 Located on the Swiss-French border, the European Council for Nuclear Research
953 (CERN) is the largest scientific organization leading particle physics research. About
954 13000 people in a broad range of roles including users, students, scientists, engineers,
955 among others, contribute to the data taking and analysis, with the goal of unveiling
956 the secrets of nature and revealing the fundamental structure of the universe. CERN
957 is also the home of the Large Hadron Collider (LHC), the largest particle accelerator
958 around the world, where protons (or heavy ions) traveling close to the speed of light,
959 are made to collide. These collisions open a window to investigate how particles (and
960 their constituents if they are composite) interact with each other, providing clues
961 about the laws of nature. This chapter presents an overview of the LHC structure
962 and operation. A detailed description of the CMS detector is offered, given that the
963 data used in this thesis have been taken with this detector.

964 3.2 The LHC

965 With 27 km of circumference, the LHC is currently the most powerful circular accelerator
 966 in the world. It is installed in the same tunnel where the Large Electron-Positron
 967 (LEP) collider was located, taking advantage of the existing infrastructure. The LHC
 968 is part of the CERN's accelerator complex composed of several successive accelerat-
 969 ing stages before the particles are injected into the LHC ring where they reach their
 970 maximum energy (see Figure 3.1).

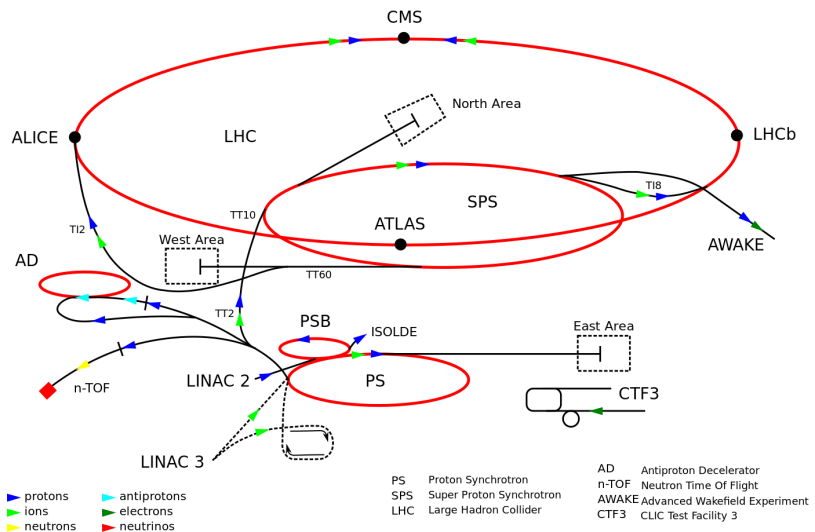


Figure 3.1: CERN accelerator complex. Blue arrows show the path followed by protons along the acceleration process [59].

971 The LHC runs in three modes depending on the particles being accelerated

- 972 • Proton-Proton collisions (pp) for multiple physics experiments.
- 973 • Lead-Lead collisions ($Pb-Pb$) for heavy ion experiments.
- 974 • Proton-Lead collisions ($p-Pb$) for quark-gluon plasma experiments.

975 In this thesis only pp collisions will be considered.

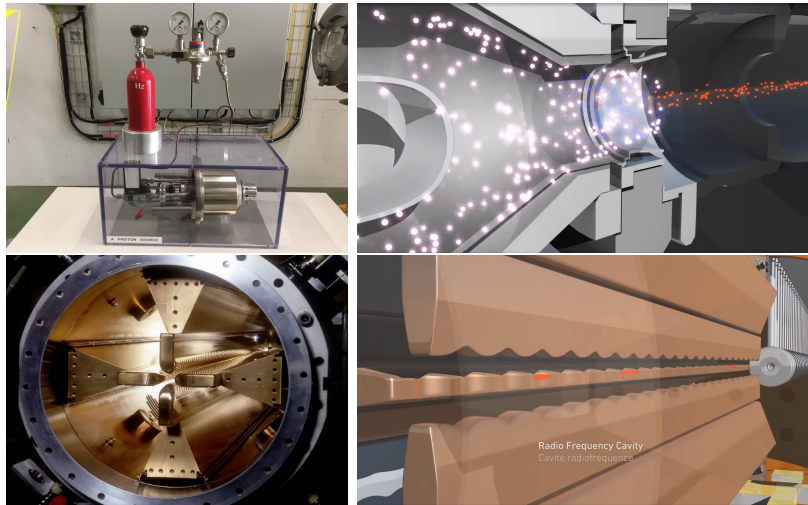


Figure 3.2: LHC protons source and the first acceleration stage. Top: the bottle contains hydrogen gas which is injected into the metal cylinder (white dots) to be broken down into electrons (blue dots) and protons (red dots); Bottom: the obtained protons are directed towards the radio frequency quadrupole which perform the first acceleration, focus the beam and create the bunches of protons. Left images are real pictures while right images are drawings [63, 64].

976 Collection of protons starts with hydrogen atoms taken from a bottle, containing
 977 hydrogen gas, and injecting them in a metal cylinder; hydrogen atoms are broken
 978 down into electrons and protons by an intense electric field (see Figure 3.2 top).
 979 The resulting protons leave the metal cylinder towards a radio frequency quadrupole
 980 (RFQ) that focus the beam, accelerates the protons and creates the packets of protons
 981 called bunches. In the RFQ, an electric field is generated by a RF wave at a frequency
 982 that matches the resonance frequency of the cavity where the electrodes are contained.
 983 The beam of protons traveling on the RFQ axis experiences an alternating electric
 984 field gradient that generates the focusing forces.

985 In order to accelerate the protons, a longitudinal time-varying electric field com-
 986 ponent is added to the system; it is done by giving the electrodes a sine-like profile as
 987 shown in Figure 3.2 bottom. By matching the speed and phase of the protons with
 988 the longitudinal electric field the bunching is performed; protons synchronized with

989 the RFQ (synchronous protons) do not feel an accelerating force, but those protons in
 990 the beam that have more (or less) energy than the synchronous proton (asynchronous
 991 protons) will feel a decelerating (accelerating) force; therefore, asynchronous protons
 992 will oscillate around the synchronous ones forming bunches of protons [61]. From the
 993 RFQ protons emerge with energy 750 keV in bunches of about 1.15×10^{11} protons [62].

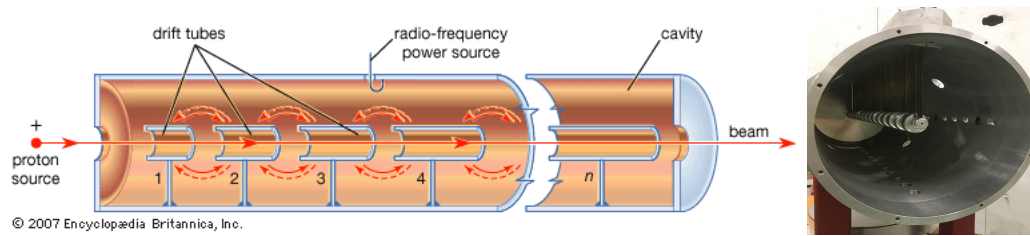


Figure 3.3: Left: drawing of the LINAC2 accelerating system at CERN. Electric fields generated by radio frequency (RF) create acceleration and deceleration zones inside the cavity; deceleration zones are blocked by drift tubes where quadrupole magnets focus the proton beam. Right: picture of a real RF cavity [65].

994 Proton bunches coming from the RFQ go to the linear accelerator 2 (LINAC2)
 995 where they are accelerated to reach 50 MeV energy. In the LINAC2 stage, acceleration
 996 is performed using electric fields generated by radio frequency which create zones
 997 of acceleration and deceleration as shown in Figure 3.3. In the deceleration zones,
 998 the electric field is blocked using drift tubes where protons are free to drift while
 999 quadrupole magnets focus the beam.

1000 The beam coming from LINAC2 is injected into the proton synchrotron booster
 1001 (PSB) to reach 1.4 GeV in energy. The next acceleration is provided at the proton
 1002 synchrotron (PS) up to 26 GeV, followed by the injection into the super proton
 1003 synchrotron (SPS) where protons are accelerated to 450 GeV. Finally, protons are
 1004 injected into the LHC where they are accelerated to the target energy of 6.5 TeV.

1005 PSB, PS, SPS and LHC accelerate protons using the same RF acceleration tech-
 1006 nique described before.

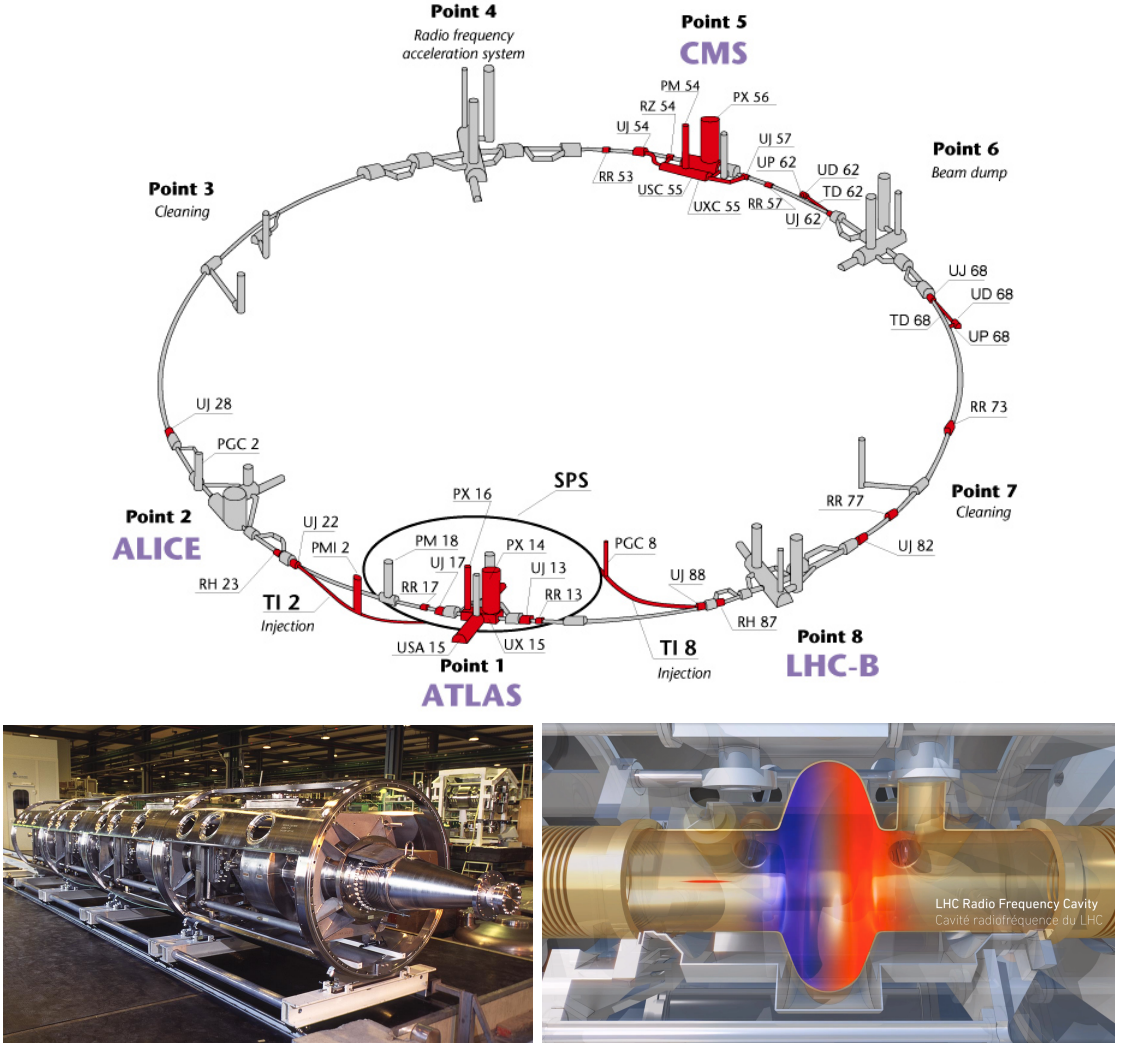


Figure 3.4: Top: LHC layout. The red zones indicate the infrastructure additions to the LEP installations, built to accommodate the ATLAS and CMS experiments which exceed the size of the former experiments located there [60]. Bottom: LHC RF cavities. A module (left picture) accommodates 4 cavities, each like the one in the right drawing, that accelerate protons and preserve the bunch structure of the beam. The color gradient pattern represents the strength of the electric field inside the cavity; red zone corresponds to the maximum of the oscillation electric field while the blue zone corresponds to the minimum. [64, 66]

1007 The LHC has a system of 16 RF cavities located in the so-called point 4, as
 1008 shown in Figure 3.4 top, tuned at a frequency of 400 MHz. The bottom side of
 1009 Figure 3.4 shows a picture of a RF module composed of 4 RF cavities working in a
 1010 superconducting state at 4.5 K; also, a representation of the accelerating electric field

1011 that accelerates the protons in the bunch is shown. The maximum of the oscillating
 1012 electric field (red region) picks the proton bunches at the entrance of the cavity
 1013 and keeps accelerating them through the whole cavity. The protons are carefully
 1014 timed so that in addition to the acceleration effect the bunch structure of the beam
 1015 is preserved.

1016 While protons are accelerated in one section of the LHC ring, where the RF cavities
 1017 are located, in the rest of their path they have to be kept in the curved trajectory
 1018 defined by the LHC ring. Technically, LHC is not a perfect circle; RF, injection, beam
 1019 dumping, beam cleaning and sections before and after the experimental points where
 1020 protons collide are all straight sections. In total, there are 8 arcs 2.45 km long each
 1021 and 8 straight sections 545 m long each. In order to curve the proton's trajectory in
 1022 the arc sections, superconducting dipole magnets are used.

1023 Inside the LHC ring, there are two proton beams traveling in opposite directions
 1024 in two separated beam pipes; the beam pipes are kept at ultra-high vacuum ($\sim 10^{-9}$
 1025 Pa) to ensure that there are no particles that interact with the proton beams. The
 1026 superconducting dipole magnets used in LHC are made of a NbTi alloy, capable of
 1027 transporting currents of about 12000 A when cooled at a temperature below 2K using
 1028 liquid helium (see Figure 3.5).

1029

1030 Protons in the arc sections of LHC feel a centripetal force exerted by the dipole
 1031 magnets which is perpendicular to the beam trajectory; The magnitude of magnetic
 1032 field needed can be found assuming that protons travel at $v \approx c$, using the standard
 1033 values for proton mass and charge and the LHC radius, as

$$F_m = \frac{mv^2}{r} = qBv \rightarrow B = 8.33T \quad (3.1)$$

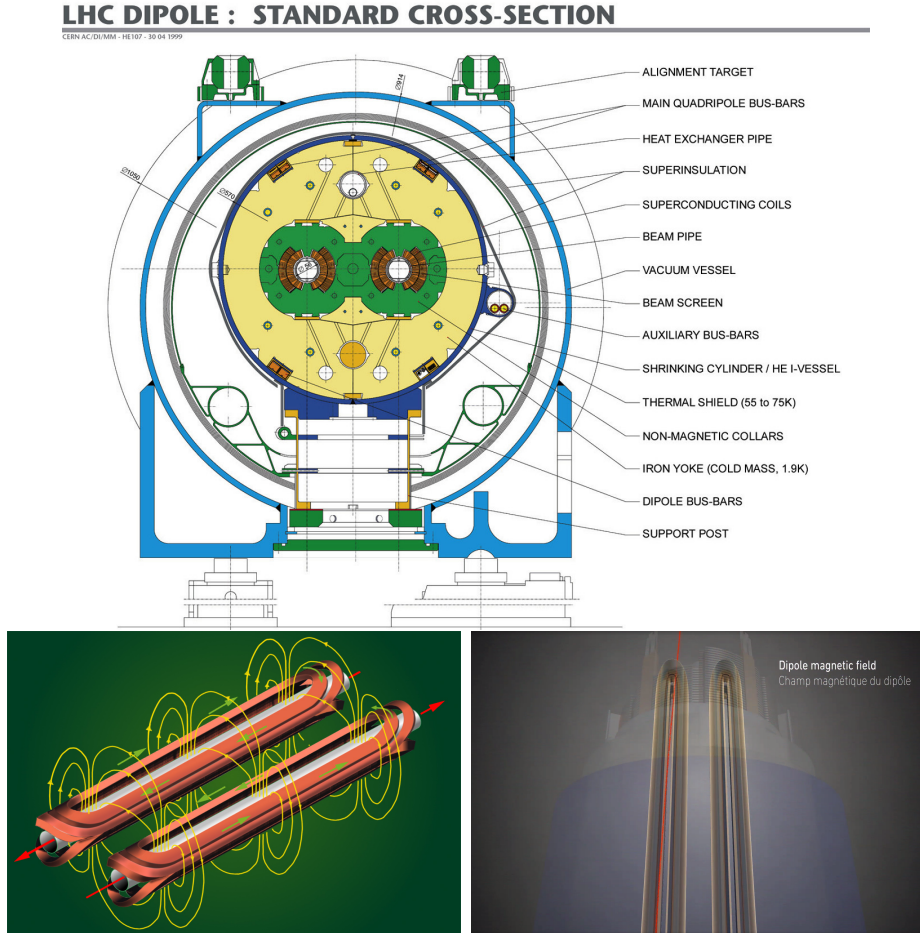


Figure 3.5: Top: LHC dipole magnet transverse view; cooling, shielding and mechanical support are indicated. Bottom left: Magnetic field generated by the dipole magnets; note that the direction of the field inside one beam pipe is opposite with respect to the other beam pipe which guarantee that both proton beams are curved in the same direction towards the center of the ring. The effect of the dipole magnetic field on the proton beam is represented on the bottom right side [64, 67, 68].

1034 which is about 100000 times the Earth's magnetic field. A representation of the mag-
 1035 netic field generated by the dipole magnets is shown on the bottom left side of Figure
 1036 3.5. The bending effect of the magnetic field on the proton beam is shown on the
 1037 bottom right side of Figure 3.5. Note that the dipole magnets are not curved; the
 1038 arc section of the LHC ring is composed of straight dipole magnets of about 15 m.
 1039 In total there are 1232 dipole magnets along the LHC ring.

1040

1041 In addition to bending the beam trajectory, the beam has to be focused so it stays
 1042 inside the beam pipe. The focusing is performed by quadrupole magnets installed in
 1043 a different straight section; in total 858 quadrupole magnets are installed along the
 1044 LHC ring. Other effects like electromagnetic interaction among bunches, interaction
 1045 with electron clouds from the beam pipe, the gravitational force on the protons, dif-
 1046 ferences in energy among protons in the same bunch, among others, are corrected
 1047 using sextupole and other magnetic multipoles.

1048

1049 The two proton beams inside the LHC ring are made of bunches with a cylindrical
 1050 shape of about 7.5 cm long and about 1 mm in diameter; when bunches are close
 1051 to the collision point (CP), the beam is focused up to a diameter of about $16 \mu\text{m}$ in
 1052 order to maximize the number of collisions per unit area and per second, known as
 1053 luminosity (L). Luminosity can be calculated using

$$L = fn \frac{N_1 N_2}{4\pi\sigma_x\sigma_y} \quad (3.2)$$

1054 where f is the revolution frequency, n is the number of bunches per beam, N_1 and
 1055 N_2 are the numbers of protons per bunch (1.5×10^{11}), σ_x and σ_y are the gaussian
 1056 transverse sizes of the bunches. The expected luminosity is about

$$f = \frac{v}{2\pi r_{LHC}} \approx \frac{3 \times 10^8 \text{ m/s}}{27 \text{ km}} \approx 11.1 \text{ kHz},$$

$$n = 2808$$

$$N_1 = N_2 = 1.5 \times 10^{11}$$

$$\sigma_x = \sigma_y = 16 \mu\text{m}$$

$$L = 1.28 \times 10^{34} \text{ cm}^{-2} \text{ s}^{-1} = 1.28 \times 10^{-5} \text{ fb}^{-1} \text{ s}^{-1} \quad (3.3)$$

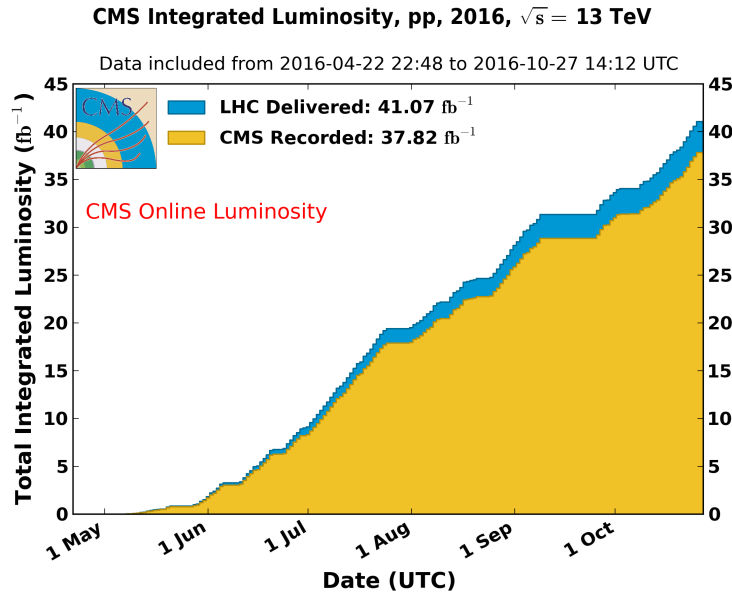


Figure 3.6: Integrated luminosity delivered by LHC and recorded by CMS during 2016. The difference between the delivered and the recorded luminosity is due to fails and issues occurred during the data taking in the CMS experiment [69].

1057 Luminosity is a fundamental aspect of LHC given that the bigger luminosity the
 1058 bigger number of collisions, which means that for processes with a very small cross
 1059 section the number of expected occurrences is increased and so the chances of being
 1060 detected. The integrated luminosity, i.e., the total luminosity, collected by the CMS
 1061 experiment during 2016 is shown in Figure 3.6; the data analyzed in this thesis cor-
 1062 responds to an integrated luminosity of 35.9 fb^{-1} at a center of mass-energy $\sqrt{s} = 13$
 1063 TeV.

1064

1065 A way to increase L is increasing the number of bunches in the beam. Currently, the
 1066 separation between two consecutive bunches in the beam is 7.5 m which corresponds
 1067 to a time separation of 25 ns. In the full LHC ring the allowed number of bunches is
 1068 $n = 27\text{km}/7.5\text{m} = 3600$; however, there are some gaps in the bunch pattern intended

1069 for preparing the dumping and injection of the beam, thus, the proton beams are
1070 composed of 2808 bunches.

1071

1072 Once the proton beams reach the desired energy, they are brought to cross each other
1073 producing proton-proton collisions. The bunch crossing happens in precise places
1074 where the four LHC experiments are located, as seen in the top of Figure 3.7. In
1075 2008, the first set of collisions involved protons with $\sqrt{s} = 7$ TeV; the energy was
1076 increased to 8 TeV in 2012 and to 13 TeV in 2015.

1077

1078 CMS and ATLAS experiments, which are multi-purpose experiments, are enabled
1079 to explore physics in any of the collision modes. LHCb experiment is optimized
1080 to explore bottom quark physics, while ALICE is optimized for heavy ion collisions
1081 searches; TOTEM and LHCf are dedicated to forward physics studies; MoEDAL (not
1082 indicated in the Figure) is intended for monopoles or massive pseudo stable particles
1083 searches.

1084

1085 At the CP there are two interesting details that need to be addressed. The first one
1086 is that the bunch crossing does not occur head-on but at a small crossing angle θ_c
1087 (280 μ rad in CMS and ATLAS) as shown in the bottom side of Figure 3.7, affecting
1088 the overlapping between bunches; the consequence is a reduction of about 17% in
1089 the luminosity (represented by a factor not included in eqn. 3.2). The second one
1090 is the occurrence of multiple pp collisions in the same bunch crossing; this effect is
1091 called pile-up (PU). A fairly simple estimation of the PU follows from estimating the
1092 probability of collision between two protons, one from each of the bunches in course
1093 of collision; it depends roughly on the ratio of proton size and the cross section of the

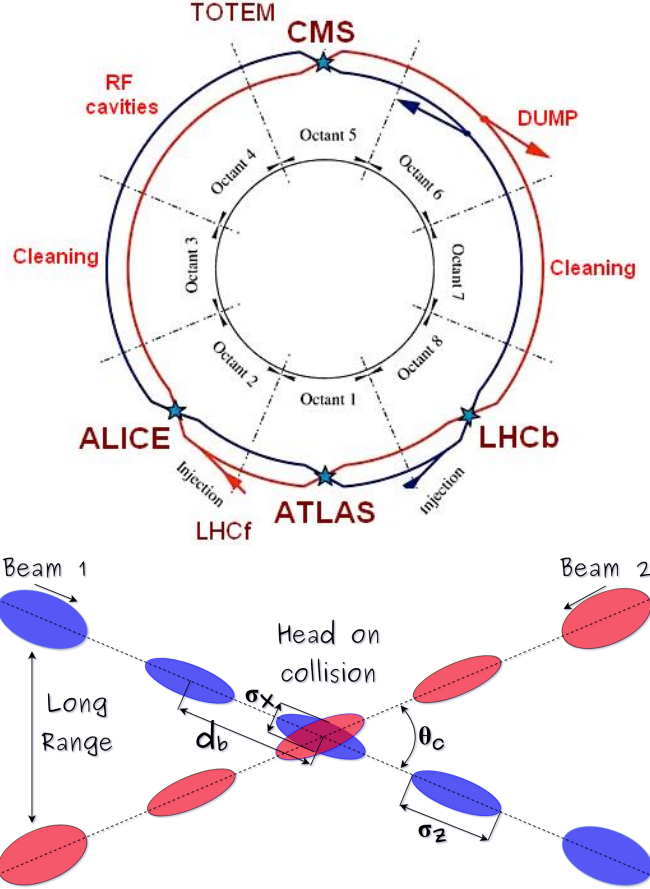


Figure 3.7: Top: LHC interaction points. Bunch crossing occurs where the LHC experiments are located [70]. Sections indicated as cleaning are dedicated to collimate the beam in order to protect the LHC ring from collisions with protons in very spreaded bunches. Bottom: bunch crossing scheme. Since the bunch crossing is not perfectly head-on, the luminosity is reduced in a factor of 17%; adapted from Reference [82].

1094 bunch in the interaction point, i.e.,

$$P(pp\text{-}collision) \sim \frac{d_{proton}^2}{\sigma_x \sigma_y} = \frac{(1\text{fm})^2}{(16\mu\text{m})^2} \sim 4 \times 10^{-21} \quad (3.4)$$

1095 however, there are $N = 1.15 \times 10^{11}$ protons in a bunch, thus the estimated number of
1096 collisions in a bunch crossing is

$$PU = N^2 * P(pp\text{-}collision) \sim 50 \text{ pp-collision per bunch crossing}, \quad (3.5)$$

about 20 of those pp collisions are inelastic. Each collision generates a vertex, but only the most energetic is considered as a primary vertex; the rest are considered as PU vertices. A multiple pp collision event in a bunch crossing at CMS is showed in Figure 3.8. Unstable particles outgoing from the primary vertex will eventually decay; this decay vertex is known as a secondary vertex.

1102

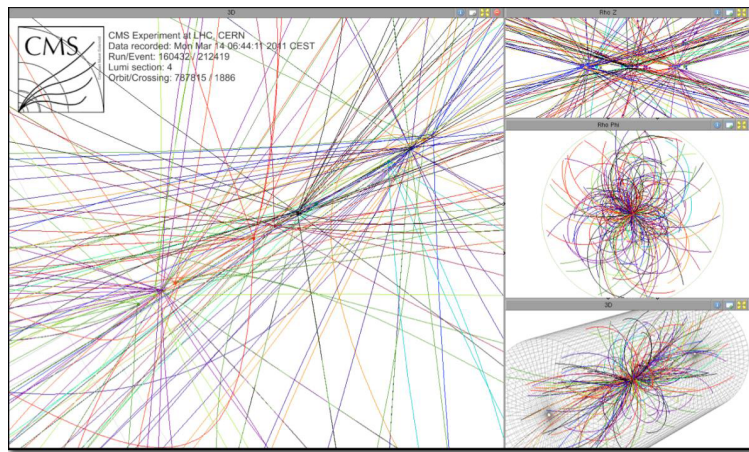


Figure 3.8: Multiple pp collision bunch crossing at CMS. Only the most energetic vertex is considered and the rest are catalogued as PU vertices [71].

1103 Next section presents a description of the CMS detector which it is the detector used
1104 to collect the data used in this thesis.

1105 3.3 The CMS experiment

1106 CMS is a general-purpose detector designed to conduct research in a wide range
1107 of physics from the standard model to new physics like extra dimensions and dark
1108 matter. Located at the point 5 in the LHC layout as shown in Figure 3.4, CMS is
1109 composed of several detection systems distributed in a cylindrical structure; in total,
1110 CMS weights about 12500 tons in a very compact 21.6 m long and 14.6 m diameter
1111 cylinder. It was built in 15 separate sections at the ground level and lowered to the

1112 cavern individually to be assembled. A complete and detailed description of the CMS
 1113 detector and its components is given in Reference [72] on which this section is based
 1114 on.

1115

1116 Figure 3.9 shows the layout of the CMS detector. The design is driven by the require-
 1117 ments on the identification, momentum resolution and unambiguous charge determi-
 1118 nation of the muons; therefore, a large bending power is provided by the solenoid
 1119 magnet made of superconducting cable capable to generate a 3.8 T magnetic field.
 1120 The detection system is composed of (from the innermost to the outermost)

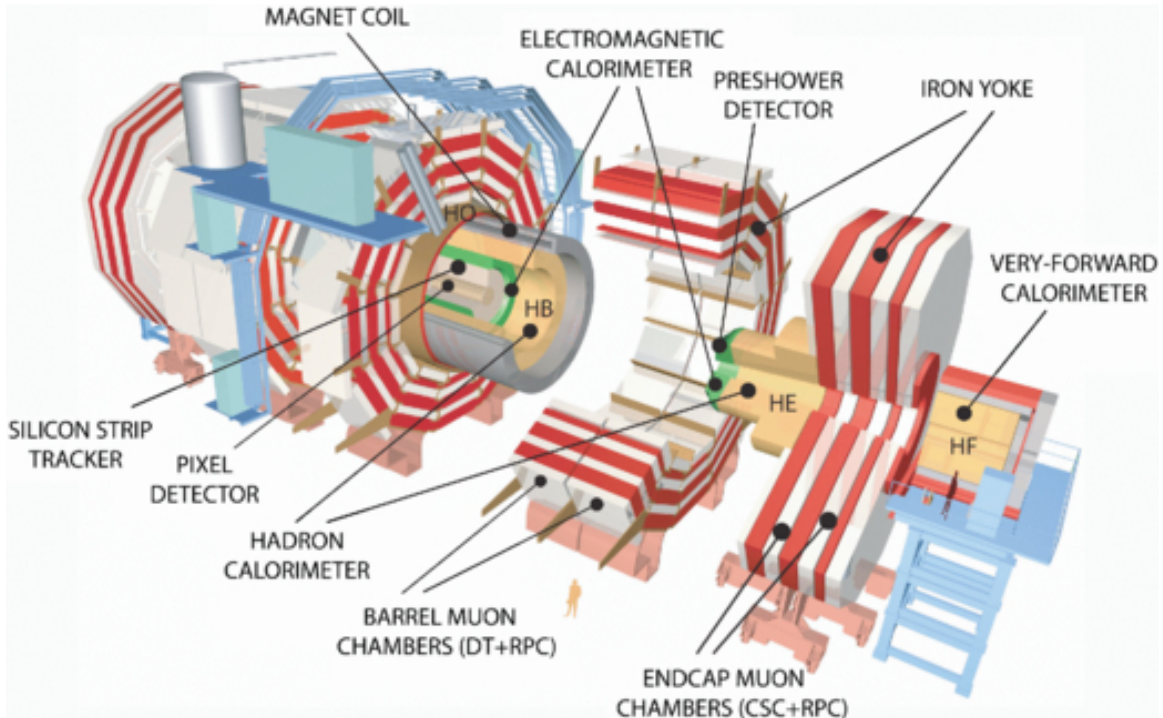


Figure 3.9: Layout of the CMS detector. The several subdetectors are indicated. The central region of the detector is referred as the Barrel section while the endcaps are referred as the forward sections. [73].

- 1121 • Pixel detector.
 1122 • Silicon strip tracker.

- 1123 • Preshower detector.
- 1124 • Electromagnetic calorimeter.
- 1125 • Hadronic calorimeter.
- 1126 • Muon chambers (Barrel and endcap)

1127 The central region of the detector is commonly referred as the barrel section while the
 1128 endcaps are referred as the forward sections of the detector; thus, each subdetector
 1129 is composed of a barrel section and a forward section.

1130 3.3.1 Coordinate system

1131 The coordinate system used by CMS is centered in the geometrical center of the
 1132 detector which is the same as the CP as shown in Figure 3.10. The z -axis is parallel
 1133 to the beam direction, while the Y -axis pointing vertically upward, and the X -axis
 1134 pointing radially inward toward the center of the LHC.

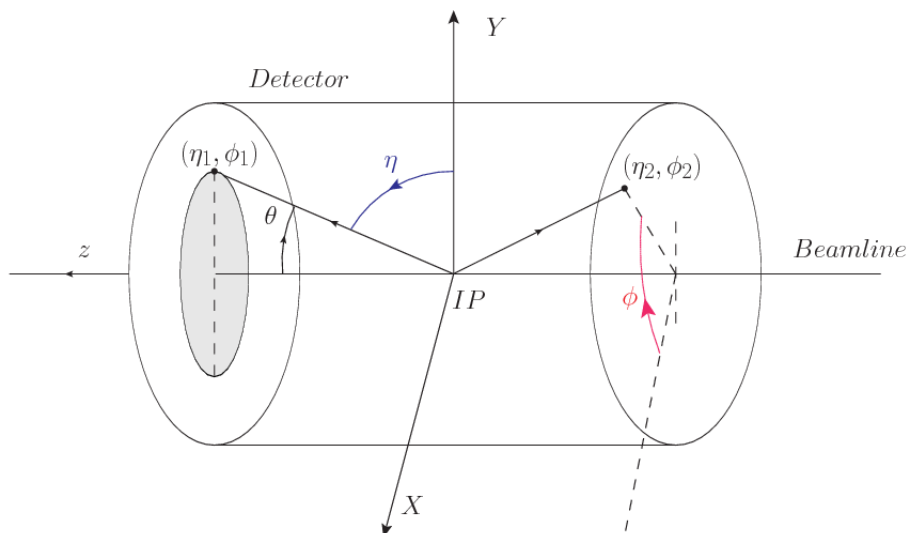


Figure 3.10: CMS detector coordinate system.

1135 In addition to the common cartesian and cylindrical coordinate systems, two coor-
 1136 dinates are of particular utility in particle physics: rapidity (y) and pseudorapidity
 1137 (η), defined in connection to the polar angle θ , energy and longitudinal momentum
 1138 component (momentum along the z -axis) according to

$$y = \frac{1}{2} \ln \frac{E + p_z}{E - p_z} \quad \eta = -\ln \left(\tan \frac{\theta}{2} \right) \quad (3.6)$$

1139 Rapidity is related to the angle between the XY -plane and the direction in which the
 1140 products of a collision are emitted; it has the nice property that the difference between
 1141 the rapidities of two particles is invariant with respect to Lorentz boosts along the z -
 1142 axis. Thus, data analysis becomes more simple when based on rapidity; however, it is
 1143 not simple to measure the rapidity of highly relativistic particles, as those produced
 1144 after pp collisions. Under the highly relativistic motion approximation, y can be
 1145 rewritten in terms of the polar angle, concluding that rapidity is approximately equal
 1146 to the pseudorapidity defined above, i.e., $y \approx \eta$. Note that η is easier to measure than y
 1147 given the direct relationship between the former and the polar angle. Angular distance
 1148 between two objects in the detector (ΔR) is defined in terms of their coordinates
 1149 $(\eta_1, \phi_1), (\eta_2, \phi_2)$ as

$$\Delta R = \sqrt{(\Delta\eta)^2 - (\Delta\phi)^2} \quad (3.7)$$

1150 3.3.2 Pixels detector

1151 The CMS tracking system is designed to provide a precise measurement of the tra-
 1152 jectory (*track*) followed by the charged particles created after the pp collisions; also,
 1153 the precise reconstruction of the primary and secondary origins (*vertices*) is expected
 1154 in an environment where, each 25 ns, the bunch crossing produce about 20 inelastic
 1155 collisions and about 1000 particles. An increment in the luminosity is ongoing which

1156 implies that the PU will increase accordingly.

1157

1158 The pixel detector was replaced during the 2016-2017 extended year-end technical
1159 stop, due to the increasingly challenging operating conditions like the higher particle
1160 flow and more radiation harsh environment, among others. The new one is responding
1161 as expected, reinforcing its crucial role in the successful way to fulfill the new LHC
1162 physics objectives after the discovery of the Higgs boson. The last chapter of this
1163 thesis is dedicated to describe my contribution to the *Forward Pixel Phase 1 upgrade*.

1164

1165 The current pixel detector is composed of 1856 silicon pixel detector modules orga-
1166 nized in four-barrel layers in the central region and three disks in the forward region;
1167 it is designed to record efficiently and with high precision, up to $10\mu\text{m}$ in the XY -
1168 plane and $20\mu\text{m}$ in the z -direction, the first four space-points (*hits*) near to the CP
1169 region (see Figure 3.11 left side) in the range $|\eta| \leq 2.5$. The first barrel layer is located
1170 at a radius of 30 mm from the beamline, while the fourth layer is located at a radius
1171 of 160 mm closer to the strip tracker inner barrel layer (see Section 3.3.3) in order to
1172 reduce the rate of fake tracks. The high granularity of the detector is represented in
1173 its about 123 Mpixels, each of size $100 \times 150\mu\text{m}^2$, which is almost twice the channels
1174 of the old detector. The transverse momentum resolution of tracks can be measured
1175 with a resolution of 1-2% for muons of $p_T = 100$ GeV.

1176

1177 Some of the improvements with respect to the previous pixel detector include a higher
1178 average tracking efficiency and lower average fake rate as well as higher track impact
1179 parameter resolution which is fundamental in order to increase the efficiency in the
1180 identification of jets originating from b quarks (b-tagging). A significant source of
1181 improvement comes from the overall reduction in the material budget of the detector

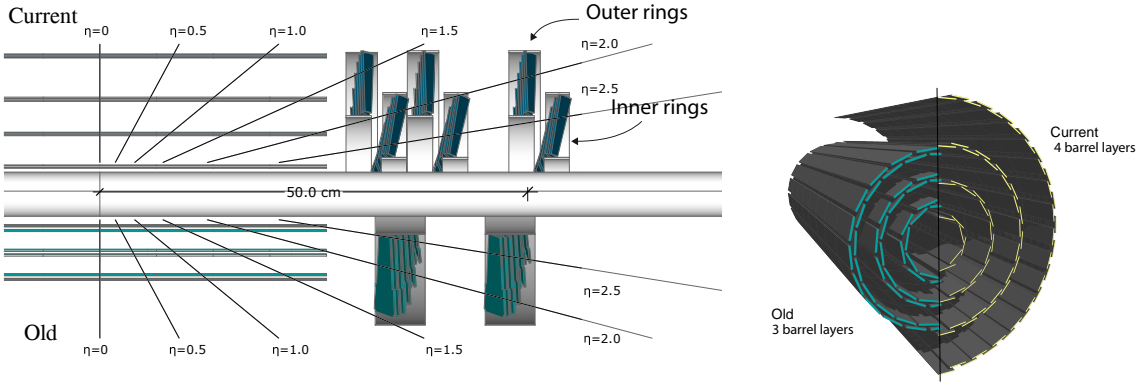


Figure 3.11: CMS pixel detector schematic view. Left: layout comparing the layers and disks in the old and current pixel detectors. Right: Transverse-oblique view comparing the pixel barrel layers in the two [75].

1182 which results in fewer photon conversions and less multiple scattering from charged
 1183 particles.

1184 3.3.3 Silicon strip tracker

1185 The silicon strip tracker (SST) is the second stage in the CMS tracking system. The
 1186 top side of Figure 3.12 shows a schematic of the SST. The inner tracker region is com-
 1187 posed of the tracker inner barrel (TIB) and the tracker inner disks (TID) covering the
 1188 region $r < 55$ cm and $|z| < 118$ cm. The TIB is composed of 4 layers while the TID
 1189 is composed of 3 disks at each end. The silicon sensors in the inner tracker are 320
 1190 μm thick, providing a resolution of about 13-38 μm in the $r\phi$ position measurement.

1191

1192 The modules indicated in blue in the schematic view of Figure 3.12 are two modules
 1193 mounted back-to-back and rotated in the plane of the module by a *stereo* angle of
 1194 100 mrad; the hits from these two modules, known as *stereo hits*, are combined to
 1195 provide a measurement of the second coordinate (z in the barrel and r on the disks)
 1196 allowing the reconstruction of hit positions in 3-D.

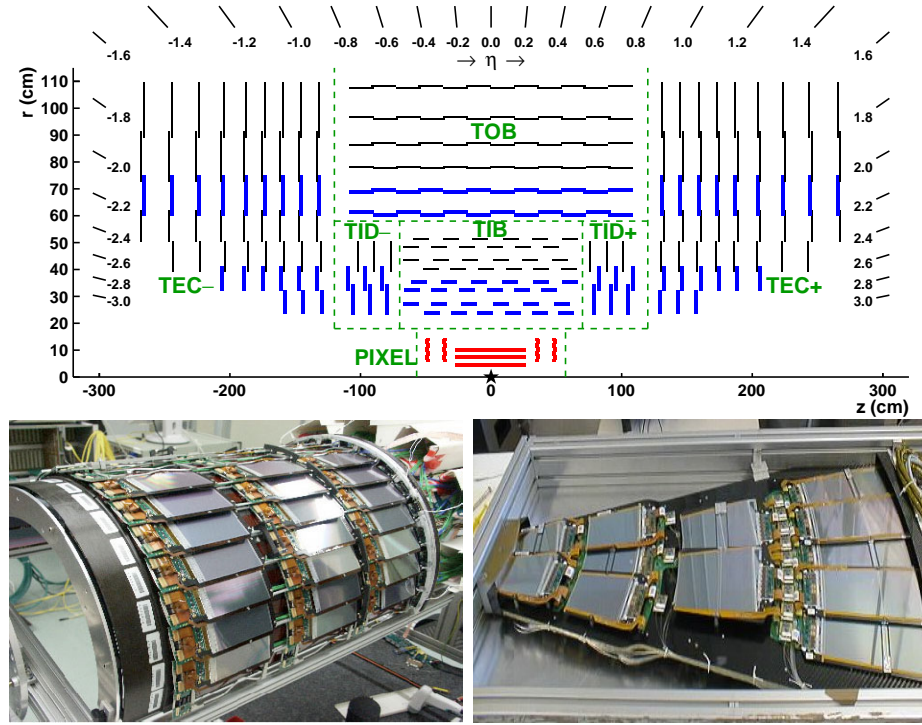


Figure 3.12: Top: CMS Silicon Strip Tracker (SST) schematic view. The SST is composed of the tracker inner barrel (TIB), the tracker inner disks (TID), the tracker outer barrel (TOB) and the tracker endcaps (TEC). Each part is made of silicon strip modules; the modules in blue represent two modules mounted back-to-back and rotated in the plane of the module by a stereo angle of 120 mrad in order to provide a 3-D reconstruction of the hit positions. Bottom: pictures of the TIB (left) and TEC (right) modules [76–78].

1197

1198 The outer tracker region is composed of the tracker outer barrel (TOB) and the
 1199 tracker endcaps (TEC). The six layers of the TOB offer coverage in the region $r > 55$
 1200 cm and $|z| < 118$ cm, while the 9 disks of the TEC cover the region $124 < |z| < 282$
 1201 cm. The resolution offered by the outer tracker is about $13\text{--}38 \mu\text{m}$ in the $r\phi$ position
 1202 measurement. The inner four TEC disks use silicon sensors $320 \mu\text{m}$ thick; those in
 1203 the TOB and the outer three TEC disks use silicon sensors of $500 \mu\text{m}$ thickness. The
 1204 silicon strips run parallel to the z -axis and the distance between strips varies from 80
 1205 μm in the inner TIB layers to $183 \mu\text{m}$ in the inner TOB layers; in the endcaps the
 1206 wedge-shaped sensors with radial strips, whose pitch range between $81 \mu\text{m}$ at small

1207 radii and 205 μm at large radii.

1208

1209 The whole SST has 15148 silicon modules, 9.3 million silicon strips and cover a total
 1210 active area of about 198 m^2 .

1211 3.3.4 Electromagnetic calorimeter

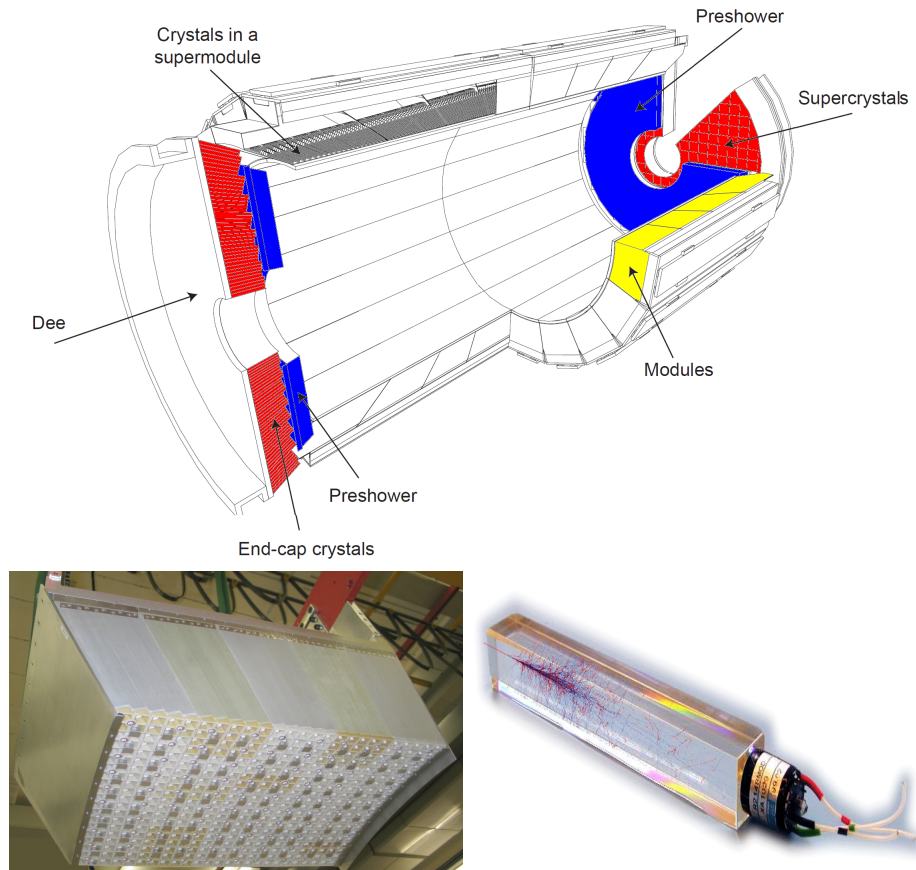


Figure 3.13: Top: CMS ECAL schematic view. Bottom: Module equipped with the crystals (left); ECAL crystal(right).

1212 The CMS electromagnetic calorimeter (ECAL) is designed to measure the energy of
 1213 electrons and photons. It is composed of 75848 lead tungstate crystals which have a
 1214 short radiation length (0.89 cm) and fast response, since 80% of the light is emitted

1215 within 25 ns; however, they are combined with Avalanche photodiodes (APDs) as
 1216 photodetectors given that crystals themselves have a low light yield ($30\gamma/\text{MeV}$). A
 1217 schematic view of the ECAL is shown in Figure 3.13.

1218

1219 Energy is measured when electrons and photons are absorbed by the crystals which
 1220 generates an electromagnetic *shower*, as seen in bottom right picture of the Figure
 1221 3.13; the shower is seen as a *cluster* of energy which depending on the amount of en-
 1222 ergy deposited can involve several crystals. The ECAL barrel (EB) covers the region
 1223 $|\eta| < 1.479$, using crystals of depth of 23 cm and $2.2 \times 2.2 \text{ cm}^2$ transverse section;
 1224 the ECAL endcap (EE) covers the region $1.479 < |\eta| < 3.0$ using crystals of depth
 1225 22 cm and transverse section of $2.86 \times 2.86 \text{ cm}^2$; the photodetectors used are vacuum
 1226 phototriodes (VPTs). Each EE is divided in two structures called *Dees*.

1227

1228 In front of the EE, it is installed the preshower detector (ES) which covers the region
 1229 $1.653 < |\eta| < 2.6$. The ES provides a precise measurement of the position of electro-
 1230 magnetic showers, which allows to distinguish electrons and photons signals from π^0
 1231 decay signals. The ES is composed of a layer of lead absorber followed by a layer of
 1232 plastic scintillators

1233 3.3.5 Hadronic calorimeter

1234 Hadrons are not absorbed by the ECAL but by the hadron calorimeter (HCAL),
 1235 which is made of a combination of alternating brass absorber layers and silicon photo-
 1236 multiplier(SiPM) layers; therefore, particles passing through the scintillator material
 1237 produce showers, as in the ECAL, as a result of the inelastic scattering of the hadrons
 1238 with the detector material. Since the particles are not absorbed in the scintillator,

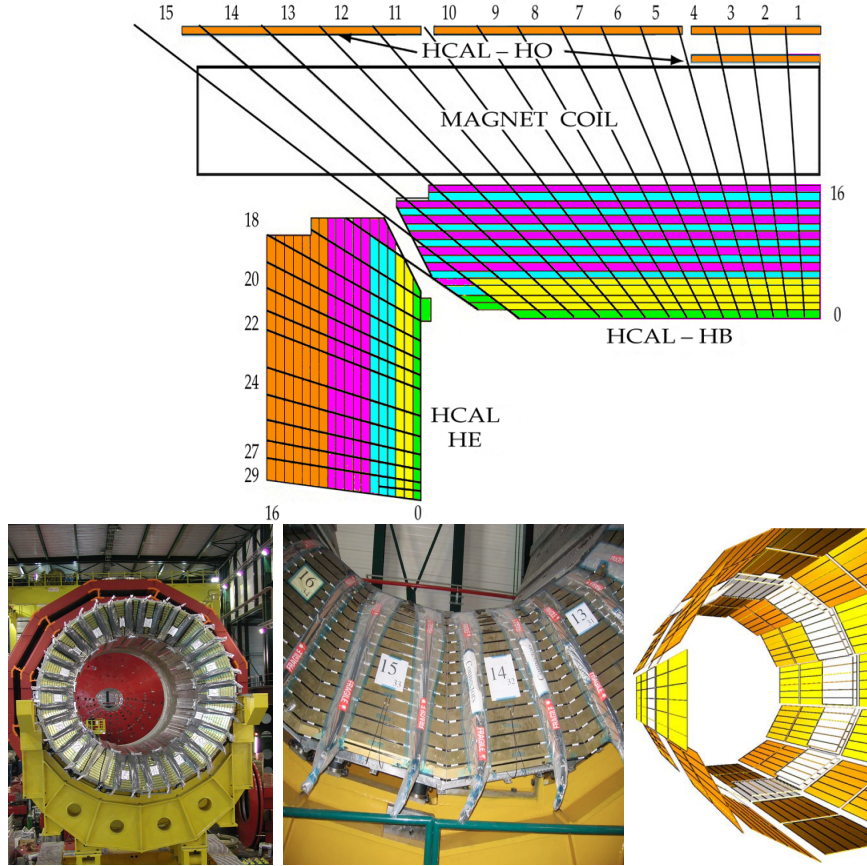


Figure 3.14: Top: CMS HCAL schematic view, the colors indicate the layers that are grouped into the same readout channels. Bottom: picture of a section of the HB; the absorber material is the golden region and scintillators are placed in between the absorber material (left and center). Schematic view of the HO (right). [79, 80]

1239 their energy is sampled; therefore the total energy is not measured but estimated from
 1240 the energy clusters, which reduce the resolution of the detector. Brass was chosen
 1241 as the absorber material due to its short interaction length ($\lambda_I = 16.42\text{cm}$) and its
 1242 non-magnetivity. Figure 3.14 shows a schematic view of the CMS HCAL.

1243

1244 The HCAL is divided into four sections; the Hadron Barrel (HB), the Hadron Outer
 1245 (HO), the Hadron Endcap (HE) and the Hadron Forward (HF) sections. The HB
 1246 covers the region $0 < |\eta| < 1.4$, while the HE covers the region $1.3 < |\eta| < 3.0$. The HF,

1247 made of quartz fiber scintillator and steel as absorption material, covers the forward
 1248 region $3.0 < |\eta| < 5.2$. Both the HB and HF are located inside the solenoid. The HO
 1249 is placed outside the magnet as an additional layer of scintillators with the purpose
 1250 of measure the energy tails of particles passing through the HB and the magnet (see
 1251 Figure 3.14 top and bottom right). The upgrades made to the HCAL during the
 1252 technical stop 2016-2017 consisted in the replacement of the photo transducer, in
 1253 order to improve the efficiency.

1254 3.3.6 Superconducting solenoid magnet

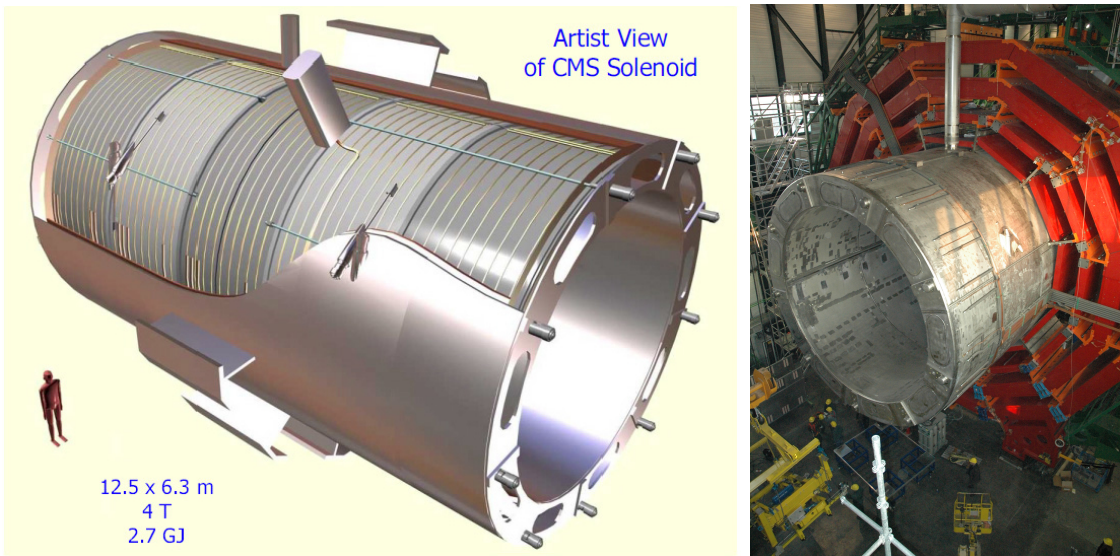


Figure 3.15: Artistic representation of the CMS solenoid magnet(left). The magnet is supported on an iron yoke (right) which also serves as the house of the muon detector and as mechanical support for the whole CMS detector [74].

1255 The superconducting magnet installed in the CMS detector is designed to provide
 1256 an intense and highly uniform magnetic field in the central part of the detector. In
 1257 fact, the tracking system takes advantage of the bending power of the magnetic field
 1258 to measure with precision the momentum of the particles that traverse it; the unam-
 1259 biguous determination of the sign for high momentum muons was a driven principle

1260 during the design of the magnet. The magnet has a diameter of 6.3 m, a length of 12.5
 1261 m and a cold mass of 220 t; the generated magnetic field reaches a strength of 3.8T.
 1262 Since it is made of Ni-Tb superconducting cable it has to operate at a temperature
 1263 of 4.7 K by using a helium cryogenic system; the current circulating in the cables
 1264 reaches 18800 A under normal running conditions. The left side of Figure 3.15 shows
 1265 an artistic view of the CMS magnet, while the right side shows a transverse view of
 1266 the cold mass where the winding structure is visible.

1267

1268 The yoke (see Figure 3.15), composed of 5 barrel wheels and 6 endcap disks made
 1269 of iron, serves not only as the media for magnetic flux return but also provides the
 1270 house for the muon detector system and structural stability to the full detector.

1271 3.3.7 Muon system

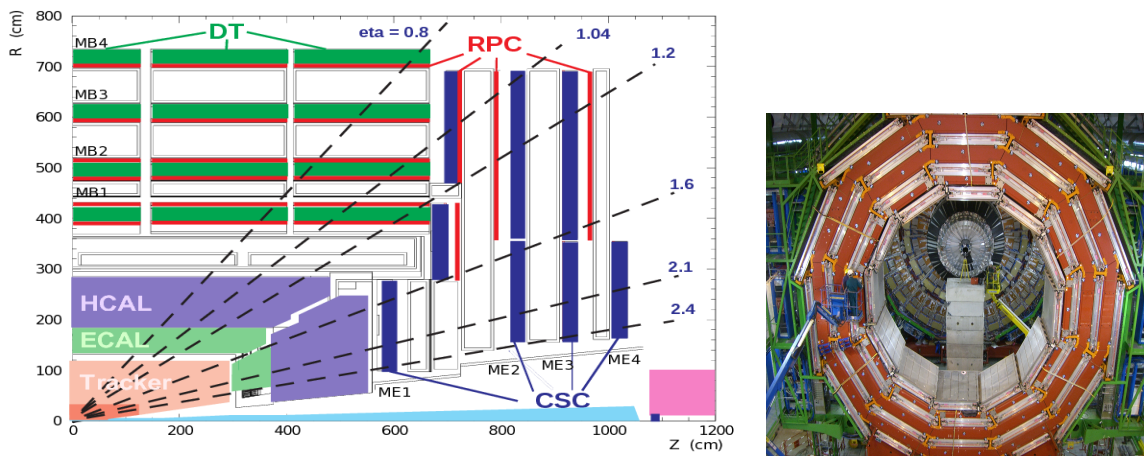


Figure 3.16: Left: CMS muon system schematic view; Right: one of the yoke rings with the muon DTs and RPCs installed; in the back it is possible to see the muon endcap [81].

1272 Muons are the only charged particles able to pass through all the CMS detector due
 1273 to their low ionization energy loss; thus, muons can be separated easily from the
 1274 high amount of particles produced in a pp collision. Also, muons are expected to be

1275 produced in the decay of several new particles; therefore, a good detection of muons
 1276 was on the leading principles when designing the CMS detector.

1277

1278 The CMS muon detection system (muon spectrometer) is embedded in the return
 1279 yoke as seen in Figure 3.16. It is composed of three different detector types, the drift
 1280 tube chambers (DT), Cathode strip chambers (CSC), and resistive plate chambers
 1281 (RPC); DT are located in the central region $\eta < 1.2$ arranged in four layers of drift
 1282 chambers filled with an Ar/CO₂ gas mixture.

1283

1284 The muon endcaps are made of CSCs covering the region $\eta < 2.4$ and filled with a
 1285 mixture of Ar/CO₂/CF₄. The reason behind using a different detector type lies on
 1286 the different conditions in the forward region like the higher muon rate and higher
 1287 residual magnetic field compared to the central region.

1288

1289 The third type of detector used in the muon system is a set of four disks of RPCs
 1290 working in avalanche mode. The RPCs provide good spatial and time resolutions.
 1291 The track of $high - p_T$ muon candidates is built combining information from the
 1292 tracking system and the signal from up to six RPCs and four DT chambers.

1293 The muon tracks are reconstructed from the hits in the several layers of the muon
 1294 system.

1295 3.3.8 CMS trigger system

1296 Under normal conditions, CMS expects pp collisions every 25 ns, i.e., an interaction
 1297 rate of 40 MHz for which it is not possible to store the recorded data in full. In order
 1298 to handle this high event rate data, an online event selection, known as triggering, is

1299 performed; triggering reduce the event rate to 100 Hz for storage and further offline
 1300 analysis.

1301

1302 The trigger system starts with a reduction of the event rate to 100 kHz in the so-
 1303 called *level 1 trigger (L1)*. L1 is based on dedicated programmable hardware like
 1304 Field Programmable Gate Arrays (FPGAs) and Application Specific Integrated Cir-
 1305 cuits (ASICs), partly located in the detector itself; another portion is located in the
 1306 CMS under-ground cavern. Hit patterns information from the muon chambers and
 1307 the energy deposits in the calorimeter are used to decide if an event is accepted or
 1308 rejected, according to selection requirements previously defined, which reflect the in-
 1309 teresting physics processes. Figure 3.17 shows the L1 trigger architecture.

1310

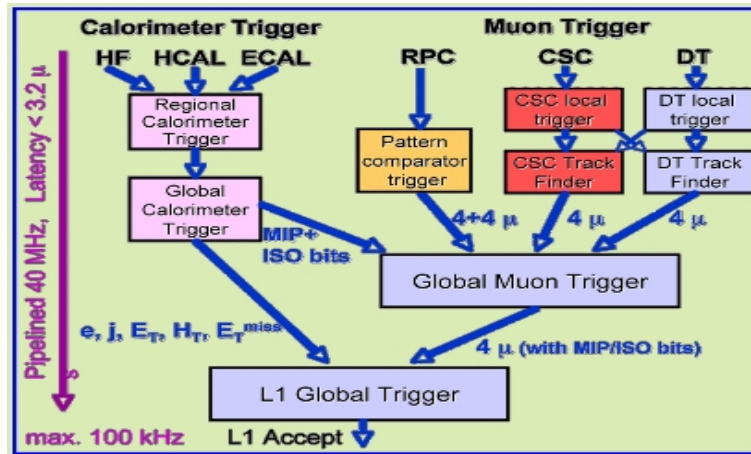


Figure 3.17: CMS Level-1 trigger architecture [82].

1311 The second stage in the trigger system is called *high-level trigger (HLT)*; events ac-
 1312 cepted by L1 are passed to HLT in order to make an initial reconstruction of them.
 1313 HLT is software based and runs on a dedicated server farm, using selection algo-
 1314 rithms and high-level object definitions; the event rate at HLT is reduced to 100 Hz.
 1315 The first HLT stage takes information from the muon detectors and the calorimeters

1316 to make the initial object reconstruction; in the next HLT stage, information from
1317 the pixel and strip detectors is used to do first fast-tracking and then full tracking
1318 online. This initial object reconstruction is used in further steps of the trigger system.

1319

1320 Events and preliminary reconstructed physics objects from HLT are sent to be fully
1321 reconstructed at the CERN computing center. Again, the pixel detector information
1322 provides high-quality seeds for the track reconstruction algorithm offline, primary ver-
1323 tex reconstruction, electron and photon identification, muon reconstruction, τ iden-
1324 tification, and b-tagging. After full reconstruction, data sets are made available for
1325 offline analyses.

1326

1327 During the 2016-2017 technical stop, the L1 system was updated in order to improve
1328 the physics object identification by improving the algorithms and accounting for the
1329 increasing pile-up scenario.

1330 **3.3.9 CMS computing**

1331 After the data, coming from the experiment, are processed at several levels, they have
1332 to be stored and made available for further analysis; in order to cope all the tasks
1333 implied in the offline data processing, like transfer, simulation, reconstruction and
1334 reprocessing, among others, a big computing power is required. The CMS computing
1335 system is based on the distributed architecture concept, where users of the system
1336 and physical computer centers are distributed worldwide and interconnected by high-
1337 speed networks.

1338 The worldwide LHC computing grid (WLCG) is the mechanism used to provide that
1339 distributed environment. WLCG is a tiered structure connecting computing centers

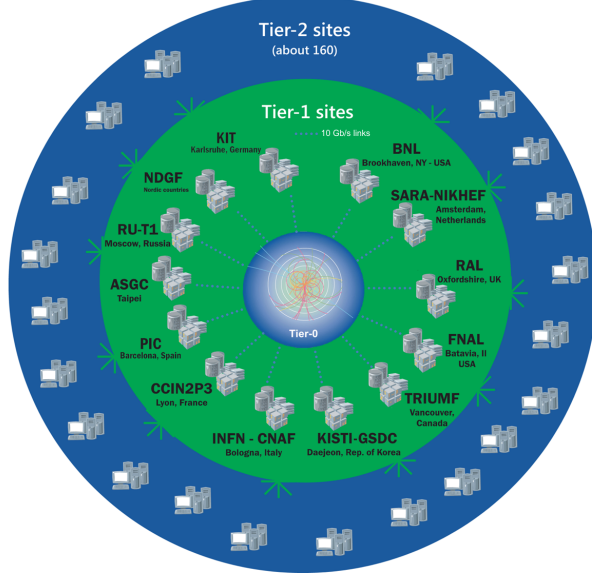


Figure 3.18: WLCG structure. The primary computer centers (Tier-0) are located at CERN (data center) and at the Wigner datacenter in Budapest. Tier-1 is composed of 13 centers and Tier-2 is composed of about 160 centers. [83].

1340 around the world, which provides the necessary storage and computing facilities. The
 1341 primary computing centers of the WLCG are located at the CERN and the Wigner
 1342 datacenter in Budapest and are known as Tier-0 as shown in Figure 3.18. The main
 1343 responsibilities for each tier level are [83]

- 1344 • **Tier-0:** initial reconstruction of recorded events and storage of the resulting
 1345 datasets, the distribution of raw data to the Tier-1 centers.
- 1346 • **Tier-1:** provide storage capacity, support for the Grid, safe-keeping of a pro-
 1347 portional share of raw and reconstructed data, large-scale reprocessing and safe-
 1348 keeping of corresponding output, generation of simulated events, distribution
 1349 of data to Tier 2s, safe-keeping of a share of simulated data produced at these
 1350 Tier 2s.
- 1351 • **Tier-2:** store sufficient data and provide adequate computing power for specific
 1352 analysis tasks, provide analysis requirements and proportional share of simu-

1353 lated event production and reconstruction.

1354 Aside from the general computing strategy to manage the huge amount of data pro-
1355 duced by experiments, CMS uses a framework to perform a variety of processing,
1356 selection and analysis tasks. The central concept of the CMS data model referred to
1357 as *event data model* (EDM) is the *Event*; therefore, an event is the unit that contains
1358 the information from a single bunch crossing as well as any data derived from that
1359 information like the reconstructed objects, the details under which additional data
1360 are derived.

1361

1362 Events are passed as the input to the *physics modules* that obtain information from
1363 them and create new one; for instance, *event data producers* add new data into the
1364 events, *analyzers* produce an information summary from an event set, *filters* perform
1365 selection and triggering.

1366

1367 CMS uses several event formats with different levels of detail and precision

1368 • **Raw format:** events in this format contain the full recorded information from
1369 the detector as well as trigger decision and other metadata. An extended version
1370 of raw data is used to store information from the CMS Monte Carlo simulation
1371 tools. Raw data are stored permanently, occupying about 2MB/event

1372 • **RECO format:** events in this format correspond to raw data that have been
1373 submitted to reconstruction algorithms like primary and secondary vertex re-
1374 construction, particle ID, track-finding. RECO events contain physical objects
1375 and all the information used to reconstruct them; average size is about 0.5
1376 MB/event.

- 1377 • **AOD format:** Analysis Object Data (AOD) is the data format used in the
 1378 physics analyses given that it contains the parameters describing the high-level
 1379 physics objects in addition to enough information to allow a kinematic refitting if
 1380 needed. AOD events are filtered versions of the RECO events to which skimming
 1381 or other kind processes have been applied. Requires about 100 kB/event.
- 1382 • **Non-event data** are data needed to interpret and reconstruct events. Some
 1383 of the non-event data used by CMS contains information about the detector
 1384 contraction and condition data like calibrations, alignment, and detector status.

1385 Figure 3.19 shows the data flow scheme between CMS detector and hardware tiers.

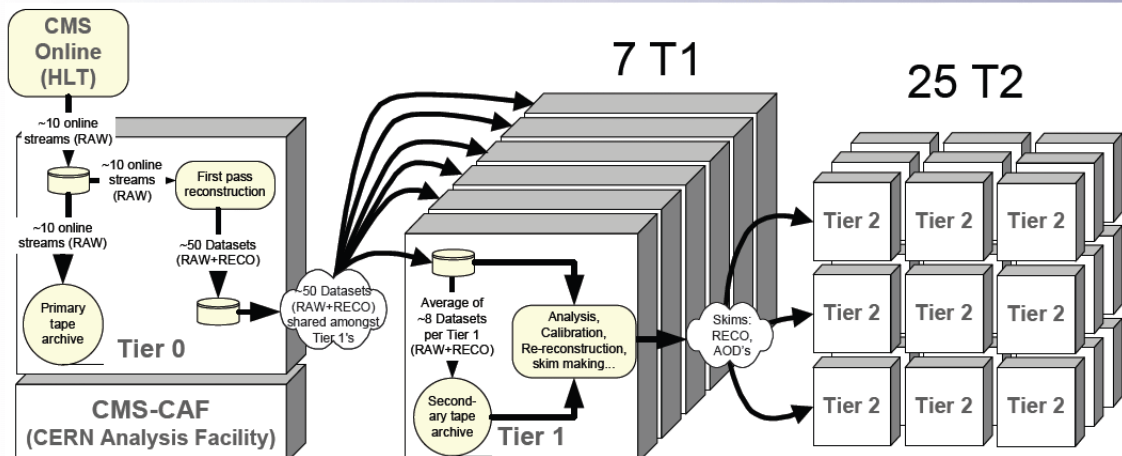


Figure 3.19: Data flow from CMS detector through hardware Tiers.

1386 The whole collection of software built as a framework is referred to as *CMSSW*. This
 1387 framework provides the services needed by the simulation, calibration and alignment,
 1388 and reconstruction modules that process event data, so that physicists can perform
 1389 analysis. The CMSSW event processing model is composed of one executable, called
 1390 cmsRun, and several plug-in modules which contains all the tools (calibration, recon-
 1391 struction algorithms) needed to process an event. The same executable is used for
 1392 both detector and Monte Carlo data [84].

1393 **Chapter 4**

1394 **Event generation, simulation and
1395 reconstruction**

1396 The process of analyzing data recorded by the CMS experiment involves several stages
1397 where the data are processed in order to interpret the information provided by all
1398 the detection systems; in those stages, the particles produced after the pp collision
1399 are identified by reconstructing their trajectories and measuring their features. In
1400 addition, the SM provides a set of predictions that have to be compared with the
1401 experimental results; however, in most of the cases, theoretical predictions are not
1402 directly comparable to experimental results due to the diverse source of uncertainties
1403 introduced by the experimental setup and theoretical approximations, among others.

1404

1405 The strategy to face these conditions consists in using statistical methods imple-
1406 mented in computational algorithms to produce numerical results that can be con-
1407 trasted with the experimental results. These computational algorithms are commonly
1408 known as Monte Carlo (MC) methods and, in the case of particle physics, they are
1409 designed to apply the SM rules and produce predictions about the physical observ-

ables measured in the experiments. Since particle physics is governed by quantum mechanics principles, predictions are not allowed from single events; therefore, a high number of events are *generated* and predictions are produced in the form of statistical distributions for the observables. Effects of the detector presence are included in the predictions by introducing simulations of the detector itself.

1415

1416 This chapter presents a description of the event generation strategy and the tools
 1417 used to perform the detector simulation and physics objects reconstruction. A com-
 1418 prehensive review of event generators for LHC physics can be found in Reference [85]
 1419 on which this chapter is based.

1420 4.1 Event generation

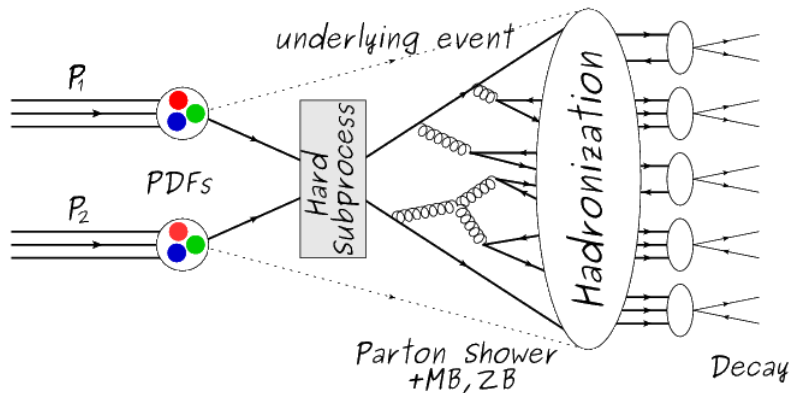


Figure 4.1: Event generation process. The actual interaction is generated in the hard subprocess. The parton shower describes the evolution of the partons from the hard subprocess. Modified from Reference [86].

1421 The event generation is intended to create events that mimic the behavior of actual
 1422 events produced in collisions; they obey a sequence of steps from the particles collision
 1423 hard process to the decay process into the final state. Figure 4.1 shows a schematic
 1424 view of the event generation process; the fact that the full process can be treated as

1425 several independent steps is motivated by the QCD factorization theorem.

1426

1427 Generation starts by taking into account the PDFs of the incoming particles. Event
 1428 generators offer the option to chose from several PDF sets depending on the particu-
 1429 lar process under simulation¹; in the following, pp collisions will be considered. The
 1430 *hard subprocess* describes the actual interaction between partons from the incoming
 1431 protons; it is represented by the matrix element connecting the initial and final states
 1432 of the interaction. Normally, the matrix element can be written as a sum over Feyn-
 1433 man diagrams and consider interferences between terms in the summation. During
 1434 the generation of the hard subprocess, the production cross section is calculated.

1435

1436 The order to which the cross section is calculated depends on the order of the Feyn-
 1437 man diagrams involved in the calculation; therefore, radiative corrections are included
 1438 by considering a higher order Feynman diagrams where QCD radiation dominates.
 1439 Currently, cross sections calculated to LO do not offer a satisfactory description of the
 1440 processes, i.e., the results are only reliable for the shape of distributions; therefore,
 1441 NLO calculations have to be performed with the implication that the computing time
 1442 needed is highly increased.

1443

1444 The final parton content of the hard subprocess is subjected to the *parton shower*
 1445 which generates the gluon radiation. Parton shower evolves the partons, i.e., glouns
 1446 split into quark-antiquark pairs and quarks with enough energy radiate gluons giv-
 1447 ing rise to further parton multiplication, following the DGLAP (Dokshitzer-Gribov-
 1448 Lipatov-Altarelli-Parisi) equations. Showering continues until the energy scale is low
 1449 enough to reach the non-perturbative limit.

¹ Tool in Reference [87] allows to plot different PDF sets under customizable conditions.

1450

1451 In the simulation of LHC processes that involve b quarks, like the single top quark
 1452 or Higgs associated production, it is needed to consider that the b quark is heavier
 1453 than the proton; hence, the QCD interaction description is made in two different
 1454 schemes [88]

1455 • four-flavor (4F) scheme. b quarks appear only in the final state because they
 1456 are heavier than the proton and therefore they can be produced only from the
 1457 splitting of a gluon into pairs or singly in association with a t quark in high
 1458 energy-scale interactions; furthermore, during the simulation, the b -PDFs are set
 1459 to zero. Calculations in this scheme are more complicated due to the presence
 1460 of the second b quark but the full kinematics is considered already at LO and
 1461 therefore the accuracy of the description is better.

1462 • five-flavor (5F) scheme. b quarks are considered massless, therefore they can
 1463 appear in both initial and final states since they can now be part of the proton;
 1464 thus, during the simulation b -PDFs are not set to zero. In this scheme, calcu-
 1465 lations are simpler than in the 4F scheme and possible logarithmic divergences
 1466 are absorbed by the PDFs through the DGLAP evolution.

1467 In this thesis, the tHq events are generated using the 4F scheme in order to reduce
 1468 uncertainties, while the tHW events are generated using the 5F scheme to eliminate
 1469 LO interference with $t\bar{t}H$ process [53].

1470

1471 Partons involved in the pp collision are the focus of the simulation, however, the rest
 1472 of the partons inside the incoming protons are also affected because the remnants are
 1473 colored objects; also, multiple parton interactions can occur. The hadronization of
 1474 the remnants and multiple parton interactions are known as *underlying event* and it

1475 has to be included in the simulation. In addition, multiple pp collisions in the same
 1476 bunch crossing (pile-up mentioned in 3.2) occurs, actually in two forms

1477 • *in-time PU* which refers to multiple pp collision in the bunch crossing but that
 1478 are not considered as primary vertices.

1479 • *Out-of-time PU* which refers to overlapping pp collisions from consecutive bunch
 1480 crossings; this can occur due to the time-delays in the detection systems where
 1481 information from one bunch crossing is assigned to the next or previous one.

1482 While the underlying event effects are included in generation using generator-specific
 1483 tools, PU effects are added to the generation by overlaying Minimum-bias (MB) and
 1484 Zero-bias (ZB) events to the generated events. MB events are inelastic events se-
 1485 lected by using a loose trigger with as little bias as possible, therefore accepting a
 1486 large fraction of the overall inelastic event; ZB events correspond to random events
 1487 recorded by the detector when collisions are likely. MB models in-time PU and ZB
 1488 models out-of-time PU.

1489

1490 The next step in the generation process is called *hadronization*. Since particles with
 1491 a net color charge are not allowed to exits isolated, they have to recombine to form
 1492 bound states. This is precisely the process by which the partons resulting from the
 1493 parton shower arrange themselves as color singlets to form hadrons. At this step, the
 1494 energy-scale is low and the strong coupling constant is large, therefore hadronization
 1495 process is non-perturbative and the evolution of the partons is described using phe-
 1496 nomenological models. Most of the baryons and mesons produced in the hadronization
 1497 are unstable and hence they will decay in the detector.

1498

1499 The last step in the generation process corresponds to the decay of the unstable
 1500 particles generated during hadronization; it is also simulated in the hadronization
 1501 step, based on the known branching ratios.

1502 **4.2 Monte Carlo Event Generators.**

1503 The event generation described in the previous section has been implemented in
 1504 several software packages for which a brief description is given.

1505 • **PYTHIA 8.** It is a program designed to perform the generation of high energy
 1506 physics events which describes the collisions between particles such as electrons
 1507 and protons. Several theories and models are implemented in it, in order to
 1508 describe physical aspects like hard and soft interaction, parton distributions,
 1509 initial and final-state parton showers, multiple parton interactions, beam rem-
 1510 nants, hadronization² and particle decay. Thanks to extensive testing, several
 1511 optimized parametrizations, known as *tunings*, have been defined in order to
 1512 improve the description of actual collisions to a high degree of precision; for
 1513 analysis at $\sqrt{s} = 13$ TeV, the underline event CUETP8M1 tune is employed [90].
 1514 The calculation of the matrix element is performed at LO which is not enough
 1515 for the current required level of precision; therefore, pythia is often used for
 1516 parton shower, hadronization and decays, while other event generators are used
 1517 to generate the matrix element at NLO.

1518 • **MadGraph5_aMC@NLO.** MadGraph is a matrix element generator which
 1519 calculates the amplitudes for all contributing Feynman diagrams of a given pro-
 1520 cess but does not provide a parton shower while MC@NLO incorporates NLO

² based in the Lund string model [89]

1521 QCD matrix elements consistently into a parton shower framework; thus, Mad-
 1522 Graph5_aMC@NLO, as a merger of the two event generators MadGraph5 and
 1523 aMC@NLO, is an event generator capable to calculate tree-level and NLO cross
 1524 sections and perform the matching of those with the parton shower. It is one of
 1525 the most frequently used matrix element generators; however, it has the partic-
 1526 ular feature of the presence of negative event weights which reduce the number
 1527 of events used to reproduce the properties of the objects generated [91].

1528

1529 • **POWHEG.** It is an NLO matrix element generator where the hardest emis-
 1530 sion of color charged particles is generated in such a way that the negative event
 1531 weights issue of MadGraph5_aMC@NLO is overcome; however, the method re-
 1532 quires an interface with p_T -ordered parton shower or a parton shower generator
 1533 where this highest emission can be vetoed in order to avoid double counting of
 1534 this highest-energetic emission. PYTHIA is a commonly matched to POWHEG
 1535 event generator [92].

1536 Events resulting from the whole generation process are known as MC events.

1537 4.3 CMS detector simulation.

1538 After generation, MC events contain the physics of the collisions but they are not
 1539 ready to be compared to the events recorded by the experiment since these recorded
 1540 events correspond to the response of the detection systems to the interaction with
 1541 the particles traversing them. The simulation of the CMS detector has to be applied
 1542 on top of the event generation; it is simulated with a MC toolkit for the simulation
 1543 of particles passing through matter called Geant4 which is also able to simulate the

1544 electronic signals that would be measured by all detectors inside CMS.

1545

1546 The simulation takes the generated particles contained in the MC events as input,
1547 makes them pass through the simulated geometry, and models physics processes that
1548 particles experience during their passage through matter. The full set of results from
1549 particle-matter interactions corresponds to the simulated hit which contains informa-
1550 tion about the energy loss, momentum and position. Particles of the input event are
1551 called *primary*, while the particles originating from GEANT4-modeled interactions of
1552 a primary particle with matter are called a *secondary*. Simulated hits are the input
1553 of subsequent modules that emulate the response of the detector readout system and
1554 triggers. The output from the emulated detection systems and triggers is known as
1555 digitization [93, 94].

1556

1557 The modeling of the CMS detector corresponds to the accurate modeling of the
1558 interaction among particles, the detector material, and the magnetic field. This
1559 simulation procedure includes the following standard steps

1560 • Modeling of the Interaction Region.

1561 • Modeling of the particle passage through the hierarchy of volumes that compose
1562 CMS detector and of the accompanying physics processes.

1563 • Modeling of the effect of multiple interactions per beam crossing and/or the
1564 effect of events overlay (Pile-Up simulation).

1565 • Modeling of the detector's electronics response, signal shape, noise, calibration
1566 constants (digitization).

1567 In addition to the full simulation, i.e., a detailed detector simulation, a faster simu-
 1568 lation (FastSim) have been developed, that may be used where much larger statistics
 1569 are required. In FastSim, detector material effects are parametrized and included in
 1570 the hits; those hits are used as input of the same higher-level algorithms³ used to an-
 1571 alyze the recorded events. In this way, comparisons between fast and full simulations
 1572 can be performed [96].

1573

1574 After the full detector simulation, the output events can be directly compared to
 1575 events actually recorded in the CMS detector. The collection of MC events that
 1576 reproduces the expected physics for a given process is known as MC sample.

1577 **4.4 Event reconstruction.**

1578 The CMS experiment use the *particle-flow event reconstruction algorithm (PF)* to do
 1579 the reconstruction of particles produced in pp collisions. Next sections will present
 1580 a basic description of the *Elements* used by PF (tracker tracks, energy clusters, and
 1581 muon tracks), based in the References [97, 98] where more detailed descriptions can
 1582 be found.

1583 **4.4.1 Particle-Flow Algorithm.**

1584 Each of the several sub detection systems of the CMS detector is dedicated to identify
 1585 a specific type of particles, i.e., photons and electrons are absorbed by the ECAL
 1586 and their reconstruction is based on ECAL information; hadrons are reconstructed
 1587 from clusters in the HCAL while muons are reconstructed from hits in the muon

³ track fitting, calorimeter clustering, b tagging, electron identification, jet reconstruction and calibration, trigger algorithms which will be considered in the next sections

1588 chambers. PF is designed to correlate signals from all the detector layers (tracks and
 1589 energy clusters) in order to reconstruct and identify each final state particle and its
 1590 properties as sketched in Figure 4.2.

1591

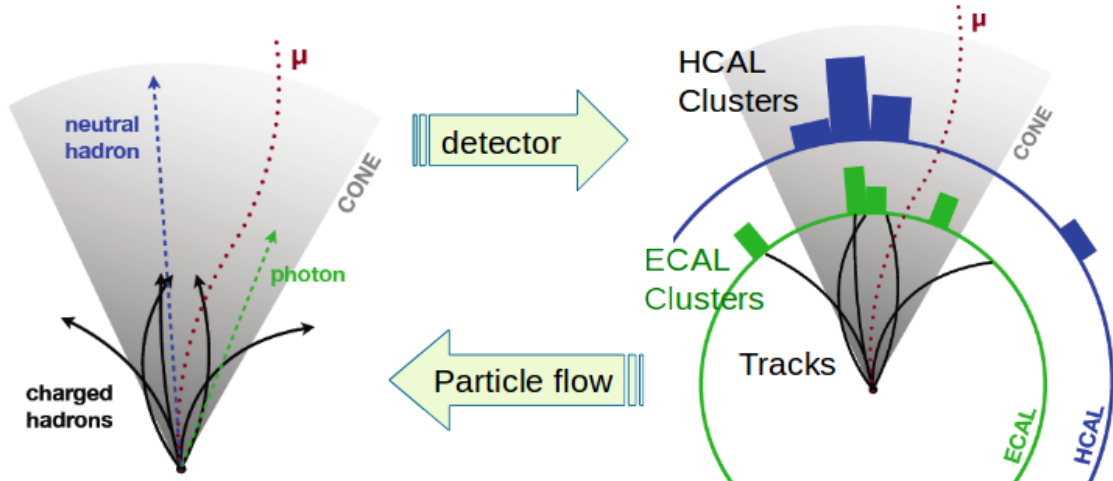


Figure 4.2: Particle flow algorithm. Information from the several CMS detection systems is provided as input to the algorithm which then combine it to identify and reconstruct all the particles in the final state and their properties. Reconstruction of simulated events is also performed by providing information from MC samples, detector and trigger simulation [99].

1592 For instance, a charged hadron is identified by a geometrical connection, known as
 1593 *link*, between one or more calorimeter clusters and a track in the tracker, provided
 1594 there are no hits in the muon system; combining several measurements allows a better
 1595 determination of the energy and charge sign of the charged hadron.

1596 Charged-particle track reconstruction.

1597 The strategy used by PF in order to reconstruct tracks is called *Iterative Tracking*
 1598 which occurs in four steps

- 1599 • Seed generation where initial track candidates are found by looking for a combi-
 1600 nation of hits in the pixel detector, strip tracker, and muon chambers. In total

1601 ten iterations are performed, each one with a different seeding requirement.
 1602 Seeds are used to estimate the trajectory parameters and uncertainties at the
 1603 time of the full track reconstruction. Seeds are also considered track candidates.

- 1604 • Track finding using a tracking software known as Combinatorial Track Finder
 1605 (CTF) [100]. The seed trajectories are extrapolated along the expected flight
 1606 path of a charged particle, in agreement to the trajectory parameters obtained
 1607 in the first step, in an attempt to find additional hits that can be assigned to
 1608 the track candidates.
- 1609 • Track-fitting where the found tracks are passed as input to a module which
 1610 provides the best estimate of the parameters of each trajectory.
- 1611 • Track selection where track candidates are submitted to a selection which dis-
 1612 cards those that fail a set of defined quality criteria.

1613 Iterations differ in the seeding configuration and the final track selection as elaborated
 1614 in References [97, 98]. In the first iteration, high p_T tracks and tracks produced near
 1615 to the interaction region are identified and those hits are masked thereby reducing
 1616 the combinatorial complexity. Next, iterations search for more complicated tracks,
 1617 like low p_T tracks and tracks from b hadron decays, which tend to be displaced from
 1618 the interaction region.

1619 **Vertex reconstruction.**

1620 During the track reconstruction, an extrapolation toward to the calorimeters is per-
 1621 formed in order to match energy deposits; that extrapolation is performed also toward
 1622 the beamline in order to find the origin of the track known as *vertex*. The vertex re-
 1623 construction is performed by selecting from the available reconstructed tracks, those

1624 that are consistent with being originated in the interaction region where pp collisions
 1625 are produced. The selection involves a requirement on the number of tracker (pixel
 1626 and strip) hits and the goodness of the track fit.

1627

1628 Selected tracks are clustered using a *deterministic annealing algorithm* (DA)⁴. A set
 1629 of candidate vertices and their associated tracks, resulting from the DA, are then fit-
 1630 ted with an *adaptive vertex fitter* (AVF) to produce the best estimate of the vertices
 1631 locations.

1632

1633 The p_T of the tracks associated to a reconstructed vertex is added, squared and used
 1634 to organize the vertices; the vertex with the highest squared sum is designated as the
 1635 *primary vertex* (PV) while the rest are designated as PU vertices.

1636 Calorimeter clustering.

1637 After traversing the CMS tracker system, electrons, photons and hadrons deposit their
 1638 energy in the ECAL and HCAL cells. The PF clustering algorithm aims to provide
 1639 a high detection efficiency even for low-energy particles and an efficient distinction
 1640 between close energy deposits. The clustering runs independently in the ECAL barrel
 1641 and endcaps, HCAL barrel and endcaps, and the two preshower layers, following two
 1642 steps

- 1643 • cells with an energy larger than a given seed threshold and larger than the energy
 1644 of the neighboring cells are identified as cluster seeds. The neighbor cells are
 1645 those that either share a side with the cluster seed candidate, or the eight closest
 1646 cells including cells that only share a corner with the seed candidate.

⁴ DA algorithm and AVF are described in detail in References [102, 103]

1647 • cells with at least a corner in common with a cell already in the cluster seed
 1648 and with an energy above a cell threshold are grouped into topological clusters.

1649 Clusters formed in this way are known as *particle-flow clusters*. With this clustering
 1650 strategy, it is possible to detect and measure the energy and direction of photons and
 1651 neutral hadrons as well as differentiate these neutral particles from the charged hadron
 1652 energy deposits. In cases involving charged hadrons for which the track parameters
 1653 are not determined accurately, for instance, low-quality and high- p_T tracks, clustering
 1654 helps in the energy measurements.

1655 **Electron track reconstruction.**

1656 Although the charged-particle track reconstruction described above works for elec-
 1657 trons, they lose a significant fraction of their energy via bremsstrahlung photon radi-
 1658 ation before reaching the ECAL; thus, the reconstruction performance depends on the
 1659 ability to measure also the radiated energy. The reconstruction strategy, in this case,
 1660 requires information from the tracking system and from the ECAL. Bremsstrahlung
 1661 photons are emitted at similar η values to that of the electron but at different values
 1662 of ϕ ; therefore, the radiated energy can be recovered by grouping ECAL clusters in a
 1663 η window over a range of ϕ around the electron direction. The group is called ECAL
 1664 supercluster.

1665

1666 Electron candidates from the track-seeding and ECAL super clustering are merged
 1667 into a single collection which is submitted to a full electron tracking fit with a
 1668 Gaussian-sum filter (GSF) [101]. The electron track and its associated ECAL su-
 1669 percluster form a *particle-flow electron*.

1670 **Muon track reconstruction.**

1671 Given that the CMS detector is equipped with a muon spectrometer capable to iden-
 1672 tify and measure the momentum of the muons traversing it, the muon reconstruction
 1673 is not specific to PF; therefore, three different muon types are defined

- 1674 • *Standalone muon.* A clustering on the DTs or CSCs hits is performed to form
 1675 track segments; those segments are used as seeds for the reconstruction in the
 1676 muon spectrometer. All DTs, CSCs, and RPCs hits along the muon trajectory
 1677 are combined and fitted to form the full track. The fitting output is called a
 1678 *standalone-muon track*.
- 1679 • *Tracker muon.* Each track in the inner tracker with p_T larger than 0.5 GeV and
 1680 a total momentum p larger than 2.5 GeV is extrapolated to the muon system.
 1681 A *tracker muon track* corresponds to a extrapolated track that matches at least
 1682 one muon segment.
- 1683 • *Global muon.* When tracks in the inner tracker (inner tracks) and standalone-
 1684 muon tracks are matched and turn out being compatibles, their hits are com-
 1685 bined and fitted to form a *global-muon track*.

1686 Global muons sharing the same inner track with tracker muons are merged into a
 1687 single candidate. PF muon identification uses the muon energy deposits in ECAL,
 1688 HCAL, and HO associated with the muon track to improve the muon identification.

1689 **Particle identification and reconstruction.**

1690 PF elements are connected by a linker algorithm that tests the connection between any
 1691 pair of elements; if they are found to be linked, a geometrical distance that quantifies
 1692 the quality of the link is assigned. Two elements may be linked indirectly through

1693 common elements. Linked elements form *PF blocks* and each PF block may contain
 1694 elements originating in one or more particles. Links can be established between
 1695 tracks, between calorimeter clusters, and between tracks and calorimeter clusters.
 1696 The identification and reconstruction start with a PF block and proceed as follows

1697 • Muons. An *isolated global muon* is identified by evaluating the presence of
 1698 inner track and energy deposits close to the global muon track in the (η, ϕ)
 1699 plane, i.e., in a particular point of the global muon track, inner tracks and
 1700 energy deposits are sought within a radius of $\Delta R = 0.3$ (see eqn. 3.7) from the
 1701 muon track; if they exit and the p_T of the found track added to the E_T of the
 1702 found energy deposit does not exceed 10% of the muon p_T then the global muon
 1703 is an isolated global muon. This isolation condition is stringent enough to reject
 1704 hadrons misidentified as muons.

1705 *Non-isolated global muons* are identified using additional selection requirements
 1706 on the number of track segments in the muon system and energy deposits along
 1707 the muon track. Muons inside jets are identified with more stringent criteria
 1708 in isolation and momentum as described in Reference [104]. The PF elements
 1709 associated with an identified muon are masked from the PF block.

1710 • Electrons are identified and reconstructed as described above plus some addi-
 1711 tional requirements on fourteen variables like the amount of energy radiated,
 1712 the distance between the extrapolated track position at the ECAL and the po-
 1713 sition of the associated ECAL supercluster, among others, which are combined
 1714 in an specialized multivariate analysis strategy that improves the electron iden-
 1715 tification. Tracks and clusters used to identify and reconstruct electrons are
 1716 masked in the PF block.

- 1717 • Isolated photons are identified from ECAL superclusters with E_T larger than 10
 1718 GeV, for which the energy deposited at a distance of 0.15, from the supercluster
 1719 position on the (η, ϕ) plane, does not exceed 10% of the supercluster energy;
 1720 note that this is an isolation requirement. In addition, there must not be links
 1721 to tracks. Clusters involved in the identification and reconstruction are masked
 1722 in the PF block.
- 1723 • Bremsstrahlung photons and prompt photons tend to convert to electron-positron
 1724 pairs inside the tracker, therefore, a dedicated finder algorithm is used to link
 1725 tracks that seem to originate from a photon conversion; in case those two tracks
 1726 are compatible with the direction of a bremsstrahlung photon, they are also
 1727 linked to the original electron track. Photon conversion tracks are also masked
 1728 in the PF block.
- 1729 • The remaining elements in the PF block are used to identify hadrons. In the
 1730 region $|\eta| \leq 2.5$, neutral hadrons are identified with HCAL clusters not linked
 1731 to any track while photons from neutral pion decays are identified with ECAL
 1732 clusters without links to tracks. In the region $|\eta| > 2.5$ ECAL clusters linked to
 1733 HCAL clusters are identified with a charged or neutral hadron shower; ECAL
 1734 clusters with no links are identified with photons. HCAL clusters not used yet,
 1735 are linked to one or more unlinked tracks and to an unlinked ECAL in order to
 1736 reconstruct charged-hadrons or a combination of photons and neutral hadrons
 1737 according to certain conditions on the calibrated calorimetric energy.
- 1738 • Charged-particle tracks may be liked together when they converge to a *sec-
 1739 ondary vertex (SV)* displaced from the interaction point where the PV and PU
 1740 vertices are reconstructed; at least three tracks are needed in that case, of which
 1741 at most one has to be an incoming track with hits in tracker region between a

1742 PV and the SV.

1743

1744 The linker algorithm, as well as the whole PF algorithm, has been validated and
 1745 commissioned; results from that validation are presented in the Reference [97].

1746 **Jet reconstruction.**

1747 Quarks and gluons may be produced in the pp collisions, therefore, their hadronization
 1748 will be seen in the detector as a shower of hadrons and their decay products in the
 1749 form of a *jet*. The anti- k_t algorithm [105] is used to perform the jet reconstruction
 1750 by clustering those PF particles within a cone (see Figure 4.3); previously, isolated
 1751 electrons, isolated muons, and charged particles associated with other interaction
 1752 vertices are excluded from the clustering.

1753 The anti- k_t algorithm proceeds in a sequential recombination of PF particles; the
 1754 distance between particles i and j (d_{ij}) and the distance between particles and the
 1755 beam are defined as

$$d_{ij} = \min\left(\frac{1}{k_{ti}^2}, \frac{1}{k_{tj}^2}\right) \frac{\Delta_{ij}^2}{R^2}$$

$$d_{iB} = \frac{1}{k_{ti}^2} \quad (4.1)$$

1756 where $\Delta_{ij}^2 = (y_i - y_j)^2 + (\phi_i - \phi_j)^2$, k_{ti}, y_i and ϕ_i are the transverse momentum, ra-
 1757 pidity and azimuth of particle i respectively and R is the called jet radius. For all
 1758 the remaining PF particles, after removing the isolated ones, d_{ij} and d_{iB} are calcu-
 1759 lated⁵ and the smallest is identified; if it is a d_{ij} , particles i and j are replaced with

⁵ Notice that this is a combinatorial calculation.

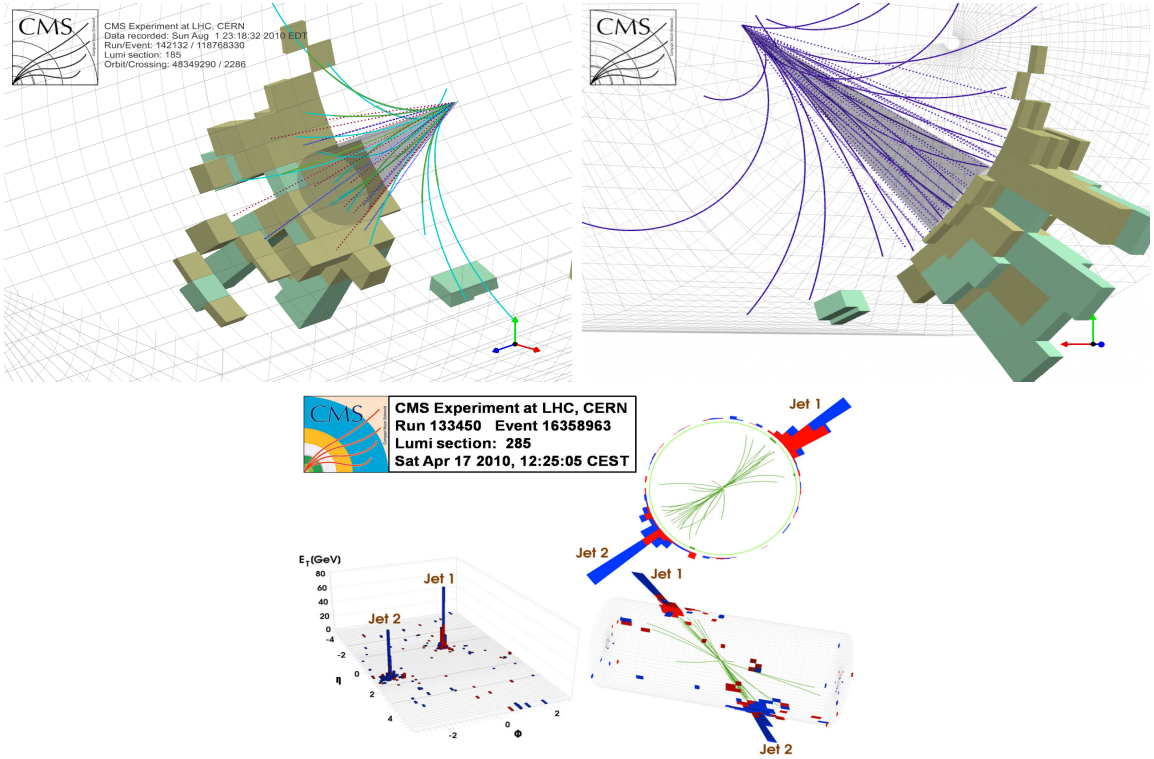


Figure 4.3: Jet reconstruction performed by the anti- k_t algorithm. Top: Two different views of a CMS recorded event are presented. Continuous lines correspond to tracks left by charged particles in the tracker while dotted lines are the imaginary paths followed by neutral particles. The green cubes represent the ECAL cells while the blue ones represent the HCAL cells; in both cases, the height of the cube represent the amount of energy deposited in the cells [106]. Bottom: Reconstruction of a recorded event with two jets [107].

1760 a new object whose momentum is the vectorial sum of the combined particles. If the
 1761 smallest distance is a d_{iB} the clustering process ends, the object i (which at this stage
 1762 should be a combination of several PF particles) is declared as a *Particle-flow-jet* (PF
 1763 jet) and all the associated PF particles are removed from the detector. The clustering
 1764 process is repeated until no PF particles remain.
 1765 Even though jets can be reconstructed efficiently, there are some effects that are not in-
 1766 cluded in the reconstruction and that lead to discrepancies between the reconstructed
 1767 results and the predicted results; in order to overcome these discrepancies, a factor-
 1768 ized model has been designed in the form of jet energy corrections (JEC) [108, 109]

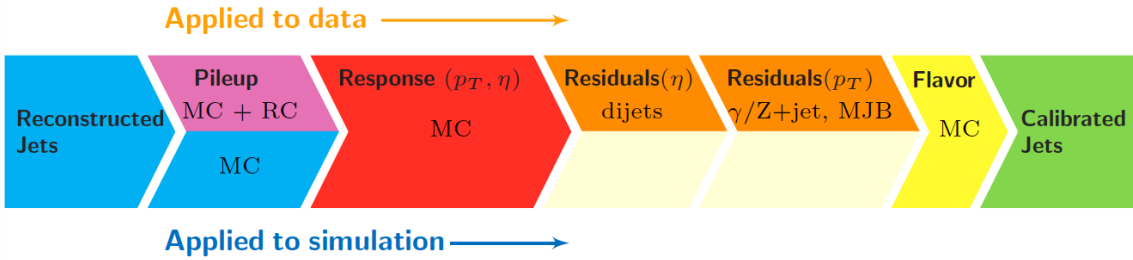


Figure 4.4: Jet energy correction diagram. Correction levels are applied sequentially in the indicated fixed order [109].

1769 applied sequentially as shown in the diagram of Figure 4.4.

1770 At each level, the jet four-momentum is multiplied by a scaling factor based on jet
1771 properties, i.e., η , flavor, etc.

- Level 1 correction removes the energy coming from pile-up. The scale factor is determined using a MC sample of QCD dijet (2 jets) events with and without pileup overlay; it is parametrized in terms of the offset energy density ρ , jet area A, jet η and jet p_T . Different corrections are applied to data and MC due to the detector simulation.
 - MC-truth correction accounts for differences between the reconstructed jet energy and the MC particle-level energy. The correction is determined on a QCD dijet MC sample and is parametrized in terms of the jet p_T and η .
 - Residuals correct remaining small differences within jet response in data and MC. The Residuals η -dependent correction compares jets of similar p_T in the barrel reference region. The Residuals p_T -dependent correct the jet absolute scale (JES vs p_T).
 - Jet-flavor corrections are derived in the same way as MC-truth corrections but using QCD pure flavor samples.

1786 ***b*-tagging of jets.**

1787 A particular feature of the hadrons containing bottom quarks (*b*-hadrons) is that
 1788 their lifetime is long enough to travel some distance before decaying, but it is not as
 1789 long as those of light quark hadrons; therefore, when looking at the hadrons produced
 1790 in pp collisions, *b*-hadrons decay typically inside the tracker rather than reaching the
 1791 calorimeters as some light-hadrons do. As a result, a *b*-hadron decay gives rise to a
 1792 displaced vertex (secondary vertex) with respect to the primary vertex as shown in
 1793 Figure 4.5; the SV displacement is in the order of a few millimeters. A jet resulting
 1794 from the decay of a *b*-hadron is called *b* jet; other jets are called light jets.

1795

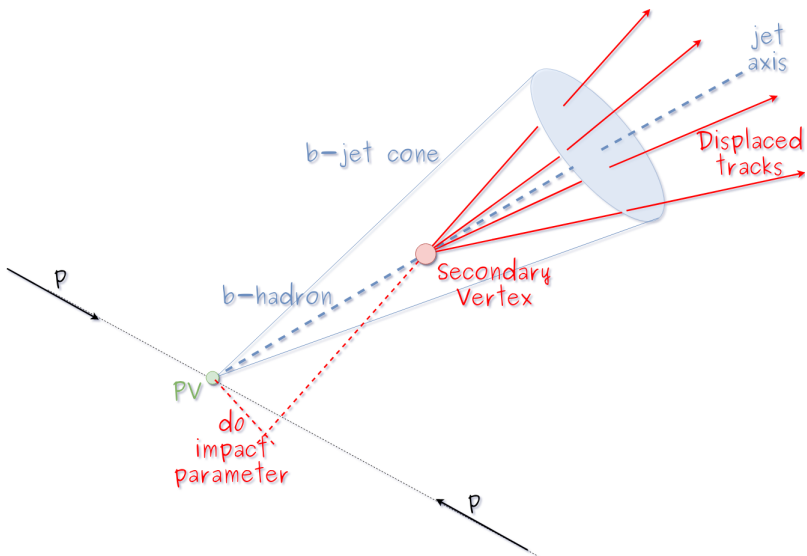


Figure 4.5: Secondary vertex in a *b*-hadron decay.

1796 Several methods to identify *b*-jets (*b*-tagging) have been developed; the method used
 1797 in this thesis is known as *Combined Secondary Vertex* algorithm in its second version
 1798 (CSVv2) [110]. By using information of the impact parameter, the reconstructed
 1799 secondary vertices, and the jet kinematics as input in a multivariate analysis that
 1800 combines the discrimination power of each variable in one global discriminator vari-

able, three working points (references): loose, medium and tight, are defined which quantify the probabilities of mistag jets from light quarks as jets from b quarks; 10, 1 and 0.1 % respectively. Although the mistagging probability decreases with the working point strength, the efficiency to correctly tag b -jets also decreases as 83, 69 and 49 % for the respective working point; therefore, a balance needs to be achieved according to the specific requirements of the analysis.

4.4.1.1 Missing transverse energy.

The fact that proton bunches carry momentum along the z -axis implies that for each event it is expected that the momentum in the transverse plane is balanced. Imbalances are quantified by the missing transverse energy (MET) and are attributed to several sources including particles escaping undetected through the beam pipe, neutrinos produced in weak interactions processes which do not interact with the detector and thus escaping without leaving a sign, or even undiscovered particles predicted by models beyond the SM.

1815

1816 The PF algorithm assigns the negative sum of the momenta of all reconstructed PF
1817 particles to the *particle-flow MET* according to

$$\vec{E}_T = - \sum_i \vec{p}_{T,i} \quad (4.2)$$

1818 JEC are propagated to the calculation of the \vec{E}_T as described in the Reference [111].

1819

1820 **4.4.2 Event reconstruction examples**

1821 Figures 4.6-4.8 show the results of the reconstruction performed on 3 recorded events.

1822 Descriptions are taken directly from the source.

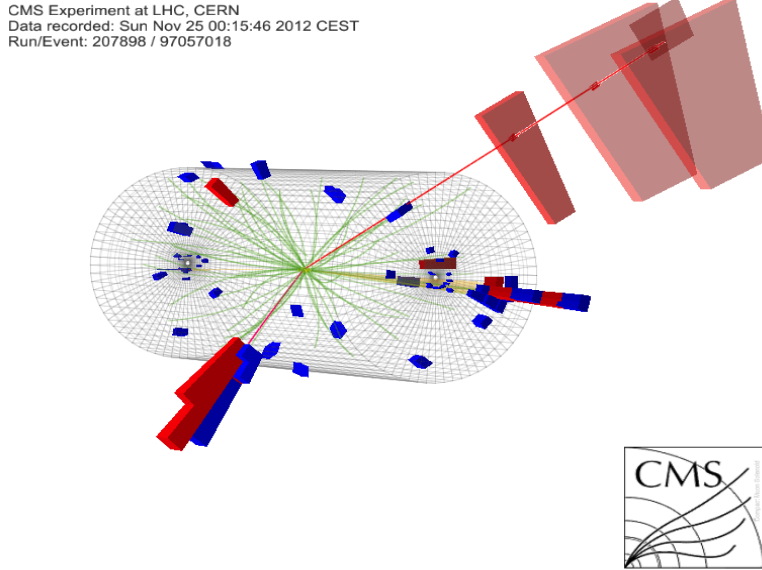


Figure 4.6: HIG-13-004 Event 1 reconstruction results; “HIG-13-004 Event 1: Event recorded with the CMS detector in 2012 at a proton-proton center-of-mass energy of 8 TeV. The event shows characteristics expected from the decay of the SM Higgs boson to a pair of τ leptons. Such an event is characterized by the production of two forward-going jets, seen here in opposite endcaps. One of the τ decays to a muon (red lines on the right) and neutrinos, while the other τ decays into a charged hadron and a neutrino.” [112].

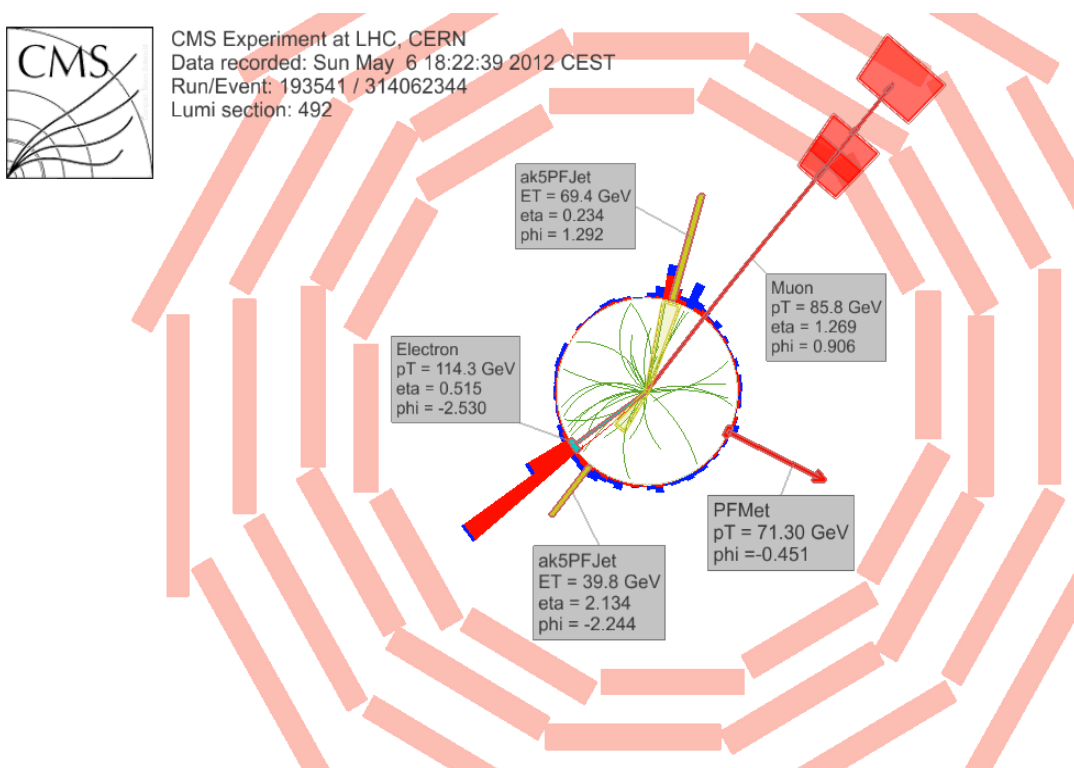


Figure 4.7: $e\mu$ event reconstruction results; “An $e\mu$ event candidate selected in 8 TeV data, as seen from the direction of the proton beams. The kinematics of the main objects used in the event selection are highlighted: two isolated leptons and two particle-flow jets. The reconstructed missing transverse energy is also displayed for reference” [113].

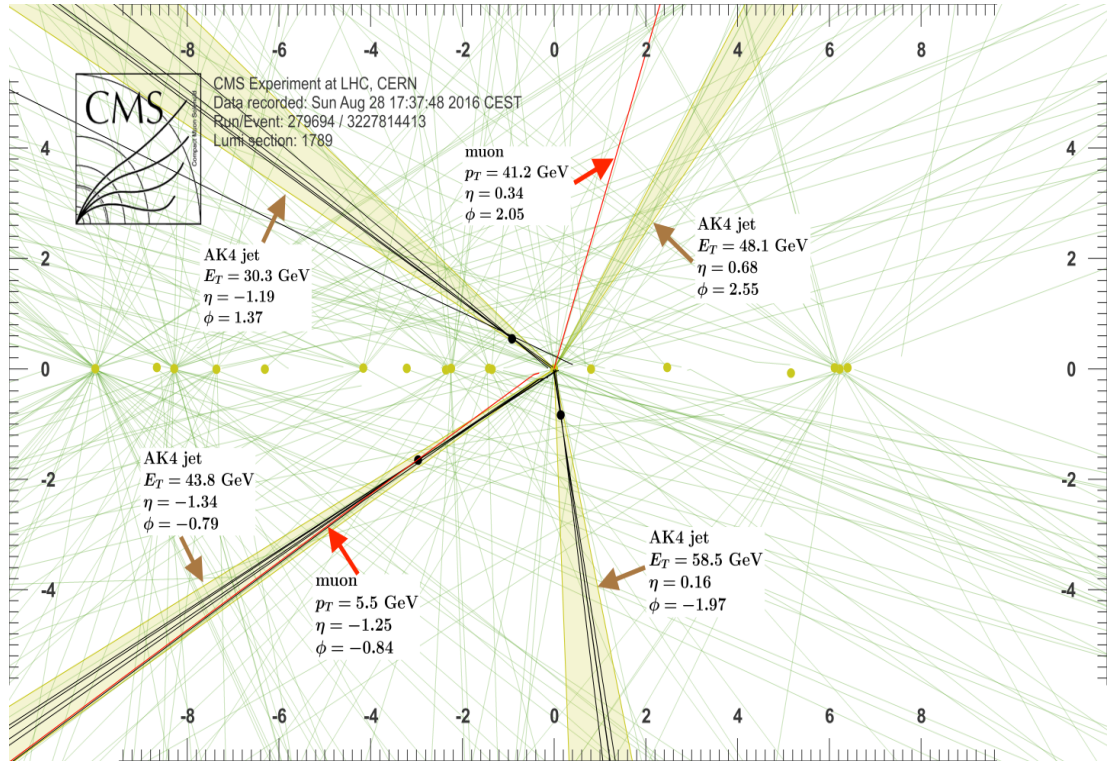


Figure 4.8: Recorded event reconstruction results;“Recorded event (ρ - z projection) with three jets with $p_T > 30$ GeV with one displaced muon track in 2016 data collected at 13 TeV. Each of the three jets has a displaced reconstructed vertex. The jet with $p_T(j) = 43.8$ GeV, $\eta(j) = -1.34$, $\phi(j) = -0.79$ contains muon with $p_T(\mu) = 5.5$ GeV, $\eta(\mu) = -1.25$, $\phi(\mu) = -0.84$. Event contains reconstructed isolated muon with $p_T(\mu) = 41.2$ GeV, $\eta(\mu) = 0.34$, $\phi(\mu) = 2.05$ and MET with $p_T = 72.5$ GeV, $\phi = -0.32$. Jet candidates for a b -jet from top quark leptonic and hadronic decays are tagged by CSVv2T algorithm. One of the other two jets is tagged by CharmT algorithm. Tracks with $p_T > 0.5$ GeV are shown. The number of reconstructed primary vertices is 18. Reconstructed $m_T(W)$ is 101.8 GeV. Beam spot position correction is applied. Reconstructed primary vertices are shown in yellow color, while reconstructed displaced vertices and associated tracks are presented in black color. Dimensions are given in cm” [114].

1823 **Chapter 5**

1824 **Statistical methods**

1825 In the course of analyzing the data sets provided by the CMS experiment and used in
1826 this thesis, several statistical tools have been employed; in this chapter, a description
1827 of these tools will be presented, starting with the general statement of the multivariate
1828 analysis method, followed by the particularities of the Boosted Decision Trees (BDT)
1829 method and its application to the classification problem. Statistical inference methods
1830 used will also be presented. This chapter is based mainly on the references [115–117].

1831 **5.1 Multivariate analysis**

1832 Multivariate data analysis (MVA) makes reference to statistical techniques that an-
1833 alyze data containing information of more than one variable, commonly taking into
1834 account the effects of all variables on the response of the particular variable under
1835 investigation, i.e., considering all the correlations between variables. MVA is em-
1836 ployed in a variety of fields like consumer and market research, quality control and
1837 process optimization. From a MVA it is possible to identify the dominant patterns
1838 in the data, like groups, outliers and trends, and determine to which group a set of

1839 values belong; in the particle physics context, MVA methods are used to perform the
 1840 selection of certain type of events, from a large data set, using a potentially large
 1841 number of measurable properties for each event.

1842 Processes with small cross section, as the tHq process, normally are hidden behind
 1843 more common processes; therefore, the data set results in a subset of events with
 1844 characteristic features of interest (signal) mixed in randomly with a much larger
 1845 number of SM events that can mimic these features of interest (background) which
 1846 implies that it is not possible to say with certainty that a given event is signal or
 1847 background. In that sense, the problem can be formulated as one where a set of
 1848 events have to be classified according to some features; these features correspond to
 1849 the measurements of several parameters like energy or momentum, organized in a
 1850 set of *input variables*. The measurements for each event can be written in a vector
 1851 $\mathbf{x} = (x_1, \dots, x_n)$ for which

- 1852 • Signal hypotheses $\rightarrow f(\mathbf{x}|s)$ is the probability density (*likelihood function*) that
 1853 \mathbf{x} is the set of measured values given that the events is a signal event.
- 1854 • Background hypotheses $\rightarrow f(\mathbf{x}|b)$ is the probability density (*likelihood function*)
 1855 that \mathbf{x} is the set of measured values given that the event is a background event.

1856 Figure 5.1 shows three ways to perform a classification of events for which mea-
 1857 surements of two properties, two input variables, have been performed; blue circles
 1858 represent signal events while red triangles represent background events. The classi-
 1859 fication on (a) is *cut-based* requiring $x_1 < c_1$ and $x_2 < c_2$; usually the cut values are
 1860 chosen according to some knowledge about the event process. In (b), the classification
 1861 is performed by stating a cut involving a linear function of the input variables and
 1862 so the boundary, while in (c) the the relationship between the input variables is not
 1863 linear thus the boundary is not linear either.

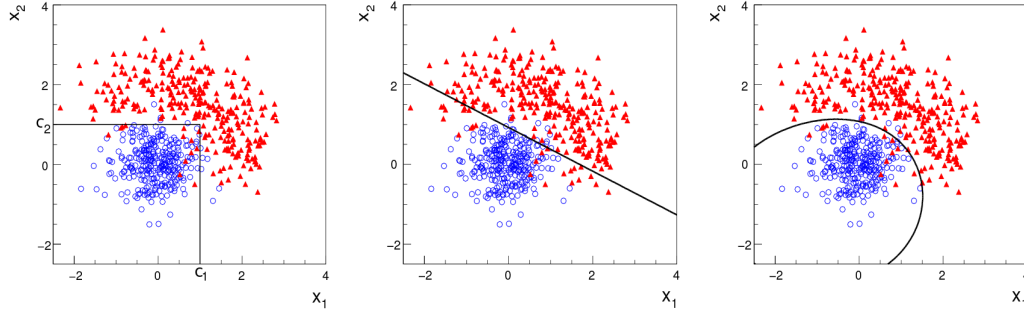


Figure 5.1: Scatter plots-MVA event classification. Distribution of two input variables x_1 and x_2 measured for a set of events; blue circles represent signal events and red triangles represent background events. The classification is based on (a) cuts, (b) linear boundary, and (c) nonlinear boundary [115]

1864 The boundary can be parametrized in terms of the input variables such that the
 1865 cut is set on the parametrization instead of on the variables, i.e., $y(\mathbf{x}) = y_{cut}$ with
 1866 y_{cut} a constant; thus, the acceptance or rejection of an event is based on what side
 1867 of the boundary is the event located. If $y(\mathbf{x})$ has functional form, it can be used to
 1868 determine the probability distribution functions $p(y|s)$ and $p(y|b)$ and then perform
 1869 a scalar test statistic with a single cut on the scalar variable y .

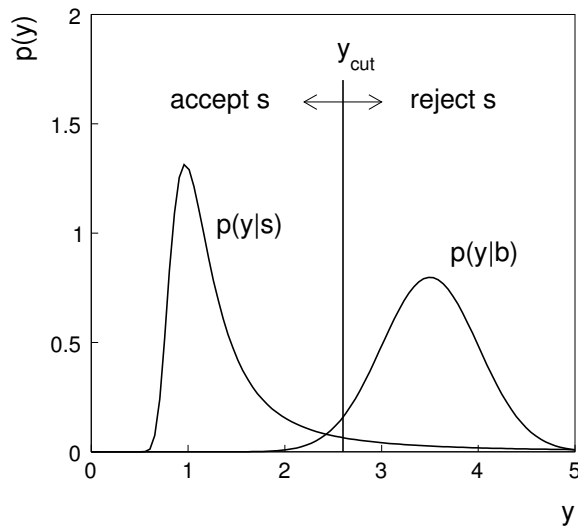


Figure 5.2: Distributions of the scalar test statistic $y(\mathbf{x})$ under the signal and background hypotheses. [115]

1870 Figure 5.2 illustrates what would be the probability distribution functions under
 1871 the signal and background hypotheses for a scalar test statistic with a cut on the
 1872 classifier y . Notice that the tails of the distributions indicate that some signal events
 1873 fall on the rejection region and some background events fall on the acceptance region;
 1874 therefore, it is convenient to define the *efficiency* with which events of a given type
 1875 are accepted, thus, the signal and background efficiencies are given by

$$\varepsilon_s = P(\text{accept event}|s) = \int_A f(\mathbf{x}|s) d\mathbf{x} = \int_{-\infty}^{y_{\text{cut}}} p(y|s) dy , \quad (5.1)$$

$$\varepsilon_b = P(\text{accept event}|b) = \int_A f(\mathbf{x}|b) d\mathbf{x} = \int_{-\infty}^{y_{\text{cut}}} p(y|b) dy , \quad (5.2)$$

1876 where A is the acceptance region. Under these conditions, the background hypothesis
 1877 corresponds to the *null hypothesis* (H_0), the signal hypothesis corresponds to the
 1878 *alternative hypothesis* (H_1), the background efficiency is the significance level of the
 1879 test, and signal efficiency is the power of the test; what is sought in an analysis is to
 1880 maximize the power of the test relative to the significance level.

1881 5.1.1 Decision trees

1882 For this thesis, the implementation of the MVA strategy, described above, is per-
 1883 formed through decision trees by using the TMVA software package [116] included in
 1884 the the ROOT analysis framework [118]. In a simple picture, a decision tree classifies
 1885 events according to their input variables values by setting a cut on each input variable
 1886 and checking which events are on which side of the cut, just as proposed in the MVA
 1887 strategy, but in addition, as a machine learning algorithm, decision trees offer the
 1888 possibility to be trained and then perform the classification efficiently.

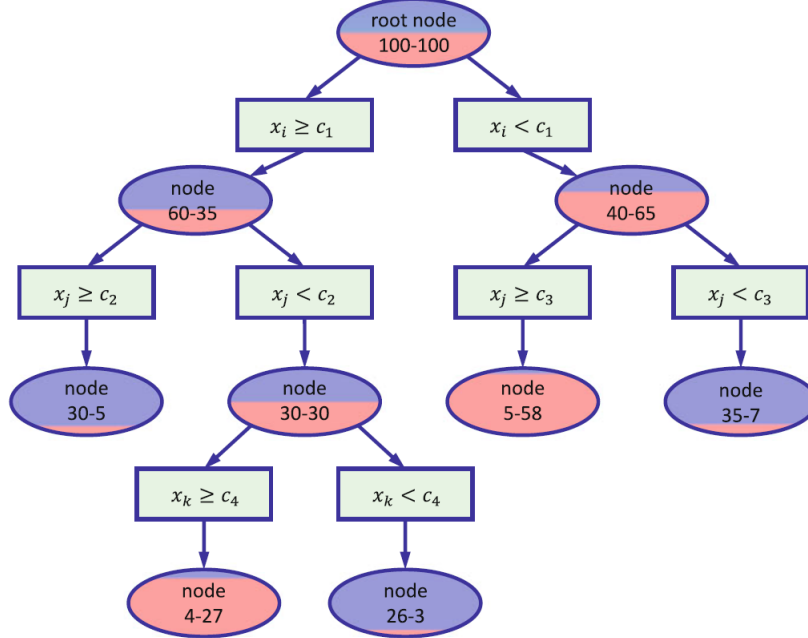


Figure 5.3: Example of a decision tree. Each node is fed with a MC sample mixing signal and background events (left-right numbers); nodes colors represent the relative amount of signal/background events [117].

1889 The training or growing of a decision tree is the process that defines the rules for
 1890 classifying events; this process is represented in figure5.3 and consist of several steps

1891 • take MC samples of signal and background events and split them into two parts
 1892 each; first parts form the training sample which will be used in the decision tree
 1893 training, while the second parts form the test sample which will be used for
 1894 testing the final classifier obtained from the training. Each event has associated
 1895 a set of input variables $\mathbf{x} = (x_1, \dots, x_n)$ which serve to distinguish between signal
 1896 and background events. The training sample is taken in at the root *node*.

1897 • pick one variable, say x_i
 1898 • pick one value of x_i , each event has its own value of x_i , and split the training
 1899 sample into two subsamples B_1 and B_2 ; B_1 contains events for which $x_i < c_1$

1900 while B_2 contains the rest of the training events;

1901 • scan all possible values of x_i and find the splitting value that provides the *best*
 1902 classification¹, i.e., B_1 is mostly made of signal events while B_2 is mostly made
 1903 of background events.

1904 • It is possible that variables other than the picked one produce a better classi-
 1905 fication, hence, all the variables have to be evaluated. Pick the next variable,
 1906 say x_j , and repeat the scan over its possible values.

1907 • At the end, all the variables and their values will have been scanned, the *best*
 1908 variable and splitting value will have been identified, say x_1, c_1 , and there will
 1909 be two nodes fed with the subsamples B_1 and B_2 .

1910 Nodes are further split by repeating the decision process until: a given number of
 1911 final nodes is obtained, nodes are largely dominated by either signal or background
 1912 events, or nodes has too few events to continue. Final nodes are called *leaves* and they
 1913 are classified as signal or background leaves according to the class of the majority of
 1914 events in them. Each *branch* in the tree corresponds to a sequence of cuts.

1915 The quality of the classification at each node is evaluated through a separation
 1916 criteria; there are several of them but the *Gini Index* (G) is the one used in the
 1917 decision trees trained for the analysis in this thesis. G is written in terms of the
 1918 purity (P), i.e. the fraction of signal events, of the samples after the separation is
 1919 made; it is given by

$$G = P(1 - P) \quad (5.3)$$

¹ Quality of the classification will be treated in the next paragraph.

1920 notice that $P=0.5$ at the root node while $G=0$ for pure leaves. For a node A split
 1921 into two nodes B_1 and B_2 the G gain is

$$\Delta G = G(A) - G(B_1) - G(B_2) \quad (5.4)$$

1922 the *best* classification corresponds to that for which the gain of G is maximized; hence,
 1923 the scanning over all event's variables and their values is of capital importance.

1924 In order to provide a numerical output for the classification, events in a sig-
 1925 nal(background) leaf are assigned an score of 1(-1) each, defining in this way the
 1926 decision tree *classifier or weak learner* as

$$f(\mathbf{x}) = \begin{cases} 1 & \mathbf{x} \text{ in signal region,} \\ -1 & \mathbf{x} \text{ in background region.} \end{cases}$$

1927 Figure 5.4 shows an example of the classification of a sample of events, containing
 1928 two variables, performed by a decision tree.

1929 5.1.2 Boosted decision trees (BDT).

1930 Event misclassification occurs when a training event ends up in the wrong leaf, i.e., a
 1931 signal event ends up in a background leaf or a background event ends up in a signal
 1932 leaf. A way to correct it is to assign a weight to the misclassified events and train
 1933 a second tree using the reweighted events; the event reweighting is performed by a
 1934 boosting algorithm, events with increased weight are known as *boosted* events, in such
 1935 a way that when used in the training of a new decision tree they get correctly classified.
 1936 The process is repeated iteratively adding a new tree to a forest and creating a set
 1937 of classifiers which are combined to create the next classifier; the final classifier offers

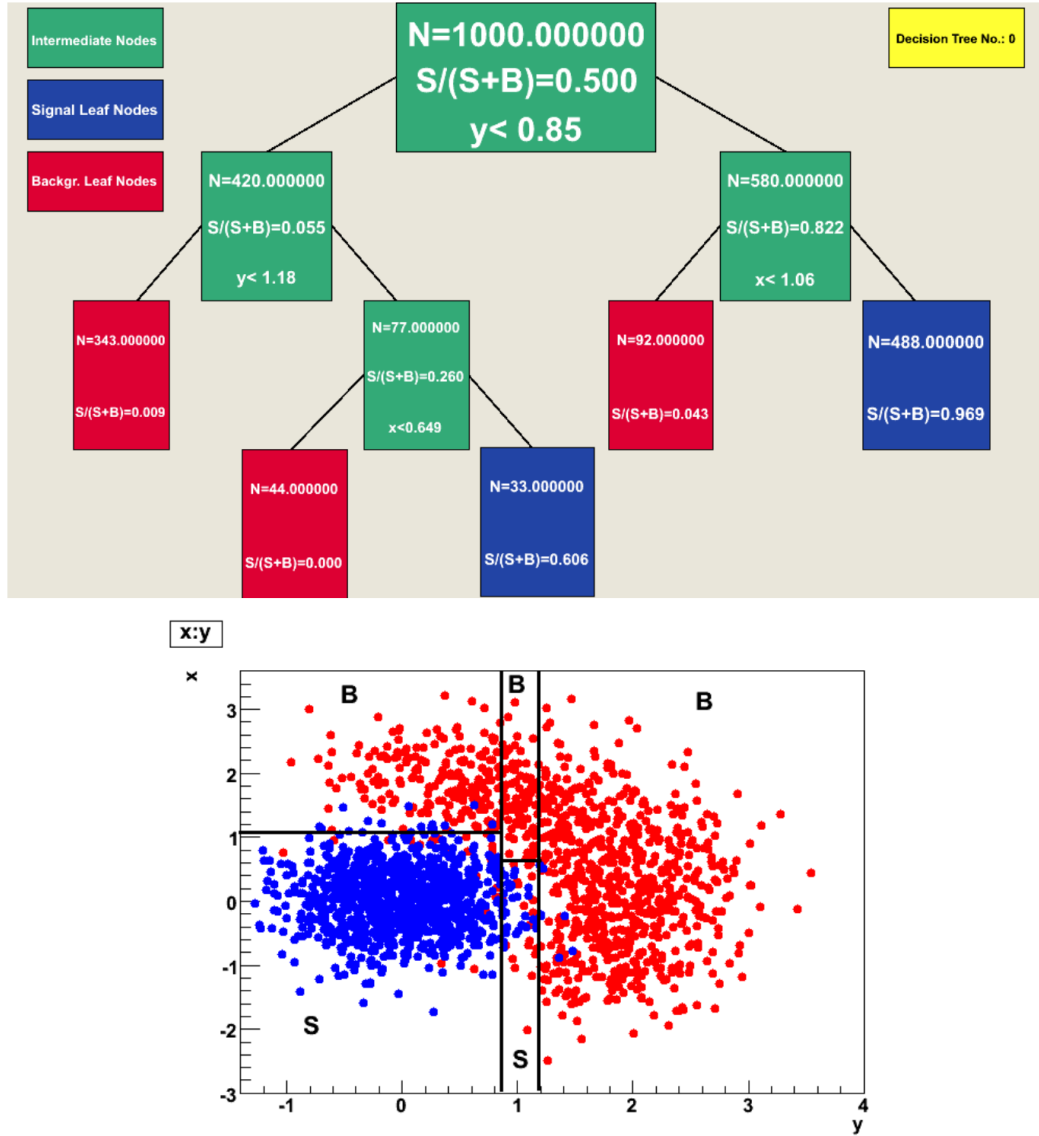


Figure 5.4: Example of a decision tree output. Each leaf, blue for signal events and red for background events, represent a region in the variables phase space [119].

1938 more stability² and has a smaller misclassification rate than any individual ones. The
 1939 resulting tree collection is known as a *boosted decision tree (BDT)*.
 1940 Thus, purity of the sample is generalized to

² Decision trees suffer from sensitivity to statistical fluctuations in the training sample which may leads to very different results with an small change in the training samples.

$$P = \frac{\sum_s w_s}{\sum_s w_s + \sum_b w_b} \quad (5.5)$$

1941 where w_s and w_b are the weights of the events; the Gini index is also generalized

$$G = \left(\sum_i^n w_i \right) P(1 - P) \quad (5.6)$$

1942 with n the number of events in the node. The final score of an event, after pass-
 1943 ing through the forest, is calculated as the renormalized sum of all the individual
 1944 (possibly weighted) scores; thus, high(low) score implies that the event is most likely
 1945 signal(background).

1946 The boosting procedure, implemented in the *Gradient boosting* algorithm used
 1947 in this thesis, produce a classifier $F(\mathbf{x})$ which is the weighted sum of the individual
 1948 classifiers obtained after each iteration,i.e.,

$$F(\mathbf{x}) = \sum_{m=1}^M \beta_m f(\mathbf{x}; a_m) \quad (5.7)$$

1949 where M is the number of trees in the forest. The *loss function* $L(F, y)$ represent the
 1950 deviation between the classifier $F(\mathbf{x})$ response and the true value y obtained from the
 1951 training sample (1 for signal events and -1 for background event), according to

$$L(F, y) = \ln(1 + e^{-2F(\mathbf{x})y}) \quad (5.8)$$

1952 thus, the reweighting is employed to ensure the minimization of the loss function;
 1953 a more detailed description of the minimization procedure can be found in reference
 1954 [120]. The final classifier output is later used as a final discrimination variable, labeled
 1955 as *BDT output/response*.

1956 **5.1.3 Overtraining.**

1957 Decision trees offer the possibility to have as many nodes as wished in order to
 1958 reduce the misclassification to zero (in theory); however, when a classifier is too much
 1959 adjusted to a particular training sample, the classifier response to a slightly different
 1960 sample may leads to a completely different classification results; this effect is know
 1961 as *overtraining*.

1962 An alternative to reduce the overtraining in BDTs consist in pruning the tree by
 1963 removing statistically insignificant nodes after the tree growing is completed but this
 1964 option is not available for BDTs with gradient boosting in the TMVA-toolkit, there-
 1965 fore, the overtraining has to be reduced by tuning the algorithm, number of nodes,
 1966 minimum number of events in the leaves, etc. The overtraining can be evaluated
 1967 by comparing the responses of the classifier when running over the training and test
 1968 samples.

1969 **5.1.4 Variable ranking.**

1970 BDTs have the couple of particular advantages related to the input variables; on one
 1971 side, they are relatively insensitive to the number of input variables used in the vector
 1972 \mathbf{x} . The ranking of the BDT input variables is determined by counting the number of
 1973 times a variable is used to split decision tree nodes; in addition, the separation gain-
 1974 squared achieved in the splitting and the number of events in the node are accounted
 1975 by applying a weighting to that number. Thus, those variables with small or no power
 1976 to separate signal and background events are rarely chosen to split the nodes,i.e., are
 1977 effectively ignored.

1978 On the other side, variables correlations play an important role for some MVA
 1979 methods like the Fisher discriminant algorithm in which the first step consist of

1980 performing a linear transformation to a phase space where the correlations between
 1981 variables are removed; in case of BDT algorithm, correlations do not affect the per-
 1982 formance.

1983 **5.1.5 BDT output example.**

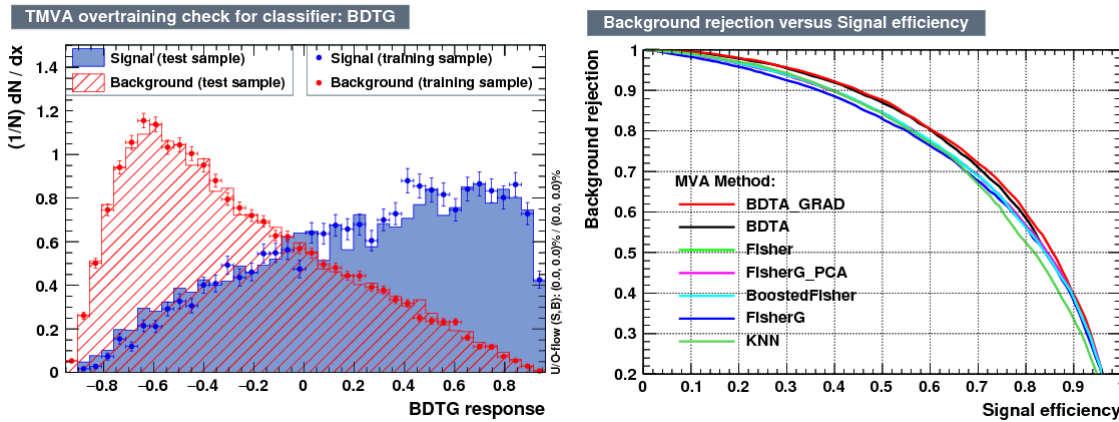


Figure 5.5: Left: Output distributions for the gradient boosted decision tree (BDTG) classifier using a sample of signal($pp \rightarrow tHq$) and background($pp \rightarrow t\bar{t}$) events. Right: Background rejection vs signal efficiency (ROC curves) for various MVA classifiers running over the same sample used to produce the plot on the left.

1984 Left side of figure 5.5 shows the BDT output distributions for signal($pp \rightarrow tHq$)
 1985 and background($pp \rightarrow t\bar{t}$) events; this plot is the equivalent to the one showed in
 1986 figure 5.2. A forest with 800 trees, maximum depth per tree = 3, and gradient
 1987 boosting have been used as training parameters. The BDTG classifier offers a good
 1988 separation power; while there is a small overtraining in the signal distribution, the
 1989 background distribution seems to be well predicted which might indicate that the
 1990 sample is composed of more background than signal events.

1991 Right side of figure 5.5 shows the background rejection vs signal efficiency curves
 1992 for several combinations of MVA classifiers-boosting algorithms; these curves are
 1993 known as ROC curves and give an indication of the performance of the classifier. The

1994 best performance is achieved with the BDTG classifier (BDTA_GRAD).

1995 5.2 Statistical inference.

1996 Once events are classified, the next step consists in finding the parameters that define
 1997 the likelihood functions $f(\mathbf{x}|s), f(\mathbf{x}|b)$ for signal and background events respectively.
 1998 In general, likelihood functions depend not only on the measurements but also on
 1999 parameters (θ_m) that define their shapes; the process of estimating these *unknown*
 2000 *parameters* and their uncertainties from the experimental data is called *inference*.
 2001 The likelihood function for N the events the in a sample is the combination of all the
 2002 likelihoods functions

$$L(\boldsymbol{\theta}) = \prod_{i=1}^N f(\mathbf{x}^i | \boldsymbol{\theta}) = \prod_{i=1}^N f(x_1^i, \dots, x_n^i; \theta_1, \dots, \theta_m) \quad (5.9)$$

2003 Thus, the estimation of the unknown parameters from experimental data samples
 2004 is written in terms of a central value using the notation

$$\theta = \hat{\theta} \pm \delta\theta \quad (5.10)$$

2005 where the interval $[\hat{\theta} + \delta\theta, \hat{\theta} - \delta\theta]$ is called *confidence interval*; it is usually inter-
 2006 preted, in the limit of infinite number of experiments, as the interval where the true
 2007 value of the unknown parameter θ is contained with a probability of 0.6827 (if no
 2008 other convention is stated).

2009 5.2.1 Nuisance parameters.

2010 The unknown parameter vector $\boldsymbol{\theta}$ is made of two types of parameters: on one side,
 2011 those parameters that provide information about the physical observables of interest

2012 for the experiment (*parameters of interest*); on the other side, the *nuisance parameters*
 2013 that are not of direct interest for the experiment but that needs to be included in
 2014 the analysis in order to achieve a satisfactory description of the data. They represent
 2015 effects of the detector response like the finite resolutions of the detection systems,
 2016 miscalibrations, and in general any source of uncertainty introduced in the analysis.

2017 In some cases the nuisance parameters are estimated using dedicated data samples,
 2018 for instance data from test beams for calibration purposes, when MC samples are
 2019 not suitable. The nuisance parameter uncertainties produce *systematic uncertainties*
 2020 while the uncertainties associated to fluctuations in data and related to the estimation
 2021 of the parameters of interest produce *statistical uncertainties*.

2022 5.2.2 Maximum likelihood estimation method

2023 The function that produce the estimate of a parameter is called *estimator*, there-
 2024 fore, estimators are usually constructed using mathematical procedures encoded in
 2025 algorithms. The estimation method used in this thesis is the *Maximum Likelihood*
 2026 *Estimation* method (MLE); it is based on the combined likelihood function defined
 2027 by eqn. 5.9 and the procedure seeks for the parameter set that corresponds to the
 2028 maximum value of the combined likelihood function, i.e., the *maximum likelihood*
 2029 *estimator* of the unknown parameter vector $\boldsymbol{\theta}$ is the function that produce the vec-
 2030 tor $\hat{\boldsymbol{\theta}}$ for which the likelihood function $L(\boldsymbol{\theta})$ evaluated at the measured sample \mathbf{x} is
 2031 maximum.

2032 Usually, the logarithm of the likelihood function is used in the numerical algo-
 2033 rithms implementations in order to avoid underflow the numerical precision of the
 2034 computers due to the product of low likelihoods. In addition, it is usual minimize the
 2035 negative logarithm of the likelihood function instead of maximizing the logarithm of

2036 it because in this way the procedure consist of differentiate a sum of therms and set
 2037 the sum to zero; therefore

$$F(\boldsymbol{\theta}) = -\ln L(\boldsymbol{\theta}) = -\sum_{i=1}^N f(\mathbf{x}^i | \boldsymbol{\theta}). \quad (5.11)$$

2038 The minimization process is performed by the software MINUIT [121] imple-
 2039 mented in the ROOT analysis framework. In case of large data samples the compu-
 2040 tational resources needed to calculate the likelihood function are too big; therefore,
 2041 the parameter estimation is performed using binned distributions of the variables of
 2042 interest for which the *binned likelihood function* is given by

$$L(data|\mu, \theta) = \prod_{i=1} \frac{(\mu s_i(\theta) + b_i(\theta))^{n_i}}{n_i!} e^{-\mu s_i(\theta) - b_i(\theta)}, \quad (5.12)$$

2043 with s_i and b_i the expected number of signal and background yields for bin i respec-
 2044 tively, n_i is the observed number of events in the bin i and $\mu = \sigma/\sigma_{SM}$ is the signal
 2045 strength. Notice that the number of entries per bin follows a Poisson distribution.
 2046 The analysis presented in this thesis is based on the binned distribution of the ratio
 2047 signal/background obtained from the BDT outputs.

2048 5.2.3 Hypothesis test

2049 The test statistic mentioned in section 5.1 involving
 2050 ; it is achieved, according to the Neyman-Pearson lemma [122],
 2051 by defining the acceptance region such that, for \mathbf{x} inside the region, the likelihood
 2052 ratio, i.e., the ratio of probability distribution functions for signal and background,

2053 **5.3 exclusion limits**

2054 **5.4 asymptotic limits**

2055 **Chapter 6**

2056 **Search for production of a Higgs**
2057 **boson and a single top quark in**
2058 **multilepton final states in pp**
2059 **collisions at $\sqrt{s} = 13 \text{ TeV}$**

2060 **6.1 Introduction**

2061 The Higgs boson discovery, supported on experimental observations and theoretical
2062 predictions made about the SM, gives the clue of the way in that elementary particles
2063 acquire mass through the Higgs mechanism; therefore, knowing the Higgs mass, the
2064 Higgs-boson and Higgs-fermion couplings can be tested. In order to test the Higgs-top
2065 coupling, several measurements have been performed, as stated in the chapter 2, but
2066 they are limited to measure the square of the coupling; however, the production of a
2067 Higgs boson in association with a single top quark (tH) not only offers access to the
2068 sign of the coupling, but also, to the CP phase of the Higgs couplings.

2069 This chapter presents the search for the associated production of a Higgs boson
 2070 and a single top quark events, focusing on leptonic signatures provided by the Higgs
 2071 decay modes to WW , ZZ , and $\tau\tau$; the 13 TeV dataset produced in 2016, which
 2072 corresponds to an integrated luminosity of 35.9fb^{-1} , is used. Constraints on the sign
 2073 of the Higgs-top coupling (y_t) have been derived from the decay rate of Higgs boson
 2074 to photon pairs [45] and from the cross section for associated production of Higgs and
 2075 Z bosons via gluon fusion [123], with recent results disfavoring negative signs of the
 2076 coupling [56, 58, 124]. It expands previous analyses performed at 8 TeV [125, 126] and
 2077 searches for associated production of $t\bar{t}$ pair and a Higgs boson in the multilepton final
 2078 state channel [127]; it also complements searches in other decay channels targeting
 2079 $H \rightarrow b\bar{b}$ [128].

2080 As shown in section 2.5, the SM cross section of the associated production of a
 2081 Higgs boson and a single top quark (tHq) process is driven by a destructive interfer-
 2082 ence between two contributions (see Figure 2.14), where the Higgs couples to either
 2083 the W boson or the top quark; however, if the sign of the Higgs-top coupling is flipped
 2084 with respect to the SM prediction, a large enhancement of the cross section occurs,
 2085 making this analysis sensitive to such deviation. A second process, where the Higgs
 2086 boson and top quark are accompanied by a W boson (tHW) has similar behavior,
 2087 albeit with a weaker interference pattern and lower contribution to the tH cross sec-
 2088 tion, therefore, a combination of both processes would increase the sensitivity; in
 2089 this analysis both contributions are combined and referred as tH channel. A third
 2090 contribution comes from $t\bar{t}H$ process. The purpose of this analysis is to investigate
 2091 the exclusion of the presence of the $tH + t\bar{t}H$ processes under the assumption of the
 2092 anomalous Higgs-top coupling modifier ($\kappa_t = -1$). The analysis exploits signatures
 2093 with two leptons of the same sign (*2lss channel*) and three leptons (*3l channel*) in
 2094 the final state.

2095 The first sections present the characteristic tHq signature as well as the expected
 2096 backgrounds. The MC samples, data sets, and the physics object definitions are
 2097 then defined. Following, the background predictions, the signal extraction, and the
 2098 statistical treatment of the selected events as well as the systematic uncertainties are
 2099 described. The final section present the results for the exclusion limits as a function
 2100 of the ratio of κ_t and the dimensionless modifier of the Higgs-vector boson κ_V .

2101 6.2 tHq signature

2102 In order to select events of tHq process, its features are translated into a set of
 2103 selection rules; figure 6.1 shows the Feynman diagram and an schematic view of the
 2104 tHq process from the pp collision to the final state configuration. A single top quark
 2105 is produced accompanied by a light quark, denoted as q ; this light quark is produced
 2106 predominantly in the forward region of the detector. The Higgs boson which can
 2107 be either emitted by the exchanged W boson or directly by the singly produced top
 2108 quark.

2109 The top quark and Higgs boson decay after their production in the detector due to
 2110 their high masses/low lifetimes. The Higgs boson is required to decay into a W boson
 2111 pair¹. The top quark almost always decays into a bottom quark and a W boson, as
 2112 encoded in the CMK matrix. The W bosons are required to decay hadronically in
 2113 the 2lss channel case and leptonically in the 3l channel case, while τ leptons are not
 2114 reconstructed separately and only their leptonic decays into either electrons or muons
 2115 are considered in this analysis.

2116 In summary, the signal process is characterized by a the final state with

- 2117 • one light-flavored forward jet,

¹ ZZ and $\tau\tau$ decays are also include in the analysis but they are not separately reconstructed

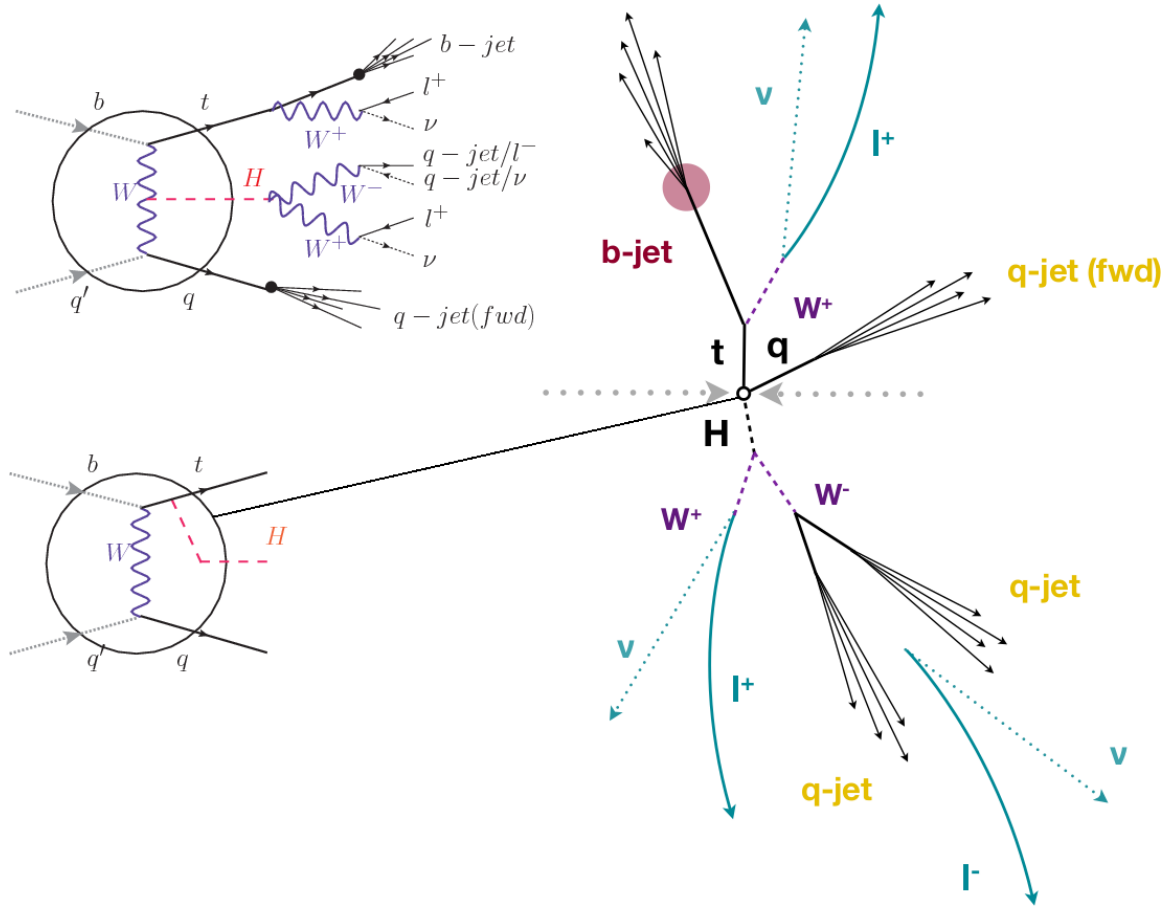


Figure 6.1: tHq event signature. Left: Feynman diagram including the whole evolution up to the final state for the case of the Higgs boson emitted by the W boson (top); Feynman diagram for the case where the Higgs boson is emitted by the top quark. Right: Schematic view as it would be seen in the detector; the circle in the Feynman diagrams on the left corresponds to the circle in the center of the schematic view as indicated by the line connecting them. In the 2lss channel, one of the W bosons from the Higgs boson decays to two light-quark jets while in the 3l channel both W bosons decays to leptons.

- 2118 • one central b-jet,
 - 2119 • 2lss channel \rightarrow two leptons of the same sign, two neutrinos and two light (often
2120 soft) jets,
 - 2121 • 3l channel \rightarrow three leptons, three neutrinos and no central light-flavored jets,
- 2122 The presence of neutrinos is inferred from the presence of MET. The analysis has

2123 been made public by CMS as a Physics Analysis Summary [129] combining the result
 2124 for the three lepton and two lepton same-sign channels. Currently, an effort to turn
 2125 the analysis into a paper is ongoing.

2126 **6.3 Background processes**

2127 The background processes are those that can mimic the signal signature or at least
 2128 can be reconstructed as that as a result of certain circumstances. The backgrounds
 2129 can be classified as

- 2130 • Irreducible backgrounds where genuine prompt leptons are produced in on-
 2131 shell W and Z boson decays; they can be reliably estimated directly from MC
 2132 simulated events, using higher-order cross sections or data control regions for
 2133 the overall normalization.
- 2134 • Reducible backgrounds where at least one of the leptons is *non-prompt*, i.e., pro-
 2135 duced within a hadronic jet, either a genuine lepton from heavy flavor decays.
 2136 misreconstructed jets, also known as *mis-ID leptons* or *fake leptons*, are consid-
 2137 ered non-prompt leptons as well. These non-prompt leptons leave tracks and
 2138 hits in the detection systems as would a prompt lepton, but correlating those
 2139 hits with nearby jets could be a way of removing them. Reducible backgrounds
 2140 are not well predicted by simulation, and are estimated using data-driven meth-
 2141 ods.

2142 The main sources of background events in the case of tHq process are $t\bar{t}$ process
 2143 and $t\bar{t} + X(X = W, Z, \gamma)$ processes, here represented together as $t\bar{t}V$ process. Figure
 2144 6.2 shows the signature for $t\bar{t}$ and $t\bar{t}W$ processes;

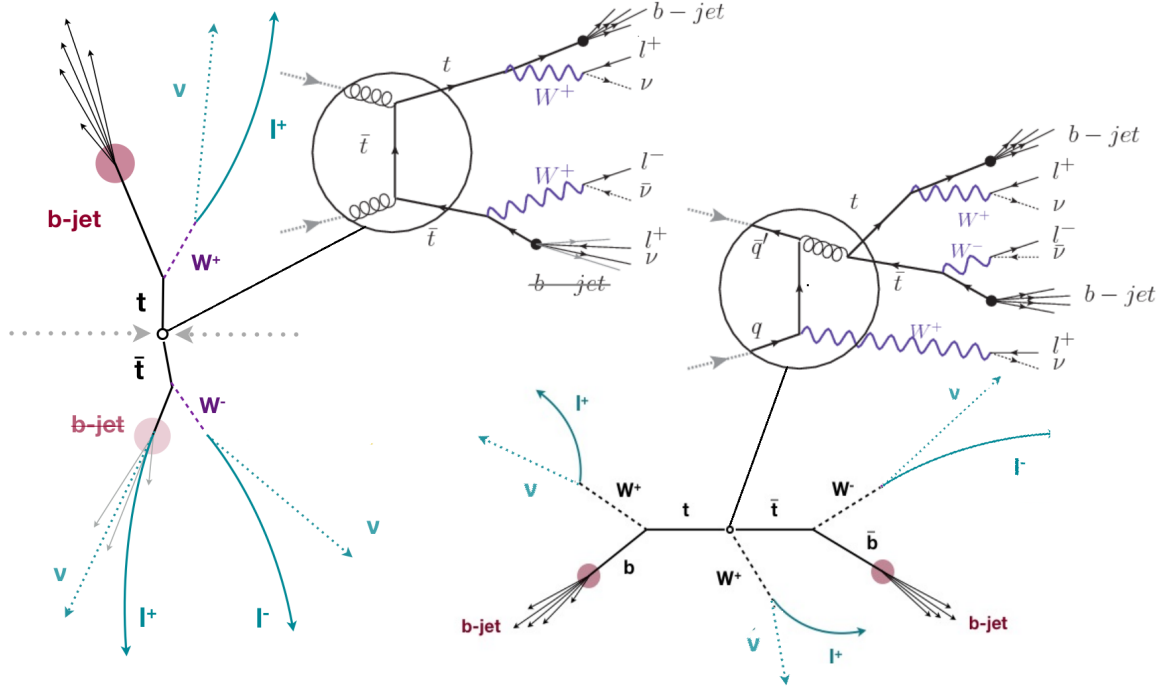


Figure 6.2: $t\bar{t}$ (left) and $t\bar{t}W$ (right) events signature as they would be seen in the detector; the Feynman diagrams including the whole evolution up to the final state are also showed. The $t\bar{t}$ process signature is very similar to that of the signal process with one fake lepton and no forward activity. The $t\bar{t}W$ process present a higher b-jet multiplicity compared to the signal process, a prompt lepton and no forward activity.

2145 The largest contribution to irreducible backgrounds involving prompt leptons
 2146 comes from $t\bar{t}W$, $t\bar{t}Z$, processes for which the number of ($b-$)jets (($b-$)jet multiplicity)
 2147 is higher than that of the signal events, while for other contributing background
 2148 events, WZ , ZZ , and rare SM processes like $W^\pm W^\pm qq$, $t\bar{t}t\bar{t}$, tZq , tZW , WWW ,
 2149 WWZ , WZZ , ZZZ , the ($b-$)jet multiplicity is lower compared to that of the signal
 2150 events. None of the irreducible backgrounds present activity in the forward region of
 2151 the detector.

2152 On the side of the reducible backgrounds, the largest contribution comes from the
 2153 $t\bar{t}$ events which have a very similar signature to the signal events but does not present
 2154 activity in the forward region of the detector either; A particular feature of the $t\bar{t}$
 2155 events is their charge-symmetry which is also a difference with the signal events.

2156 The charge misidentification plays an important role in the the 2lss channel since
 2157 leptons in processes like $t\bar{t}$ + jets or Z + jets can be charge misidentified, leading to
 2158 backgrounds increments. An identification variable have been designed in order to
 2159 reject this type of background events.

2160 6.4 Data and MC Samples

2161 Technical developments on the event generator side allow for an event-wise reweight-
 2162 ing that can change the event kinematics based on specific generation parameters.
 2163 This way not only the case of $C_t = \sqrt{2}$, but a whole range of κ_t and κ_V values can
 2164 be investigated.

2165 The data considered in this analysis were collected by the CMS experiment dur-
 2166 ing 2016 and correspond to a total integrated luminosity of $35.9 fb^{-1}$. Only periods
 2167 when the CMS magnet was on were considered when selecting the data samples, that
 2168 corresponds to the 23 Sep 2016 (Run B to G) and PromptReco (Run H) versions
 2169 of the datasets. The MC samples used in this analysis correspond to the RunI-
 2170 ISummer16MiniAODv2 campaign produced with CMSSW 80X. The two signal sam-
 2171 ples (for tHq and tHW) were produced with MG5_aMC@NLO (version 5.222), in
 2172 leading-order order mode, and are normalized to next-to-leading-order cross sections,
 2173 see Tab. 6.1. Each sample is generated with a set of event weights corresponding to
 2174 different values of κ_t and κ_V couplings as shown in Tab. 6.2.

2175 6.4.1 Full 2016 dataset and MC samples

2176 Different MC generators were used to generate the background processes. The dom-
 2177 inant sources ($t\bar{t}$, $t\bar{t}W$, $t\bar{t}Z$, $t\bar{t}H$) were produced using AMC@NLO interfaced to
 2178 PYTHIA8, and are scaled to NLO cross sections. Other processes are simulated us-

Sample	σ [pb]	BF
/THQ_Hincl_13TeV-madgraph-pythia8_TuneCUETP8M1/	0.7927	0.324
/THW_Hincl_13TeV-madgraph-pythia8_TuneCUETP8M1/	0.1472	1.0

Table 6.1: Signal samples and their cross section and branching fraction used in this analysis. See Ref. [138] for more details.

ing POWHEG interfaced to PYTHIA, or bare PYTHIA (see table 6.3 and [127] for more details).

6.4.2 Triggers

We consider online-reconstructed events triggered by one, two, or three leptons. Single-lepton triggers are included to boost the acceptance of events where the p_T of the sub-leading lepton falls below the threshold of the double-lepton triggers. Additionally, by including double-lepton triggers in the ≥ 3 lepton category, as well as single-lepton triggers in all categories, we increase the efficiency, considering the logical “or” of the trigger decisions of all the individual triggers in a given category. Tab. 6.5 shows the lowest-threshold non-prescaled triggers present in the High-Level Trigger (HLT) menus for both Monte-Carlo and data in 2016.

Trigger efficiency scale factors

The efficiency of events to pass the trigger is measured in simulation (trivially using generator information) and in the data (using event collected by an uncorrelated MET trigger). Small differences between the data and MC efficiencies are corrected by applying scale factors as shown in Tab. 6.6. The exact procedure and control plots are documented in [132] for the current analysis.

		<i>tHq</i>		<i>tHW</i>		
κ_V	κ_t	sum of weights	cross section [pb]	sum of weights	cross section [pb]	LHE weights
1.0	-3.0	35.700022	2.991	11.030445	0.6409	LHEweight_wgt[446]
1.0	-2.0	20.124298	1.706	5.967205	0.3458	LHEweight_wgt[447]
1.0	-1.5	14.043198	1.205	4.029093	0.2353	LHEweight_wgt[448]
1.0	-1.25	11.429338	0.9869	3.208415	0.1876	LHEweight_wgt[449]
1.0	-1.0		0.7927		0.1472	
1.0	-0.75	7.054998	0.6212	1.863811	0.1102	LHEweight_wgt[450]
1.0	-0.5	5.294518	0.4723	1.339886	0.07979	LHEweight_wgt[451]
1.0	-0.25	3.818499	0.3505	0.914880	0.05518	LHEweight_wgt[452]
1.0	0.0	2.627360	0.2482	0.588902	0.03881	LHEweight_wgt[453]
1.0	0.25	1.719841	0.1694	0.361621	0.02226	LHEweight_wgt[454]
1.0	0.5	1.097202	0.1133	0.233368	0.01444	LHEweight_wgt[455]
1.0	0.75	0.759024	0.08059	0.204034	0.01222	LHEweight_wgt[456]
1.0	1.0	0.705305	0.07096	0.273617	0.01561	LHEweight_wgt[457]
1.0	1.25	0.936047	0.0839	0.442119	0.02481	LHEweight_wgt[458]
1.0	1.5	1.451249	0.1199	0.709538	0.03935	LHEweight_wgt[459]
1.0	2.0	3.335034	0.2602	1.541132	0.08605	LHEweight_wgt[460]
1.0	3.0	10.516125	0.8210	4.391335	0.2465	LHEweight_wgt[461]
1.5	-3.0	45.281492	3.845	13.426212	0.7825	LHEweight_wgt[462]
1.5	-2.0	27.606715	2.371	7.809713	0.4574	LHEweight_wgt[463]
1.5	-1.5	20.476088	1.784	5.594971	0.3290	LHEweight_wgt[464]
1.5	-1.25	17.337465	1.518	4.635978	0.2749	LHEweight_wgt[465]
1.5	-1.0	14.483302	1.287	3.775902	0.2244	LHEweight_wgt[466]
1.5	-0.75	11.913599	1.067	3.014744	0.1799	LHEweight_wgt[467]
1.5	-0.5	9.628357	0.874	2.352505	0.1410	LHEweight_wgt[468]
1.5	-0.25	7.627574	0.702	1.789184	0.1081	LHEweight_wgt[469]
1.5	0.0	5.911882	0.5577	1.324946	0.08056	LHEweight_wgt[470]
1.5	0.25	4.479390	0.4365	0.959295	0.05893	LHEweight_wgt[471]
1.5	0.5	3.331988	0.3343	0.692727	0.04277	LHEweight_wgt[472]
1.5	0.75	2.469046	0.2558	0.525078	0.03263	LHEweight_wgt[473]
1.5	1.0	1.890565	0.2003	0.456347	0.02768	LHEweight_wgt[474]
1.5	1.25	1.596544	0.1689	0.486534	0.02864	LHEweight_wgt[475]
1.5	1.5	1.586983	0.1594	0.615638	0.03509	LHEweight_wgt[476]
1.5	2.0	2.421241	0.2105	1.170602	0.06515	LHEweight_wgt[477]
1.5	3.0	7.503280	0.5889	3.467546	0.1930	LHEweight_wgt[478]
0.5	-3.0	27.432685	2.260	8.929074	0.5136	LHEweight_wgt[479]
0.5	-2.0	13.956013	1.160	4.419093	0.2547	LHEweight_wgt[480]
0.5	-1.5	8.924438	0.7478	2.757611	0.1591	LHEweight_wgt[481]
0.5	-1.25	6.835341	0.5726	2.075247	0.1204	LHEweight_wgt[482]
0.5	-1.0	5.030704	0.4273	1.491801	0.08696	LHEweight_wgt[483]
0.5	-0.75	3.510528	0.2999	1.007273	0.05885	LHEweight_wgt[484]
0.5	-0.5	2.274811	0.1982	0.621663	0.03658	LHEweight_wgt[485]
0.5	-0.25	1.323555	0.1189	0.334972	0.01996	LHEweight_wgt[486]
0.5	0.0	0.656969	0.06223	0.147253	0.008986	LHEweight_wgt[487]
0.5	0.25	0.274423	0.02830	0.058342	0.003608	LHEweight_wgt[488]
0.5	0.5	0.176548	0.01778	0.068404	0.003902	LHEweight_wgt[489]
0.5	0.75	0.363132	0.03008	0.177385	0.009854	LHEweight_wgt[490]
0.5	1.0	0.834177	0.06550	0.385283	0.02145	LHEweight_wgt[491]
0.5	1.25	1.589682	0.1241	0.692099	0.03848	LHEweight_wgt[492]
0.5	1.5	2.629647	0.2047	1.097834	0.06136	LHEweight_wgt[493]
0.5	2.0	5.562958	0.4358	2.206057	0.1246	LHEweight_wgt[494]
0.5	3.0	14.843102	1.177	5.609519	0.3172	LHEweight_wgt[495]

Table 6.2: κ_V and κ_t combinations generated for the two signal samples and their NLO cross sections. The *tHq* cross section is multiplied by the branching fraction of the enforced leptonic decay of the top quark (0.324). See also Ref. [138].

Sample	σ [pb]
TTWJetsToLNu_TuneCUETP8M1_13TeV-amcatnloFXFX-madspin-pythia8	0.2043
TTZToLLNuNu_M-10_TuneCUETP8M1_13TeV-amcatnlo-pythia8	0.2529
ttHJetToNonbb_M125_13TeV_amcatnloFXFX_madspin_pythia8_mWCutfix /store/cmst3/group/susy/gpetrucc/13TeV/u/TTLL_m1to10_LO_NoMS_for76X/	0.2151 0.0283
WGToLNuG_TuneCUETP8M1_13TeV-madgraphMLM-pythia8	585.8
ZGTo2LG_TuneCUETP8M1_13TeV-amcatnloFXFX-pythia8	131.3
TGJets_TuneCUETP8M1_13TeV_amcatnlo_madspin_pythia8	2.967
TGJets_TuneCUETP8M1_13TeV_amcatnlo_madspin_pythia8	2.967
TTGJets_TuneCUETP8M1_13TeV-amcatnloFXFX-madspin-pythia8	3.697
WpWpJJ_EWK-QCD_TuneCUETP8M1_13TeV-madgraph-pythia8	0.03711
ZZZ_TuneCUETP8M1_13TeV-amcatnlo-pythia8	0.01398
WWZ_TuneCUETP8M1_13TeV-amcatnlo-pythia8	0.1651
WZZ_TuneCUETP8M1_13TeV-amcatnlo-pythia8	0.05565
WW_DoubleScattering_13TeV-pythia8	1.64
tZq_ll_4f_13TeV-amcatnlo-pythia8_TuneCUETP8M1	0.0758
ST_tWll_5f_LO_13TeV-MadGraph-pythia8	0.01123
TTTT_TuneCUETP8M1_13TeV-amcatnlo-pythia8	0.009103
WZTo3LNu_TuneCUETP8M1_13TeV-powheg-pythia8	4.4296
ZZTo4L_13TeV_powheg_pythia8	1.256
TTJets_SingleLeptFromTbar_TuneCUETP8M1_13TeV-madgraphMLM-pythia8	182.1754
TTJets_SingleLeptFromT_TuneCUETP8M1_13TeV-madgraphMLM-pythia8	182.1754
TTJets_DiLept_TuneCUETP8M1_13TeV-madgraphMLM-pythia8	87.3
DYJetsToLL_M-10to50_TuneCUETP8M1_13TeV-amcatnloFXFX-pythia8	18610
DYJetsToLL_M-50_TuneCUETP8M1_13TeV-madgraphMLM-pythia8	6024
WJetsToLNu_TuneCUETP8M1_13TeV-amcatnloFXFX-pythia8	61526.7
ST_tW_top_5f_inclusiveDecays_13TeV-powheg-pythia8_TuneCUETP8M1	35.6
ST_tW_antitop_5f_inclusiveDecays_13TeV-powheg-pythia8_TuneCUETP8M1	35.6
ST_t-channel_4f_leptonDecays_13TeV-amcatnlo-pythia8_TuneCUETP8M1	70.3144
ST_t-channel_antitop_4f_leptonDecays_13TeV-powheg-pythia8_TuneCUETP8M1	26.2278
ST_s-channel_4f_leptonDecays_13TeV-amcatnlo-pythia8_TuneCUETP8M1	3.68064
WWTo2L2Nu_13TeV-powheg	10.481

Table 6.3: List of background samples used in this analysis (CMSSW 80X). In the first section of the table are listed the samples of the processes for which we use the simulation to extract the final yields and shapes, in the second section the samples of the processes we will estimate from data. The MC simulation is used to design the data driven methods and derive the associated systematics.

Sample	σ [pb]
ttWJets_13TeV_madgraphMLM	0.6105
ttZJets_13TeV_madgraphMLM	0.5297/0.692

Table 6.4: Leading-order $t\bar{t}W$ and $t\bar{t}Z$ samples used in the signal BDT training.

Same-sign dilepton (==2 muons)
HLT_Mu17_TrkIsoVVL_Mu8_TrkIsoVVL_DZ_v*
HLT_Mu17_TrkIsoVVL_TkMu8_TrkIsoVVL_DZ_v*
HLT_IsoMu22_v*
HLT_IsoTkMu22_v*
HLT_IsoMu22_eta2p1_v*
HLT_IsoTkMu22_eta2p1_v*
HLT_IsoMu24_v*
HLT_IsoTkMu24_v*
Same-sign dilepton (==2 electrons)
HLT_Ele23_Ele12_CaloIdL_TrackIdL_IsoVL_DZ_v*
HLT_Ele27_eta2p1_WP Loose_Gsf_v*
HLT_Ele27_WPTight_Gsf_v*
HLT_Ele25_eta2p1_WPTight_Gsf_v*
Same-sign dilepton (==1 muon, ==1 electron)
HLT_Mu23_TrkIsoVVL_Ele8_CaloIdL_TrackIdL_IsoVL_v*
HLT_Mu8_TrkIsoVVL_Ele23_CaloIdL_TrackIdL_IsoVL_v*
HLT_Mu23_TrkIsoVVL_Ele8_CaloIdL_TrackIdL_IsoVL_DZ_v*
HLT_Mu8_TrkIsoVVL_Ele23_CaloIdL_TrackIdL_IsoVL_DZ_v*
HLT_IsoMu22_v*
HLT_IsoTkMu22_v*
HLT_IsoMu22_eta2p1_v*
HLT_IsoTkMu22_eta2p1_v*
HLT_IsoMu24_v*
HLT_IsoTkMu24_v*
HLT_Ele27_WPTight_Gsf_v*
HLT_Ele25_eta2p1_WPTight_Gsf_v*
HLT_Ele27_eta2p1_WP Loose_Gsf_v*
Three lepton and Four lepton
HLT_DiMu9_Ele9_CaloIdL_TrackIdL_v*
HLT_Mu8_DiEle12_CaloIdL_TrackIdL_v*
HLT_TripleMu_12_10_5_v*
HLT_Ele16_Ele12_Ele8_CaloIdL_TrackIdL_v*
HLT_Mu23_TrkIsoVVL_Ele8_CaloIdL_TrackIdL_IsoVL_v*
HLT_Mu23_TrkIsoVVL_Ele8_CaloIdL_TrackIdL_IsoVL_DZ_v*
HLT_Mu8_TrkIsoVVL_Ele23_CaloIdL_TrackIdL_IsoVL_v*
HLT_Mu8_TrkIsoVVL_Ele23_CaloIdL_TrackIdL_IsoVL_DZ_v*
HLT_Ele23_Ele12_CaloIdL_TrackIdL_IsoVL_DZ_v*
HLT_Mu17_TrkIsoVVL_Mu8_TrkIsoVVL_DZ_v*
HLT_Mu17_TrkIsoVVL_TkMu8_TrkIsoVVL_DZ_v*
HLT_IsoMu22_v*
HLT_IsoTkMu22_v*
HLT_IsoMu22_eta2p1_v*
HLT_IsoTkMu22_eta2p1_v*
HLT_IsoMu24_v*
HLT_IsoTkMu24_v*
HLT_Ele27_WPTight_Gsf_v*
HLT_Ele25_eta2p1_WPTight_Gsf_v*
HLT_Ele27_eta2p1_WP Loose_Gsf_v*

Table 6.5: Table of high-level triggers that we consider in the analysis.

Category	Scale Factor
ee	1.01 ± 0.02
e μ	1.01 ± 0.01
$\mu\mu$	1.00 ± 0.01
3l	1.00 ± 0.03

Table 6.6: Trigger efficiency scale factors and associated uncertainties, shown here rounded to the nearest percent.

2196 6.5 Object Identification

2197 In this section, the specific definitions of the physical objects in terms of the numerical
 2198 values assigned to the reconstruction parameters are presented; thus, the provided
 2199 details summarize and complement the descriptions presented in previous chapters.
 2200 The object reconstruction and selection strategy used in this thesis is inherited from
 2201 the analyses in references [127, 132], thus, the information provided in this section is
 2202 extracted from those documents unless other references are stated.

2203 6.5.1 Jets and b -jet tagging.

2204 In this analysis, jets are reconstructed by clustering PF candidates using the anti- k_t
 2205 algorithm with parameter distance $\Delta R = 0.4$; those charged hadrons that are not
 2206 consistent with the selected primary vertex are discarded from the clustering. The
 2207 jet energy is then corrected for the varying response of the detector as a function
 2208 of transverse momentum p_T and pseudorapidity η . Jets are selected for use in the
 2209 analysis only if they have $p_T > 25$ GeV and are separated from any selected leptons
 2210 by $\Delta R > 0.4$.

2211 Jets coming from the primary vertex and jets coming from pile-up vertices are
 2212 distinguished using a MVA discriminator based on the differences in the jet shapes,
 2213 in the relative multiplicity of charged and neutral components, and in the different
 2214 fraction of transverse momentum which is carried by the hardest components. Jet

2215 tracks are also required to be compatible with the primary vertex.

2216 Jets originated from the hadronization of a b quark are selected using a MVA
 2217 likelihood discriminant which uses track-based lifetime information and reconstructed
 2218 secondary vertices (CSV algorithm). Only jets within the CMS tracker acceptance
 2219 ($\eta < 2.4$) are identified with this tool. Data samples are used to measure the efficiency
 2220 of the b -jet tagging and the probability to misidentify jets from light quarks or gluons;
 2221 in both cases the measurements are parametrized as a function of the jet p_T and η
 2222 and later used to correct differences between the data and MC simulation in the b
 2223 tagging performance, by applying per-jet weights to the simulation, dependent on
 2224 the jet p_T , η , b tagging discriminator, and flavor (from simulation truth) [130]. The
 2225 per-event weight is taken as the product of the per-jet weights, including those of the
 2226 jets associated to the leptons. The weights are derived on $t\bar{t}$ and Z+jets events.

2227 Two working points are defined, based on the CSV algorithm output: *loose*' work-
 2228 ing point (CSV>0.46) with a b signal tagging efficiency of about 83% and a mistagging
 2229 rate of about 8%; and *medium* working point (CSV>0.80) with b -tagging efficiency of
 2230 about 69% and mistagging rate of order 1% [131]. Tagging of jets from charm quarks
 2231 have efficiencies of about 40% and 18% for loose and medium working points re-
 2232 spectively. Separate scale factors are applied to jets originating from bottom/charm
 2233 quarks and from light quarks in simulated events to match the tagging efficiencies
 2234 measured in the data.

2235 6.5.2 Missing Energy MET.

2236 As stated in section 4.4.1.1, the MET vector is calculated as the negative of the vector
 2237 sum of transverse momenta of all PF candidates in the event and its magnitude is
 2238 referred to as E_T^{miss} . Due to pile-up interactions, the performance in determining

2239 MET is degraded; in order to correct for that, the energy from the selected jets and
 2240 leptons that compose the event is assigned to the variable H_T^{miss} . It is calculated in
 2241 the same way as E_T^{miss} and although it has worse resolution than E_T^{miss} , it is more
 2242 robust in the sense that it does not rely on the soft part of the event. The event
 2243 selection uses a linear discriminator based on the two variables given by

$$E_T^{miss} LD = 0.00397 * E_T^{miss} + 0.00265 * H_T^{miss} \quad (6.1)$$

2244 taking advantage of the fact that the correlation between E_T^{miss} and H_T^{miss} is less
 2245 for events with instrumental missing energy than for events with real missing energy.
 2246 The working point $E_T^{miss} LD > 0.2$ was chosen to ensure a good signal efficiency while
 2247 keeping a good background rejection.

2248 6.5.3 Lepton reconstruction and identification

2249 Two types of leptons are defined in this analysis: *signal leptons* are those coming from
 2250 W, Z and τ decays which usually are isolated from other particles; *background leptons*
 2251 are defined as leptons produced in b -jet hadron decays, light-jets misidentification,
 2252 and photon conversions.

2253 The process of reconstruction and identification of electron and muon candidates
 2254 was described in chapter4, hence, the identification variables used in order to retain
 2255 the highest possible efficiency for signal leptons while maximizing the rejection of
 2256 background leptons are listed and described in the following sections ².

2257 The identification variables include not only observables related directly to the re-
 2258 constructed leptons themselves, but also to the clustered energy deposits and charged
 2259 particles in a cone around the lepton direction (jet-related variables); an initial loose

² the studies performed to optimize the identification are far from the scope of this thesis, therefore, only general descriptions are provided

2260 preselection of leptons candidates is performed and then an MVA discriminator, re-
 2261 fered to as *lepton MVA* discriminator, is used to distinguish signal leptons from
 2262 background leptons.

2263 **Muons.**

2264 The Physics Objects Groups (POG) at CMS, are in charge of studying and defining
 2265 the set of selection criteria applied on the course of reconstruction and identification
 2266 of particles. These selection criteria are implemented in the CMS framework in the
 2267 form of several object identification working points according to the strength of the
 2268 requirements.

2269 The muon candidates are reconstructed by combining information from the tracker
 2270 system and the muon detection system of CMS detector and the POG defined three
 2271 working points for muon identification *MuonID* [133];

- 2272 • *POG Loose Muon ID* is a particle identified as a muon by the PF event re-
 2273 construction and also reconstructed either as a global-muon or as an arbitrated
 2274 tracker-muon. This identification criteria is designed to be highly efficient for
 2275 prompt muons and for muons from heavy and light quark decays; it can be com-
 2276 plemented by applying impact parameter cuts in analyses with prompt muon
 2277 signals.
- 2278 • *POG Medium Muon ID* is a Loose muon with additional track-quality and
 2279 muon-quality (spatial matching between the individual measurements in the
 2280 tracker and the muon system) requirements. This identification criteria is de-
 2281 signed to be highly efficient in the separation of the muons coming from decay
 2282 in flight of heavy quarks and muons coming from B meson decays as well as
 2283 prompt muons. An additional category *MVA Prompt ID* is defined in this iden-

2284 tification criteria directed to discriminated muons from B mesons and prompt
 2285 muons (from W,Z and τ decays). The Medium ID provides the same fake rate as
 2286 the Tight Muon ID but a higher efficiency on prompt and B-decays muons. [134]

- 2287 • *POG Tight Muon ID* is a global muon with additional muon-quality require-
 2288 ments Tight Muon ID selects a subset of the PF muons.

2289 Only muons within the muon system acceptance $|\eta| < 2.4$ and minimum p_T of 5
 2290 GeV are considered.

2291 **Electrons.**

2292 Electrons are reconstructed using information from the tracker and from the electro-
 2293 magnetic calorimeter and identified by an MVA algorithm (*MVA eID* discriminant)
 2294 using the shape of the calorimetric shower variables like the shape in η and ϕ , the clus-
 2295 ter circularity, widths along η and ϕ ; track-cluster matching variables like E_{tot}/p_{in} ,
 2296 E_{Ele}/p_{out} , $\Delta\eta_{in}$, $\Delta\eta_{out}$, $\Delta\phi_{in}$, $1/E - 1/p$; and track quality variables like ξ^2 of the
 2297 GSF tracks, the number of hits used by the GSF filter [135].

2298 A loose selection based on η -dependent cuts on this discriminant is used to prese-
 2299 lect electron candidates, the full shape of the discriminant is used in the lepton MVA
 2300 selection to separate signal leptons from background leptons (described in section
 2301 6.5.3).

2302 In order to reject electrons from photon conversions, electron candidates with
 2303 missing hits in the pixel tracker layers or matched to a conversion secondary vertex
 2304 are discarded. Electrons are selected for the analysis if they have $p_T > 7$ GeV and
 2305 are located within the tracker system acceptance region ($|\eta| < 2.5$).

2306 **Lepton vertexing and pile-up rejection.**

2307 The impact parameter in the transverse plane d_0 , impact parameter along the z
 2308 axis d_z , and the impact parameter significance in the detector space SIP_{3D} , are
 2309 considered to perform the identification and rejection of pile-up, misreconstructed
 2310 tracks, and background leptons from b-hadron decays; pile-up and misreconstructed
 2311 track mitigation is achieved by imposing loose cuts on the impact parameter variables.
 2312 The full shape of the those variables is used in a lepton MVA classifier to achieve the
 2313 best separation between the signal and the background leptons.

2314 **Lepton isolation.**

2315 PF is able to recognize leptons from two different sources: on one side, leptons from
 2316 the decays of heavy particles, such as W and Z bosons, which are normally isolated
 2317 in space from the hadronic activity in the event; on the other side, leptons from the
 2318 decays of hadrons and jets misidentified as leptons, which are not isolated as the
 2319 former. For highly boosted systems, like the lepton and the b -jet generated in the
 2320 semileptonic decay of a boosted top, the decay products tend to be more closer and
 2321 sometimes they even overlap; thus, the PF standard definition of isolation in terms of
 2322 the separation between the lepton candidates and other PF objects in the η - ϕ plane,

$$\Delta R = \sqrt{(\eta^l - \eta^i)^2 + (\phi^l - \phi^i)^2} < 0.3 \quad (6.2)$$

2323 which considers all the neutral, charged hadrons and photons in a cone around the
 2324 leptons, is refocused to the local isolation of the leptons through the mini-isolation
 2325 I_{mini} [136] defined as the sum of particle flow candidates p_T within a cone around

2326 the lepton, corrected for the effects of pileup and divided by the lepton p_T

$$I_{mini} = \frac{\sum_R p_T(h^\pm) - \max\left(0, \sum_R p_T(h^0) + p_T(\gamma) - \rho \mathcal{A} \left(\frac{R}{0.3}\right)^2\right)}{p_T(l)} \quad (6.3)$$

2327 where ρ is the pileup energy density, h^\pm, h^0, γ, l , represent the charged hadron, neutral
 2328 hadrons, photons, and the lepton, respectively. The radius R of the cone depends on
 2329 the p_T of the lepton according to

$$R = \frac{10\text{GeV}}{\min(\max(p_T(l), 50\text{GeV}), 200\text{GeV})}, \quad (6.4)$$

2330 The p_T dependence of the cone size allows for greater signal efficiency. Setting a
 2331 cut on I_{mini} below a given threshold ensures that the lepton is locally isolated, even
 2332 in boosted systems. The effect of pileup is mitigated using the so-called effective area
 2333 correction \mathcal{A} listed in Table 6.7.

$ \eta $ range	$\mathcal{A}(e)$ neutral/charged	$\mathcal{A}(\mu)$ neutral/charged
0.0 - 0.8	0.1607 / 0.0188	0.1322 / 0.0191
0.8 - 1.3	0.1579 / 0.0188	0.1137 / 0.0170
1.3 - 2.0	0.1120 / 0.0135	0.0883 / 0.0146
2.0 - 2.2	0.1228 / 0.0135	0.0865 / 0.0111
2.2 - 2.5	0.2156 / 0.0105	0.1214 / 0.0091

Table 6.7: Effective areas, for electrons and muons used to mitigate the effect of pileup by using the so-called effective area correction.

2334 A loose cut on I_{mini} is applied to pre-select the muon and electron candidates;
 2335 however, the full shape is used in the lepton MVA discriminator when performing the
 2336 signal lepton selection.

2337 **Jet-related variables.**

2338 In order to reject misidentified leptons from b -jets, mostly coming from $t\bar{t}$ +jets,
 2339 Drell-Yan+jets, and W+jets events, the vertexing and isolation described in previous
 2340 sections are complemented with additional variables related to the closest recon-
 2341 structed jet to the lepton, i.e., the PF jets reconstructed³ around the leptons with
 2342 $\Delta R = \sqrt{(\eta^l - \eta^{jet})^2 + (\phi^l - \phi^{jet})^2} < 0.5$. The identification variables used in the lep-
 2343 ton MVA discriminator are the ratio p_T^l/p_T^{jet} , the CSV b-tagging discriminator value
 2344 of the jet, the number of charged tracks of the jet, and the relative p_T given by

$$p_T^{rel} = \frac{(\vec{p}_{jet} - \vec{p}_l) \cdot \vec{p}_l}{\|\vec{p}_{jet} - \vec{p}_l\|}. \quad (6.5)$$

2345 **LeptonMVA discriminator.**

2346 Electrons and muons passing the basic selection process described above are referred
 2347 to as *loose leptons*. Additional discrimination between signal leptons and background
 2348 leptons is crucial considering that the rate of $t\bar{t}$ production is much larger than the
 2349 signal, hence, an overwhelming background from $t\bar{t}$ production. To maximally ex-
 2350 ploit the available information in each event to that end, the dedicated lepton MVA
 2351 discriminator, based on a boosted decision tree (BDT) algorithm, has been built so
 2352 that all the identification variables can be used together.

2353 The lepton MVA discriminator training is performed using simulated signal Loose
 2354 leptons from the $t\bar{t}H$ MC sample and fake leptons from the $t\bar{t}$ +jets MC sample,
 2355 separately for muons and electrons. The input variables used include vertexing, iso-
 2356 lation and jet-related variables, the p_T and η of the lepton, the electron MVA eID
 2357 discriminator and the muon segment-compatibility variables. An additional require-
 2358 ment known as *tight-charge* requirement, is imposed by comparing two independent

³ charged hadrons from PU vertices are not removed prior to the jet clustering.

measurement of the charge, one from the ECAL supercluster and the other from the tracker; thus, the consistency in the measurements of the electron charge is ensured so that events with a wrong electron charge assignment are rejected; this variable is particularly used in the 2lss channel to suppress opposite-sign events for which the charge of one of the leptons has been mismeasured. The tight-charge requirement for muons is represented by the requirement of a consistently well measured track transverse momentum given by $\Delta p_T/p_T < 0.2$. Leptons are selected for the final analysis if they pass a given threshold of the BDT output, and are referred to as *tight leptons* in the following.

The validation of the lepton MVA algorithm and the lepton identification variables is performed using data in various control regions; the details about that validation are not discussed here but can be found in Reference [132].

Selection definitions

Electron and muon object identification is defined in three different sets of selections criteria; the *Loose*, *Fakeable Object*, and *Tight* selection. These three levels of selection are designed to serve for event level vetoes, the fake rate estimation application region, and the final signal selection, respectively. The p_T of fakeable objects is defined as $0.85 \times p_T(\text{jet})$, where the jet is the one associated to the lepton object. This mitigates the dependence of the fake rate on the momentum of the fakeable object and thereby improves the precision of the method.

Tables 6.8 and 6.9 list the full criteria for the different selections of muons and electrons.

In addition to the previously defined requirements for jets, they are required to be separated from any lepton candidates passing the fakeable object selections by $\Delta R > 0.4$.

Cut	Loose	Fakeable object	Tight
$ \eta < 2.4$	✓	✓	✓
p_T	$> 5\text{GeV}$	$> 15\text{GeV}$	$> 15\text{GeV}$
$ d_{xy} < 0.05$ (cm)	✓	✓	✓
$ d_z < 0.1$ (cm)	✓	✓	✓
$\text{SIP}_{3D} < 8$	✓	✓	✓
$I_{\text{mini}} < 0.4$	✓	✓	✓
is Loose Muon	✓	✓	✓
jet CSV	—	< 0.8484	< 0.8484
is Medium Muon	—	—	✓
tight-charge	—	—	✓
lepMVA > 0.90	—	—	✓

Table 6.8: Requirements on each of the three muon selections. In the cases where the cut values change between the selections, those values are listed in the table. Otherwise, whether the cut is applied is indicated.

Cut	Loose	Fakeable Object	Tight
$ \eta < 2.5$	✓	✓	✓
p_T	$> 7\text{GeV}$	$> 15\text{GeV}$	$> 15\text{GeV}$
$ d_{xy} < 0.05$ (cm)	✓	✓	✓
$ d_z < 0.1$ (cm)	✓	✓	✓
$\text{SIP}_{3D} < 8$	✓	✓	✓
$I_{\text{mini}} < 0.4$	✓	✓	✓
MVA eID $> (0.0, 0.0, 0.7)$	✓	✓	✓
$\sigma_{in\eta} < (0.011, 0.011, 0.030)$	—	✓	✓
H/E $< (0.10, 0.10, 0.07)$	—	✓	✓
$\Delta\eta_{in} < (0.01, 0.01, 0.008)$	—	✓	✓
$\Delta\phi_{in} < (0.04, 0.04, 0.07)$	—	✓	✓
$-0.05 < 1/E - 1/p < (0.010, 0.010, 0.005)$	—	✓	✓
p_T^{ratio}	—	$> 0.5^\dagger / -$	—
jet CSV	—	$< 0.3^\dagger / < 0.8484$	< 0.8484
tight-charge	—	—	✓
conversion rejection	—	—	✓
Number of missing hits	< 2	$= 0$	$= 0$
lepton MVA > 0.90	—	—	✓

Table 6.9: Criteria for each of the three electron selections. In cases where the cut values change between selections, those values are listed in the table. Otherwise, whether the cut is applied is indicated. In some cases, the cut values change for different η ranges. These ranges are $0 < |\eta| < 0.8$, $0.8 < |\eta| < 1.479$, and $1.479 < |\eta| < 2.5$ and the respective cut values are given in the form (value₁, value₂, value₃). For the two p_T^{ratio} and CSV rows, the cuts marked with a \dagger are applied to leptons that fail the lepton MVA cut, while the loose cut value is applied to those that pass the lepton MVA cut.

2384 6.5.4 Lepton selection efficiency

2385 Efficiencies of reconstruction and selecting loose leptons are measured both for muons
 2386 and electrons using a tag and probe method on both data and MC, using $Z \rightarrow \ell^+ \ell^-$
 2387 [137]. The scale factors are derived from the ratio of efficiencies $\varepsilon_i(p_T, \eta)$ measured
 2388 for a given lepton in data/MC, according to

$$\rho(p_T, \eta) = \frac{\varepsilon_{\text{data}}(p_T, \eta)}{\varepsilon_{\text{MC}}(p_T, \eta)}. \quad (6.6)$$

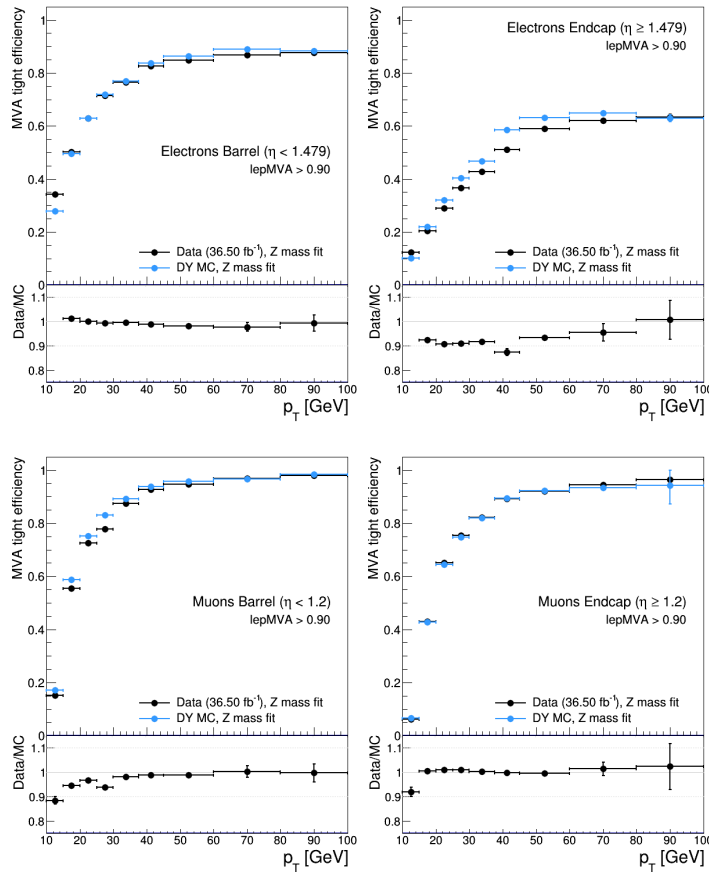


Figure 6.3: Tight vs loose selection efficiencies for electrons (top), and muons (bottom), for the 2lss definition, i.e., including the tight-charge requirement.

2389 The scale factor for each event is used to correct the weight of the event in the

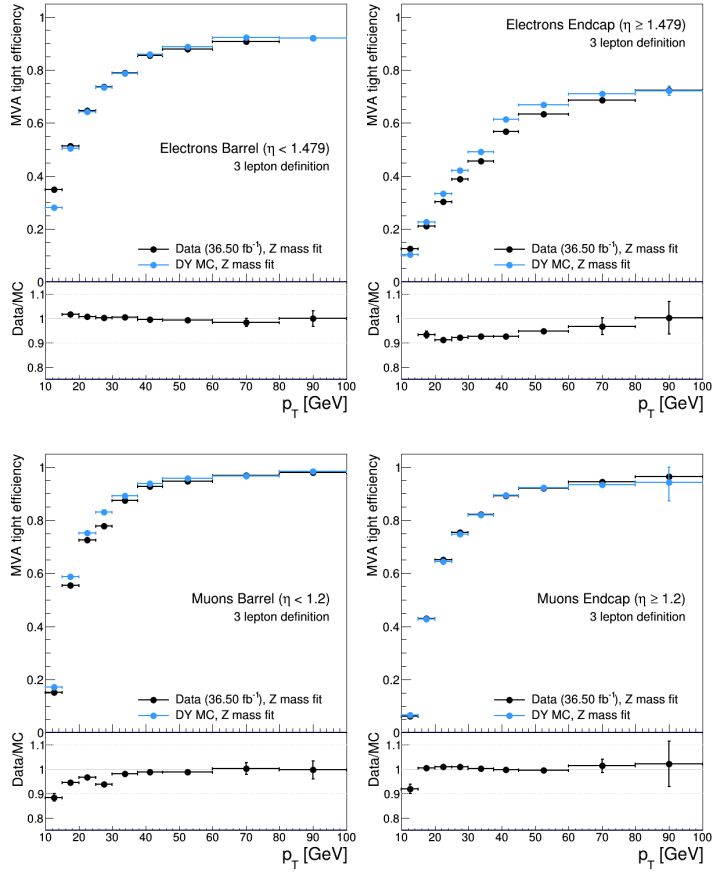


Figure 6.4: Tight vs loose selection efficiencies for electrons (top), and muons (bottom), for the 3l channel not including the tight-charge requirement.

2390 full sample; therefore, the full simulation correction is given by the product of all
 2391 the individual scale factors. The scale factors used in this thesis are inherited from
 2392 the reference [132] which in turns inherited them from leptonic SUSY analyses using
 2393 equivalent lepton selections.

2394 The efficiency of applying the tight selection as defined in Tables 6.8 and 6.9, on the
 2395 loose leptons are determined by using a tag and probe method on a sample of Drell-
 2396 Yan enriched events. Figures 6.3 and 6.4 show the efficiencies for the 2lss channel and
 2397 3l channel respectively. Efficiencies in the 2lss channel have been produced including
 2398 the tight-charge requirement, while for the 3l channel it is not included. Number

2399 of passed and failed probes are determined from a fit to the invariant mass of the
 2400 dilepton system.

2401 Simulation is corrected using these scale factors; note that they depends on η and
 2402 p_T .

2403 **6.6 Event selection**

2404 .

2405 .

2406 .

2407 .

2408 .

2409 .

2410 .

2411 .

2412 .

2413 . . .

2414 The analysis is designed to efficiently identify and select prompt leptons from
 2415 on-shell W and

2416 Z boson decays and to reject non-prompt leptons from b quark decays and spurious
 2417 lepton

2418 signatures from hadronic jets. Events are then selected in the various lepton
 2419 channels, and are

2420 required to contain hadronic jets, some of which must be consistent with b quark
 2421 hadronization. Finally, the signal yield is extracted by simultaneously fitting the
 2422 output of two dedicated

2423 multivariate discriminants (trained to separate the tHq signal from the two dom-
 2424 inant backgrounds) in all categories

2425 . Multivariate techniques are used to discriminate the signal from the dominant
 2426 backgrounds. The analysis yields a 95% confidence level (C.L.) upper limit on the
 2427 combined $tH + ttH$ production cross section times branching ratio of 0.64 pb, with
 2428 an expected limit of 0.32 pb, for a scenario with $kt = \sqrt{1.0}$ and $kV = 1.0$. Values
 2429 of kt outside the range of $\sqrt{1.25}$ to $\sqrt{1.60}$ are excluded at 95% C.L., assuming kV
 2430 $= 1.0$.

2431 Dont forget to mention previous constrains to ct check reference ?? and references
 2432 <https://link.springer.com/content/pdf/10.1007%2FJHEP01%282013%29088.pdf> (para-
 2433 graph after eq 2)

2434 We selects events with three leptons and a b -jet tagged jet in the final state. The tHq
 2435 signal contribution is then determined in a fit of the observed data to two multivariate
 2436 classifier outputs, each trained to discriminate against one of the two dominant back-
 2437 grounds of events with non-prompt leptons from $t\bar{t}$ and of associated production of $t\bar{t}$
 2438 and vector bosons ($t\bar{t}W$, $t\bar{t}Z$). The fit result is then used to set an upper limit on the
 2439 combined $t\bar{t}H$, tHq and tHW production cross section, as a function of the relative
 2440 coupling strengths of Higgs and top quark and Higgs and W boson, respectively.

2441 6.7 Background predictions

2442 The modeling of reducible and irreducible backgrounds in this analysis uses the exact
 2443 methods, analysis code, and ROOT trees used for the $t\bar{t}H$ multilepton analysis. We
 2444 give a brief description of the methods and refer to the documentation of that analysis
 2445 in Refs. [127, 132] for any details.

2446 The backgrounds in three-lepton final states can be split in two broad categories:

irreducible backgrounds with genuine prompt leptons (i.e. from on-shell W and Z boson decays); and reducible backgrounds where at least one of the leptons is “non-prompt”, i.e. produced within a hadronic jet, either a genuine lepton from heavy flavor decays, or simply mis-reconstructed jets.

Irreducible backgrounds can be reliably estimated directly from Monte-Carlo simulated events, using higher-order cross sections or data control regions for the overall normalization. This is done in this analysis for all backgrounds involving prompt leptons: $t\bar{t}W$, $t\bar{t}Z$, $t\bar{t}H$, WZ , ZZ , $W^\pm W^\pm qq$, $t\bar{t}t\bar{t}$, tZq , tZW , WWW , WWZ , WZZ , ZZZ .

Reducible backgrounds, on the other hand, are not well predicted by simulation, and are estimated using data-driven methods. In the case of non-prompt leptons, a fake rate method is used,

Additional identification criteria are applied for electrons with p_T greater than 30 GeV to mimic the identification applied at trigger level in order to ensure consistency between the measurement region and application region of the fake-rate.

where the contribution to the final selection is estimated by extrapolating from a sideband (or “application region”) with a looser lepton definition (the fakeable object definitions in Tabs. 6.8 and 6.9) to the signal selection. The tight-to-loose ratios (or “fake rates”) are measured in several background dominated data events with dedicated triggers, subtracting the residual prompt lepton contribution using MC. Non-prompt leptons in our signal regions are predominantly produced in $t\bar{t}$ events, with a much smaller contribution, from Drell–Yan production. The systematic uncertainty on the normalization of the non-prompt background estimation is on the order of 50%, and thereby one of the dominant limitations on the performance of multilepton analyses in general and this analysis in particular. It consists of several individual sources, such as the result of closure tests of the method using simulated

2473 events, limited statistics in the data control regions due to necessary prescaling of
 2474 lepton triggers, and the uncertainty in the subtraction of residual prompt leptons
 2475 from the control region.

2476 The fake background where the leptons pass the looser selection are weighted
 2477 according to how many of them fail the tight criteria. Events with a single failing
 2478 lepton are weighted with the factor $f/(1-f)$ for the estimate to the tight selection
 2479 region, where f is the fake rate. Events with two failing leptons are given the negative
 2480 weight $-f_i f_j / (1-f_i)(1-f_j)$, and for three leptons the weight is positive and equal
 2481 to the product of $f/(1-f)$ factor evaluated for each failing lepton.

2482 Figures 6.5 show the distributions of some relevant kinematic variables, normalized
 2483 to the cross section of the respective processes and to the integrated luminosity.

2484 6.8 Signal discrimination

2485 The tHq signal is separated from the main backgrounds using a boosted decision
 2486 tree (BDT) classifier, trained on simulated signal and background events. A set
 2487 of discriminating variables are given as input to the BDT which produces a output
 2488 distribution maximizing the discrimination power. Table 6.10 lists the input variables
 2489 used while Figures 6.6 show their distributions for the relevant signal and background
 2490 samples, for the three lepton channel. Two BDT classifiers are trained for the two
 2491 main backgrounds expected in the analysis: events with prompt leptons from $t\bar{t}W$ and
 2492 $t\bar{t}Z$ (also referred to as $t\bar{t}V$), and events with non-prompt leptons from $t\bar{t}$. The datasets
 2493 used in the training are the tHq signal (see Tab. 6.1), and LO MADGRAPH samples
 2494 of $t\bar{t}W$ and $t\bar{t}Z$, in an admixture proportional to their respective cross sections (see
 2495 Tab. 6.4).

2496 The MVA analysis consist of two stages: first a “training” where the MVA method

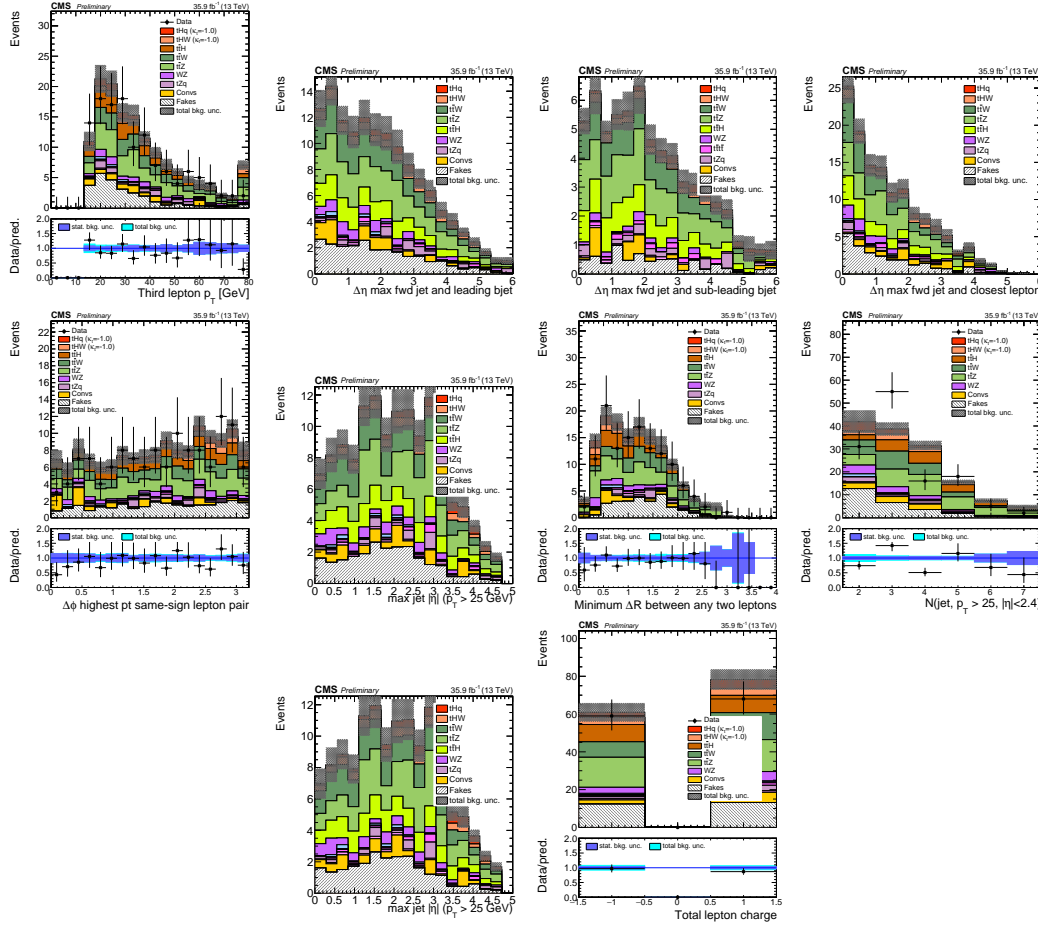


Figure 6.5: Distributions of input variables to the BDT for signal discrimination, three lepton channel, normalized to their cross section and to 35.9fb^{-1} .

is trained to discriminate between simulated signal and background events, then a “test” stage where the trained algorithm is used to classify different events from the samples. The sample is obtained from a pre-selection (see Tab. ?? with pre-selection cuts). Figures 6.7 show the input variables distributions as seen by the MVA algorithm. Note that in contrast to the distributions in Fig. 6.6 only the main backgrounds ($t\bar{t}$ from simulation, $t\bar{t}V$) are included.

Note that splitting the training in two groups reveals that some variables show opposite behavior for the two background sources; potentially screening the discrimination power if they were to be used in a single discriminant. For some other variables

Variable name	Description
nJet25	Number of jets with $p_T > 25$ GeV, $ \eta < 2.4$
MaxEtaJet25	Maximum $ \eta $ of any (non-CSV-loose) jet with $p_T > 25$ GeV
totCharge	Sum of lepton charges
nJetEta1	Number of jets with $ \eta > 1.0$, non-CSV-loose
detaFwdJetBJet	$\Delta\eta$ between forward light jet and hardest CSV loose jet
detaFwdJet2BJet	$\Delta\eta$ between forward light jet and second hardest CSV loose jet (defaults to -1 in events with only one CSV loose jet)
detaFwdJetClosestLep	$\Delta\eta$ between forward light jet and closest lepton
dphiHighestPtSSPair	$\Delta\phi$ of highest p_T same-sign lepton pair
minDRll	minimum ΔR between any two leptons
Lep3Pt/Lep2Pt	p_T of the 3 rd lepton (2 nd for ss2l)

Table 6.10: MVA input discriminating variables

2506 the distributions are similar in both background cases.

2507 From table 6.10, it is clear that the input variables are correlated to some extend.
 2508 These correlations play an important role for some MVA methods like the Fisher
 2509 discriminant method in which the first step consist of performing a linear transfor-
 2510 mation to an phase space where the correlations between variables are removed. In
 2511 case a boosted decision tree (BDT) method however, correlations do not affect the
 2512 performance. Figure 6.9 show the linear correlation coefficients for signal and back-
 2513 ground for the two training cases (the signal values are identical by construction). As
 2514 expected, strong correlations appears for variables related to the forward jet activity.
 2515 Same trend is seen in case of the same sign dilepton channel in Figure ??.

2516 6.8.1 Classifiers response

2517 Several MVA algorithms were evaluated to determine the most appropriate method
 2518 for this analysis. The plots in Fig. 6.10 (top) show the background rejection as a
 2519 function of the signal efficiency for $t\bar{t}$ and $t\bar{t}V$ trainings (ROC curves) for the different

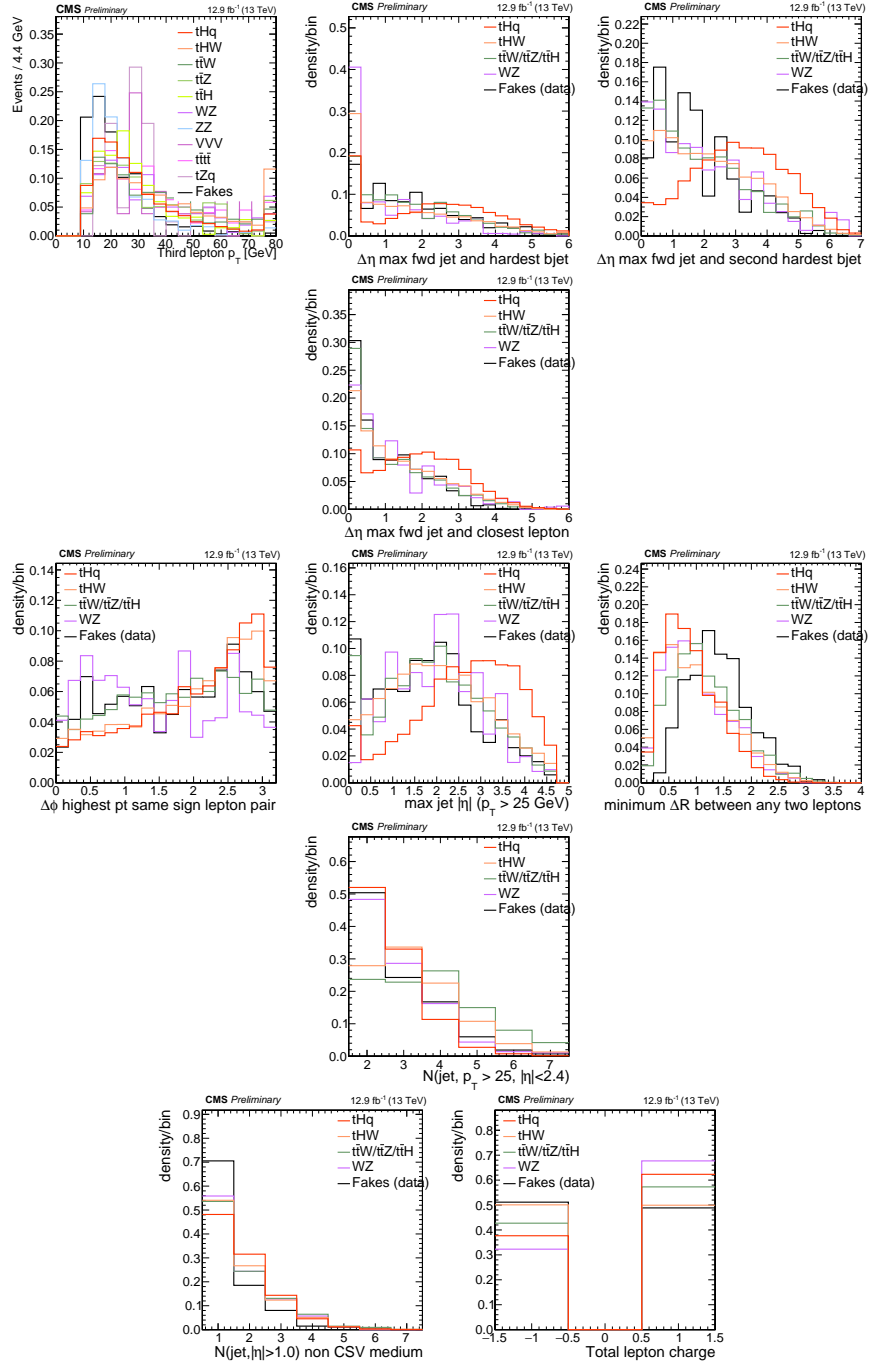


Figure 6.6: Distributions of input variables to the BDT for signal discrimination, three lepton channel.

2520 algorithms that were evaluated.

2521 In both cases the gradient boosted decision tree (“BDTA_GRAD”) classifier offers

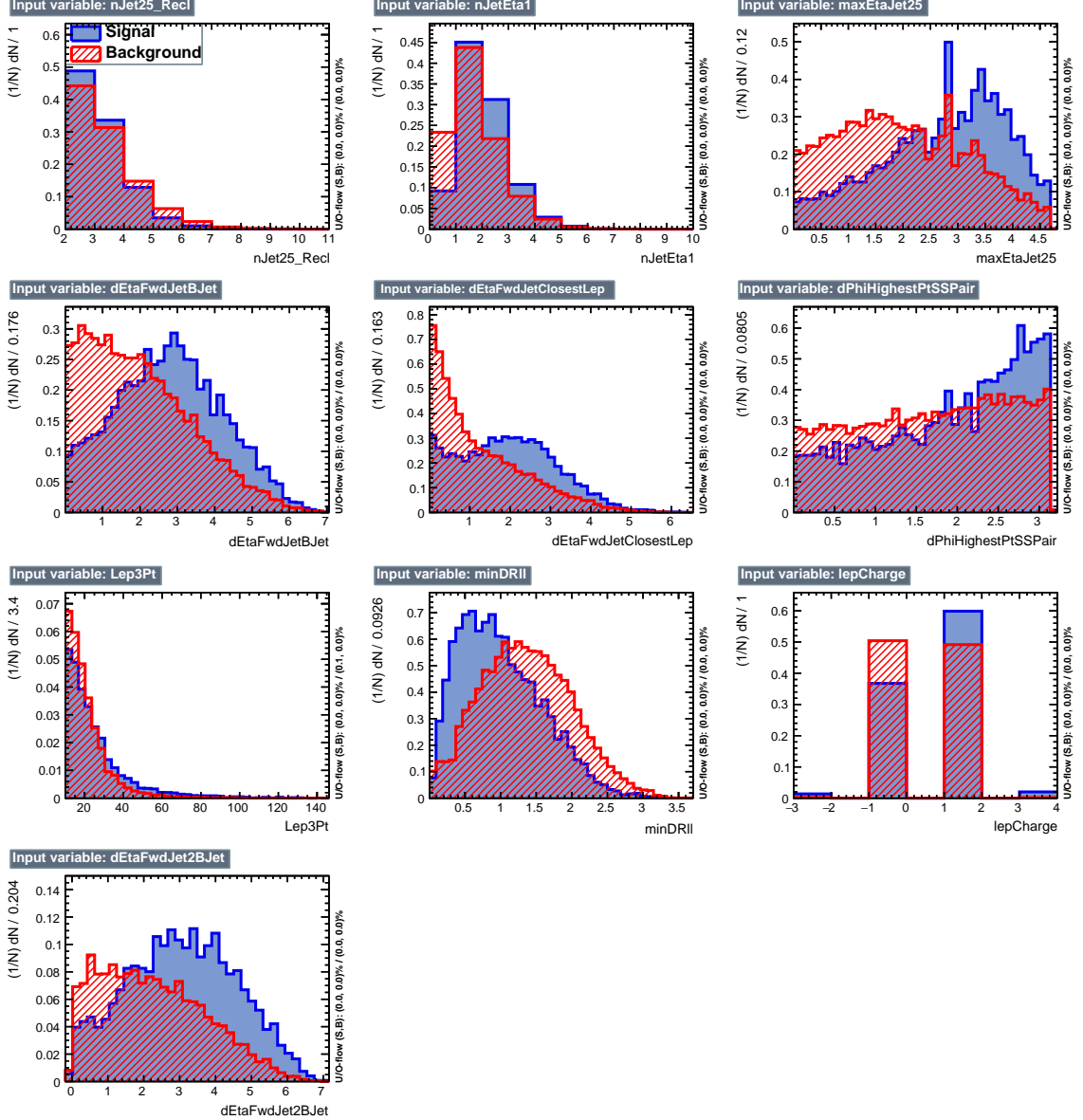


Figure 6.7: BDT inputs as seen by TMVA (signal, in blue, is tHq , background, in red, is $t\bar{t}$) for the three lepton channel, discriminated against $t\bar{t}$ (fakes) background.

the best results, followed by an adaptive BDT classifier (“BDTA”). The BDTA_GRAD classifier output distributions for signal and backgrounds are shown on the bottom of Fig. 6.10. As expected, a good discrimination power is obtained using default discriminator parameter values, with minimal overtraining. TMVA provides a ranking of the input variables by their importance in the classification process, shown in Tab. 6.11.

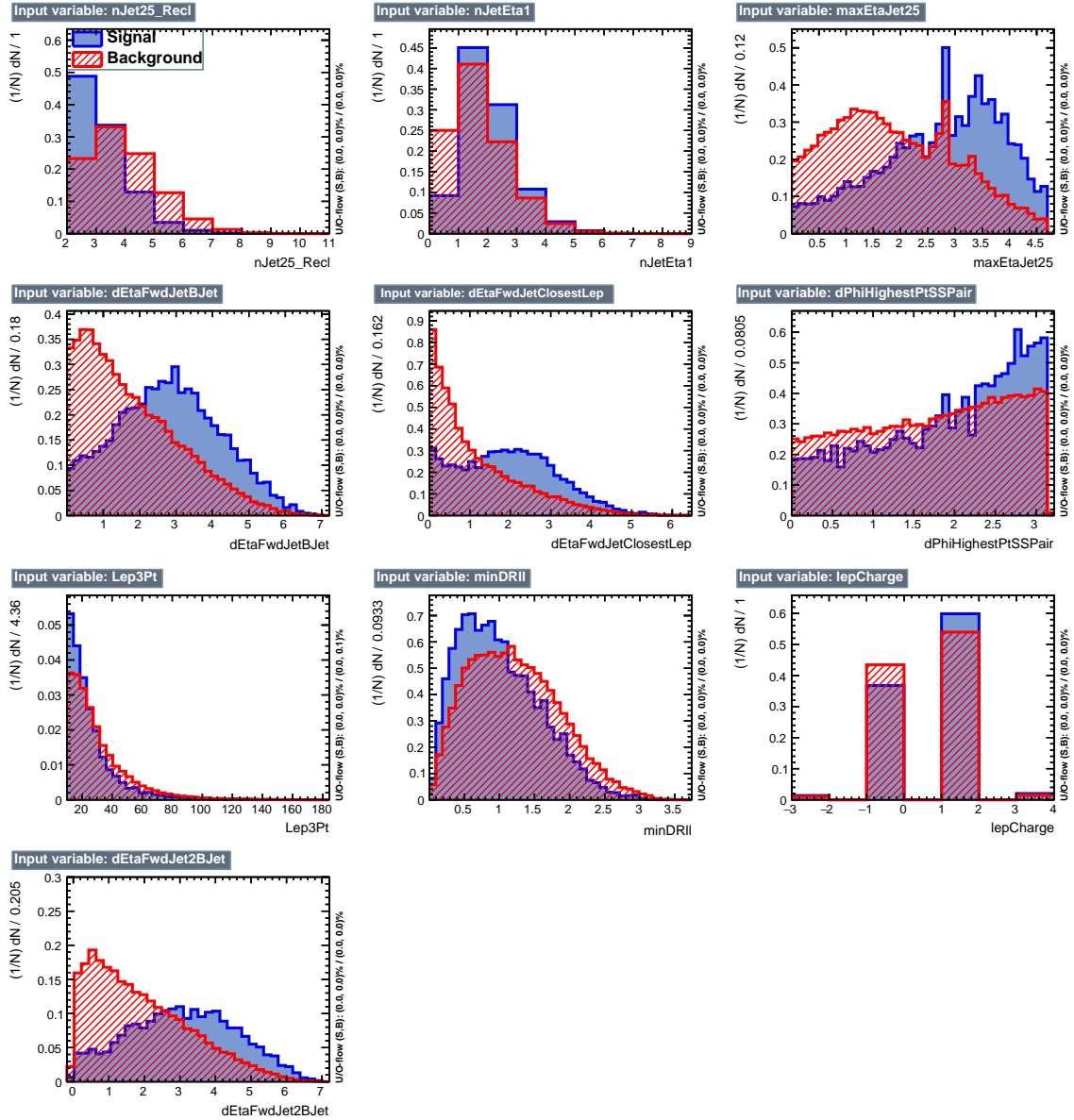


Figure 6.8: BDT inputs as seen by TMVA (signal, in blue, is tHq , background, in red, is $t\bar{t}W+t\bar{t}Z$) for the three lepton channel, discriminated against $t\bar{t}V$ background.

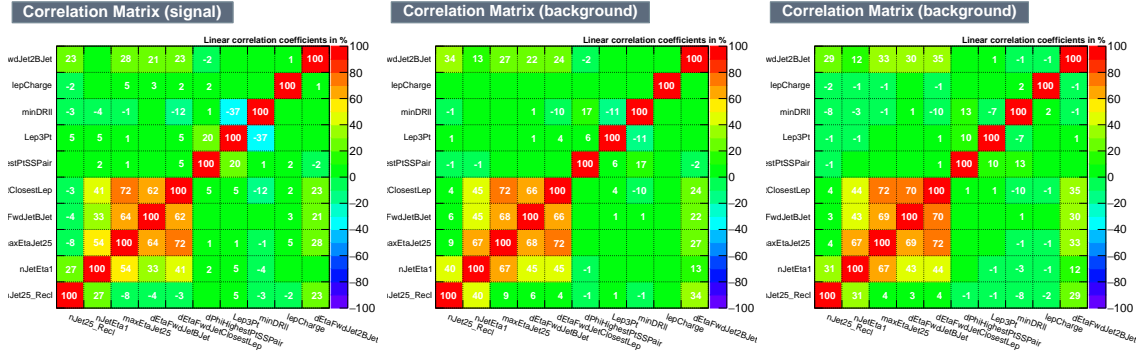


Figure 6.9: Signal (left), $t\bar{t}$ background (middle), and $t\bar{t}V$ background (right.) correlation matrices for the input variables in the TMVA analysis for the three lepton channel.

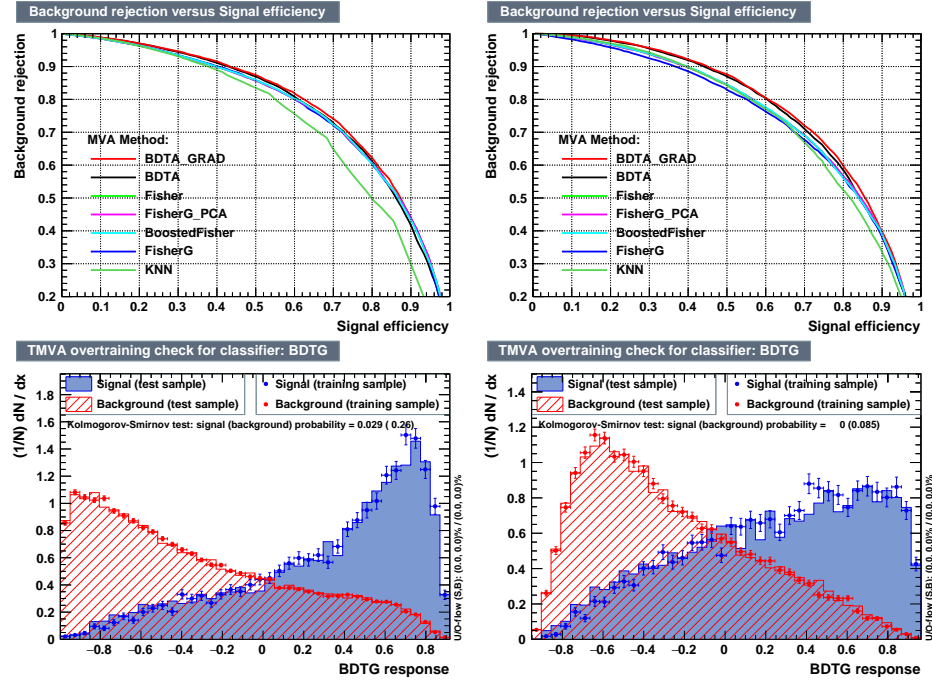


Figure 6.10: Top: background rejection vs signal efficiency (ROC curves) for various MVA classifiers (top) in the three lepton channel against $t\bar{t}V$ (left) and $t\bar{t}$ (right). Bottom: classifier output distributions for the gradient boosted decision trees, for training against $t\bar{t}V$ (left) and against $t\bar{t}$ (right).

2528 6.9 Additional discriminating variables

2529 Two additional discriminating variables were tested considering the fact that the
 2530 forward jet in the background could come from the pileup; since we have a real forward

ttbar training			ttV training		
Rank	Variable	Importance	Variable	Importance	
1	minDRll	1.329e-01	dEtaFwdJetBJet	1.264e-01	
2	dEtaFwdJetClosestLep	1.294e-01	Lep3Pt	1.224e-01	
3	dEtaFwdJetBJet	1.209e-01	maxEtaJet25	1.221e-01	
4	dPhiHighestPtSSPair	1.192e-01	dEtaFwdJet2BJet	1.204e-01	
5	Lep3Pt	1.158e-01	dEtaFwdJetClosestLep	1.177e-01	
6	maxEtaJet25	1.121e-01	minDRll	1.143e-01	
7	dEtaFwdJet2BJet	9.363e-02	dPhiHighestPtSSPair	9.777e-02	
8	nJetEta1	6.730e-02	nJet25_Recl	9.034e-02	
9	nJet25_Recl	6.178e-02	nJetEta1	4.749e-02	
10	lepCharge	4.701e-02	lepCharge	4.116e-02	

Table 6.11: TMVA input variables ranking for BDTA_GRAD method for the trainings in the three lepton channel. For both trainings the rankings show almost the same 5 variables in the first places.

```

TMVA.Types.kBDT
NTrees=800
BoostType=Grad
Shrinkage=0.10
!UseBaggedGrad
nCuts=50
MaxDepth=3
NegWeightTreatment=PairNegWeightsGlobal
CreateMVAPdfs

```

Table 6.12: TMVA configuration used in the BDT training.

jet in the signal, it could give some improvement in the discriminating power. The additional variables describe the forward jet momentum (fwdJetPt25) and the forward jet identification(fwdJetPUID). Distributions for these variables in the three lepton channel are shown in the figure 6.11. The forward jet identification distribution show that for both, signal and background, jets are mostly real jets.

The testing was made including in the MVA input one variable at a time, so we can evaluate the dicrimination power of each variable, and then both simultaneously. fwdJetPUID was ranked in the last place in importance (11) in both training (ttV and tt) while fwdJetPt25 was ranked 3 in the ttV training and 7 in the tt training. When training using 12 variables, fwdJetPt25 was ranked 5 and 7 in the ttV and tt

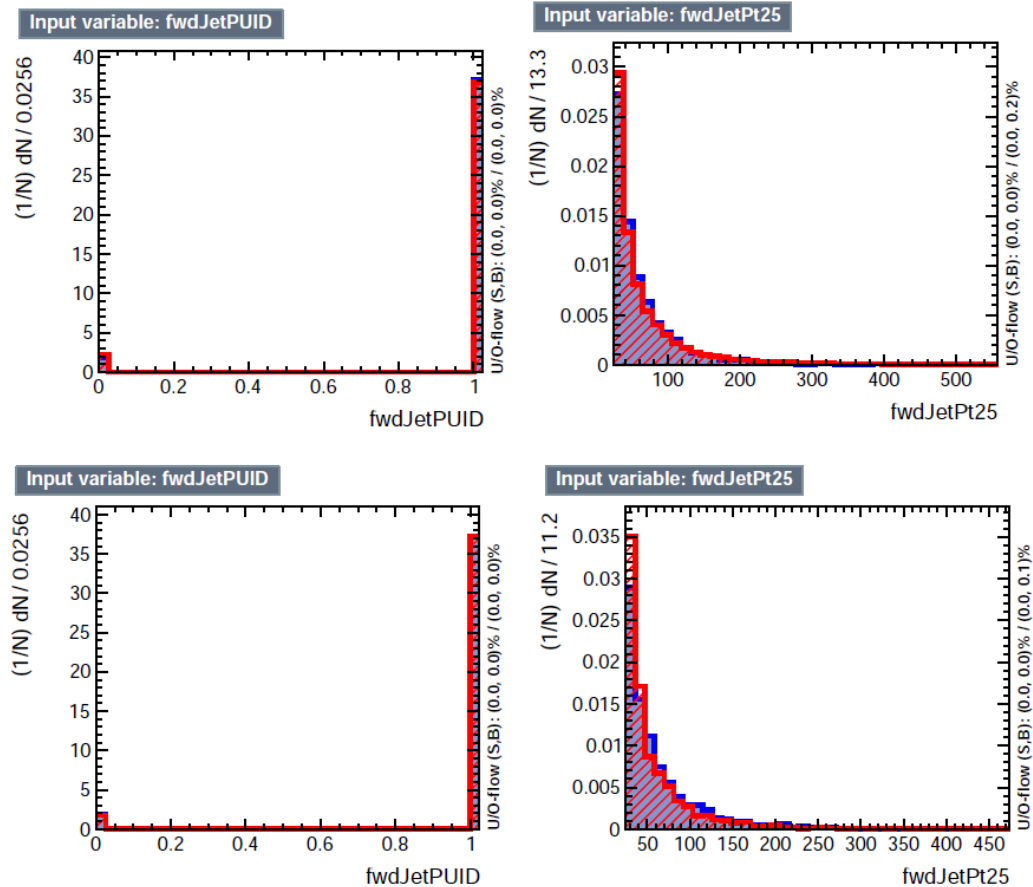


Figure 6.11: Additional discriminating variables distributions for ttv training (Top row) and tt training (bottom row) in the three lepton channel. The origin of the jets in the forward jet identification distribution is tagged as 0 for “pileup jets” while “real jets” are tagged as 1.

2541 trainings respectively, while `fwdJetPUID` was ranked 12 in both cases.

2542 The improvement in the discrimination performance provided by the additional
 2543 variables is about 1%, so it was decided not to include them in the procedure. Table
 2544 6.13 show the ROC-integral for all the testing cases we made.

ROC-integral	
base 10 var ttv	0.848
+ fwdJetPUID ttv	0.849
+ fwdJetPt25 ttv	0.856
12 var ttv	0.856
<hr/>	
base 10 var tt	0.777
+ fwdJetPUID tt	0.777
+ fwdJetPt25 tt	0.787
12 var	0.787

Table 6.13: ROC-integral for all the testing cases we made in the evaluation of the additional variables discriminating power. The improvement in the discrimination performance provided by the additional variables is about 1%

2545 **References**

- 2546 [1] J. Schwinger. "Quantum Electrodynamics. I. A Covariant Formulation". Phys-
2547 ical Review. 74 (10): 1439-61, (1948). <https://doi.org/10.1103/PhysRev.74.1439>
- 2549 [2] R. P. Feynman. "Space-Time Approach to Quantum Electrodynamics". Physical
2550 Review. 76 (6): 769-89, (1949). <https://doi.org/10.1103/PhysRev.76.769>
- 2551 [3] S. Tomonaga. "On a Relativistically Invariant Formulation of the Quantum
2552 Theory of Wave Fields". Progress of Theoretical Physics. 1 (2): 27-42, (1946).
2553 <https://doi.org/10.1143/PTP.1.27>
- 2554 [4] D.J. Griffiths, "Introduction to electrodynamics". 4th ed. Pearson, (2013).
- 2555 [5] F. Mandl, G. Shaw. "Quantum field theory." Chichester, Wiley (2009).
- 2556 [6] F. Halzen, and A.D. Martin, "Quarks and leptons: An introductory course in
2557 modern particle physics". New York: Wiley, (1984) .
- 2558 [7] File: Standard_Model_of_Elementary_Particle_dark.svg. (2017, June 12)
2559 Wikimedia Commons, the free media repository. Retrieved November 27, 2017
2560 from <https://www.collegiate-advanced-electricity.com/single-post/2017/04/10/The-Standard-Model-of-Particle-Physics>.

- 2562 [8] E. Noether, "Invariante Variationsprobleme", Nachrichten von der Gesellschaft
2563 der Wissenschaften zu Göttingen, mathematisch-physikalische Klasse, vol. 1918,
2564 pp. 235-257, (1918).
- 2565 [9] C. Patrignani et al. (Particle Data Group), Chin. Phys. C, 40, 100001 (2016)
2566 and 2017 update.
- 2567 [10] M. Goldhaber, L. Grodzins, A.W. Sunyar "Helicity of Neutrinos", Phys. Rev.
2568 109, 1015 (1958).
- 2569 [11] Palanque-Delabrouille N et al. "Neutrino masses and cosmology with Lyman-
2570 alpha forest power spectrum", JCAP 11 011 (2015).
- 2571 [12] M. Gell-Mann. "A Schematic Model of Baryons and Mesons". Physics Letters.
2572 8 (3): 214-215 (1964).
- 2573 [13] G. Zweig. "An SU(3) Model for Strong Interaction Symmetry and its Breaking"
2574 (PDF). CERN Report No.8182/TH.401 (1964).
- 2575 [14] G. Zweig. "An SU(3) Model for Strong Interaction Symmetry and its Breaking:
2576 II" (PDF). CERN Report No.8419/TH.412(1964).
- 2577 [15] M. Gell-Mann. "The Interpretation of the New Particles as Displaced Charged
2578 Multiplets". Il Nuovo Cimento 4: 848. (1956).
- 2579 [16] T. Nakano, K. Nishijima. "Charge Independence for V-particles". Progress of
2580 Theoretical Physics 10 (5): 581-582. (1953).
- 2581 [17] N. Cabibbo, "Unitary symmetry and leptonic decays" Physical Review Letters,
2582 vol. 10, no. 12, p. 531, (1963).

- 2583 [18] M.Kobayashi, T.Maskawa, “CP-violation in the renormalizable theory of weak
2584 interaction,” Progress of Theoretical Physics, vol. 49, no. 2, pp. 652-657, (1973).
- 2585 [19] File: Weak Decay (flipped).svg. (2017, June 12). Wikimedia Com-
2586 mons, the free media repository. Retrieved November 27, 2017 from
2587 [https://commons.wikimedia.org/w/index.php?title=File:Weak_Decimal_\(flipped\)](https://commons.wikimedia.org/w/index.php?title=File:Weak_Decimal_(flipped).svg&oldid=247498592)
2588 .svg&oldid=247498592.
- 2589 [20] Georgia Tech University. Coupling Constants for the Fundamental
2590 Forces(2005). Retrieved January 10, 2018, from <http://hyperphysics.phy->
2591 astr.gsu.edu/hbase/Forces/couple.html#c2
- 2592 [21] M. Strassler. (May 31, 2013).The Strengths of the Known Forces. Retrieved Jan-
2593 uary 10, 2018, from <https://profmattstrassler.com/articles-and-posts/particle->
2594 physics-basics/the-known-forces-of-nature/the-strength-of-the-known-forces/
- 2595 [22] S.L. Glashow. “Partial symmetries of weak interactions”, Nucl. Phys. 22 579-
2596 588, (1961).
- 2597 [23] A. Salam, J.C. Ward. “Electromagnetic and weak interactions”, Physics Letters
2598 13 168-171, (1964).
- 2599 [24] S. Weinberg, “A model of leptons”, Physical Review Letters, vol. 19, no. 21, p.
2600 1264, (1967).
- 2601 [25] M. Peskin, D. Schroeder, “An introduction to quantum field theory”. Perseus
2602 Books Publishing L.L.C., (1995).
- 2603 [26] A. Pich. “The Standard Model of Electroweak Interactions”
2604 <https://arxiv.org/abs/1201.0537>

- 2605 [27] G. Arnison et al. (UA1 Collaboration), Phys. Lett. B 122, 103 (1983).
- 2606 [28] M. Banner et al. (UA2 Collaboration), Phys. Lett. B 122, 476 (1983).
- 2607 [29] G. Arnison et al. (UA1 Collaboration), Phys. Lett. B 126, 398 (1983).
- 2608 [30] P. Bagnaia et al. (UA2 Collaboration), Phys. Lett. B 129, 130 (1983).
- 2609 [31] F.Bellaiche. (2012, 2 September). “What’s this Higgs boson anyway?”. Retrieved
2610 from: <https://www.quantum-bits.org/?p=233>
- 2611 [32] M. Endres et al. Nature 487, 454-458 (2012) doi:10.1038/nature11255
- 2612 [33] F. Englert, R. Brout. “Broken Symmetry and the Mass of Gauge
2613 Vector Mesons”. Physical Review Letters. 13 (9): 321-23.(1964)
2614 doi:10.1103/PhysRevLett.13.321
- 2615 [34] P.Higgs. “Broken Symmetries and the Masses of Gauge Bosons”. Physical Re-
2616 view Letters. 13 (16): 508-509,(1964). doi:10.1103/PhysRevLett.13.508.
- 2617 [35] G.Guralnik, C.R. Hagen and T.W.B. Kibble. “Global Conservation Laws
2618 and Massless Particles”. Physical Review Letters. 13 (20): 585-587, (1964).
2619 doi:10.1103/PhysRevLett.13.585.
- 2620 [36] CMS collaboration. “Observation of a new boson at a mass of 125 GeV with
2621 the CMS experiment at the LHC”. Physics Letters B. 716 (1): 30-61 (2012).
2622 arXiv:1207.7235. doi:10.1016/j.physletb.2012.08.021
- 2623 [37] ATLAS collaboration. “Observation of a New Particle in the Search for the Stan-
2624 dard Model Higgs Boson with the ATLAS Detector at the LHC”. Physics Letters
2625 B. 716 (1): 1-29 (2012). arXiv:1207.7214. doi:10.1016/j.physletb.2012.08.020.

- 2626 [38] ATLAS collaboration; CMS collaboration (26 March 2015). “Combined Mea-
 2627 surement of the Higgs Boson Mass in pp Collisions at $\sqrt{s}=7$ and 8 TeV with
 2628 the ATLAS and CMS Experiments”. Physical Review Letters. 114 (19): 191803.
 2629 arXiv:1503.07589. doi:10.1103/PhysRevLett.114.191803.
- 2630 [39] LHC InternationalMasterclasses“When protons collide”. Retrieved from http://atlas.physicsmasterclasses.org/en/zpath_protoncollisions.htm
- 2632 [40] CMS Collaboration, “SM Higgs Branching Ratios and Total Decay Widths (up-
 2633 date in CERN Report4 2016)”. <https://twiki.cern.ch/twiki/bin/view/LHCPhysics/CERNYellowReportPageBR> , last accessed on 17.12.2017.
- 2635 [41] R.Grant V. “Determination of Higgs branching ratios in $H \rightarrow W^+W^- \rightarrow l\nu jj$
 2636 and $H \rightarrow ZZ \rightarrow l^+l^-jj$ channels”. Physics Department, University of Ten-
 2637 nessee (Dated: October 31, 2012). Retrieved from <http://aesop.phys.utk.edu/ph611/2012/projects/Riley.pdf>
- 2639 [42] LHC Higgs Cross Section Working Group, Denner, A., Heinemeyer, S. et al.
 2640 “Standard model Higgs-boson branching ratios with uncertainties”. Eur. Phys.
 2641 J. C (2011) 71: 1753. <https://doi.org/10.1140/epjc/s10052-011-1753-8>
- 2642 [43] D. de Florian et al., LHC Higgs Cross Section Working Group,
 2643 CERNâš2017âš002-M, arXiv:1610.07922[hep-ph] (2016).
- 2644 [44] F. Maltoni, K. Paul, T. Stelzer, and S. Willenbrock, “Associated production
 2645 of Higgs and single top at hadron colliders”, Phys.Rev. D64 (2001) 094023,
 2646 [hep-ph/0106293].

- 2647 [45] S. Biswas, E. Gabrielli, F. Margaroli, and B. Mele, “Direct constraints on the
 2648 top-Higgs coupling from the 8 TeV LHC data,” Journal of High Energy Physics,
 2649 vol. 07, p. 073, (2013).
- 2650 [46] M. Farina, C. Grojean, F. Maltoni, E. Salvioni, and A. Thamm, “Lifting de-
 2651 generacies in Higgs couplings using single top production in association with a
 2652 Higgs boson,” Journal of High Energy Physics, vol. 05, p. 022, (2013).
- 2653 [47] T.M. Tait and C.-P. Yuan, “Single top quark production as a window to physics
 2654 beyond the standard model”, Phys. Rev. D 63 (2000) 014018 [hep-ph/0007298].
- 2655 [48] F. Demartin, F. Maltoni, K. Mawatari, and M. Zaro, “Higgs production in
 2656 association with a single top quark at the LHC,” European Physical Journal C,
 2657 vol. 75, p. 267, (2015).
- 2658 [49] CMS Collaboration, “Modelling of the single top-quark production in associa-
 2659 tion with the Higgs boson at 13 TeV.” [https://twiki.cern.ch/twiki/bin/](https://twiki.cern.ch/twiki/bin/viewauth/CMS/SingleTopHiggsGeneration13TeV)
 2660 [viewauth/CMS/SingleTopHiggsGeneration13TeV](#), last accessed on 16.01.2018.
- 2661 [50] CMS Collaboration, “SM Higgs production cross sections at $\sqrt{s} =$
 2662 13 TeV.” [https://twiki.cern.ch/twiki/bin/view/LHCPhysics/](https://twiki.cern.ch/twiki/bin/view/LHCPhysics/CERNYellowReportPageAt13TeV)
 2663 [CERNYellowReportPageAt13TeV](#), last accessed on 16.01.2018.
- 2664 [51] S. Dawson, The effective W approximation, Nucl. Phys. B 249 (1985) 42.
- 2665 [52] S. Biswas, E. Gabrielli and B. Mele, JHEP 1301 (2013) 088 [arXiv:1211.0499
 2666 [hep-ph]].
- 2667 [53] F. Demartin, B. Maier, F. Maltoni, K. Mawatari, and M. Zaro, “tWH associated
 2668 production at the LHC”, European Physical Journal C, vol. 77, p. 34, (2017).
 2669 arXiv:1607.05862

- 2670 [54] LHC Higgs Cross Section Working Group, “Handbook of LHC Higgs Cross
 2671 Sections: 4.Deciphering the Nature of the Higgs Sector”, arXiv:1610.07922.
- 2672 [55] J. Ellis, D. S. Hwang, K. Sakurai, and M. Takeuchi.“Disentangling Higgs-Top
 2673 Couplings in Associated Production”, JHEP 1404 (2014) 004, [arXiv:1312.5736].
- 2674 [56] CMS Collaboration, V. Khachatryan et al., “Precise determination of the mass
 2675 of the Higgs boson and tests of compatibility of its couplings with the standard
 2676 model predictions using proton collisions at 7 and 8 TeV,” arXiv:1412.8662.
- 2677 [57] ATLAS Collaboration, G. Aad et al., “Updated coupling measurements of the
 2678 Higgs boson with the ATLAS detector using up to 25 fb^{-1} of proton-proton
 2679 collision data”, ATLAS-CONF-2014-009.
- 2680 [58] ATLAS and CMS Collaborations, “Measurements of the Higgs boson produc-
 2681 tion and decay rates and constraints on its couplings from a combined ATLAS
 2682 and CMS analysis of the LHC pp collision data at $\sqrt{s} = 7$ and 8 TeV,” (2016).
 2683 CERN-EP-2016-100, ATLAS-HIGG-2015-07, CMS-HIG-15-002.
- 2684 [59] File:Cern-accelerator-complex.svg. Wikimedia Commons,
 2685 the free media repository. Retrieved January, 2018 from
 2686 <https://commons.wikimedia.org/wiki/File:Cern-accelerator-complex.svg>
- 2687 [60] J.L. Caron , “Layout of the LEP tunnel including future LHC infrastructures.”,
 2688 (Nov, 1993). A C Collection. Legacy of AC. Pictures from 1992 to 2002. Re-
 2689 trieved from <https://cds.cern.ch/record/841542>
- 2690 [61] M. Vretenar, “The radio-frequency quadrupole”. CERN Yellow Report CERN-
 2691 2013-001, pp.207-223 DOI:10.5170/CERN-2013-001.207. arXiv:1303.6762
- 2692 [62] L.Evans. P. Bryant (editors). “LHC Machine”. JINST 3 S08001 (2008).

- 2693 [63] CERN Photographic Service.“Radio-frequency quadrupole, RFQ-1”, March
2694 1983, CERN-AC-8303511. Retrieved from <https://cds.cern.ch/record/615852>.
- 2695 [64] CERN Photographic Service “Animation of CERN’s accelerator net-
2696 work”, 14 October 2013. DOI: 10.17181/cds.1610170 Retrieved from
2697 <https://videos.cern.ch/record/1610170>
- 2698 [65] C.Sutton. “Particle accelerator”.Encyclopedia Britannica. July 17, 2013. Re-
2699 trieved from <https://www.britannica.com/technology/particle-accelerator>.
- 2700 [66] L.Guiraud. “Installation of LHC cavity in vacuum tank.”. July 27 2000. CERN-
2701 AC-0007016. Retrieved from <https://cds.cern.ch/record/41567>.
- 2702 [67] J.L. Caron, “Magnetic field induced by the LHC dipole’s superconducting coils”.
2703 March 1998. AC Collection. Legacy of AC. Pictures from 1992 to 2002. LHC-
2704 PHO-1998-325. Retrieved from <https://cds.cern.ch/record/841511>
- 2705 [68] AC Team. “Diagram of an LHC dipole magnet”. June 1999. CERN-DI-9906025
2706 retrieved from <https://cds.cern.ch/record/40524>.
- 2707 [69] CMS Collaboration “Public CMS Luminosity Information”.
2708 <https://twiki.cern.ch/twiki/bin/view/CMSPublic/LumiPublicResults#2016>
2709 _proton_proton_13_TeV_collis, last accessed 24.01.2018
- 2710 [70] J.L Caron. “LHC Layout” AC Collection. Legacy of AC. Pictures
2711 from 1992 to 2002. September 1997, LHC-PHO-1997-060. Retrieved from
2712 <https://cds.cern.ch/record/841573>.
- 2713 [71] J.A. Coarasa. “The CMS Online Cluster:Setup, Operation and Maintenance
2714 of an Evolving Cluster”. ISGC 2012, 26 February - 2 March 2012, Academia
2715 Sinica, Taipei, Taiwan.

- 2716 [72] CMS Collaboration. “The CMS experiment at the CERN LHC” JINST 3 S08004
2717 (2008).
- 2718 [73] CMS Collaboration. “CMS detector drawings 2012” CMS-PHO-GEN-2012-002.
2719 Retrieved from <http://cds.cern.ch/record/1433717>.
- 2720 [74] R. Breedon. “View through the CMS detector during the cooldown of the
2721 solenoid on February 2006. CMS Collection”, February 2006, CMS-PHO-
2722 OREACH-2005-004, Retrieved from <https://cds.cern.ch/record/930094>.
- 2723 [75] A. Dominguez et. al. “CMS Technical Design Report for the Pixel Detector
2724 Upgrade”, CERN-LHCC-2012-016. CMS-TDR-11.
- 2725 [76] CMS Collaboration. “Description and performance of track and primary-vertex
2726 reconstruction with the CMS tracker,” Journal of Instrumentation, vol. 9, no.
2727 10, p. P10009,(2014).
- 2728 [77] CMS Collaboration and M. Brice. “Images of the CMS Tracker Inner
2729 Barrel”, November 2008, CMS-PHO-TRACKER-2008-002. Retrieved from
2730 <https://cds.cern.ch/record/1431467>.
- 2731 [78] M. Weber. “The CMS tracker”. 6th international conference on hyperons, charm
2732 and beauty hadrons Chicago, June 28-July 3 2004.
- 2733 [79] CMS Collaboration. “Projected Performance of an Upgraded CMS Detector at
2734 the LHC and HL-LHC: Contribution to the Snowmass Process”. Jul 26, 2013.
2735 arXiv:1307.7135
- 2736 [80] L. Veillet. “End assembly of HB with EB rails and rotation in-
2737 side SX ”,January 2002. CMS-PHO-HCAL-2002-002. Retrieved from
2738 <https://cds.cern.ch/record/42594>.

- 2739 [81] J. Puerta-Pelayo.“First DT+RPC chambers installation round in the
2740 UX5 cavern.”. January 2007, CMS-PHO-OREACH-2007-001. Retrieved from
2741 <https://cds.cern.ch/record/1019185>
- 2742 [82] X. Cid Vidal and R. Cid Manzano. “CMS Global Muon Trigger” web
2743 site: Taking a closer look at LHC. Retrieved from https://www.lhc-closer.es/taking_a_closer_look_at_lhc/0.lhc_trigger
2744
- 2745 [83] WLCG Project Office, “Documents & Reference - Tiers - Structure,” (2014).
2746 <http://wlcg.web.cern.ch/documents-reference> , last accessed on 30.01.2018.
- 2747 [84] CMS Collaboration. “CMSSW Application Framework”,
2748 <https://twiki.cern.ch/twiki/bin/view/CMSPublic/WorkBookCMSSWFramework>,
2749 last accesses 06.02.2018
- 2750 [85] A. Buckleya, J. Butterworthb, S. Giesekec, et. al. “General-purpose event gen-
2751 erators for LHC physics”. arXiv:1101.2599v1 [hep-ph] 13 Jan 2011
- 2752 [86] A. Quadt. “Top Quark Physics at Hadron Colliders”. Advances in the Physics
2753 of Particles and Nuclei. Springer-Verlag Berlin Heidelberg. DOI: 10.1007/978-
2754 3-540-71060-8 (2007)
- 2755 [87] DurhamHep Data Project, “The Durham HepData Project - PDF Plotter.”
2756 <http://hepdata.cedar.ac.uk/pdf/pdf3.html> , last accessed on 02.02.2018.
- 2757 [88] F. Maltoni, G. Ridolfi, and M. Ubiali, “b-initiated processes at the LHC: a
2758 reappraisal,” Journal of High Energy Physics, vol. 07, p. 022, (2012).
- 2759 [89] B. Andersson, G. Gustafson, G. Ingelman and T. Sjostrand, “Parton fragmen-
2760 tation and string dynamics”, Physics Reports, Vol. 97, No. 2-3, pp. 31-145,
2761 1983.

- 2762 [90] CMS Collaboration, “Event generator tunes obtained from underlying event
2763 and multiparton scattering measurements;” European Physical Journal C, vol.
2764 76, no. 3, p. 155, (2016).
- 2765 [91] J. Alwall et. al., “The automated computation of tree-level and next-to-leading
2766 order differential cross sections, and their matching to parton shower simula-
2767 tions,” Journal of High Energy Physics, vol. 07, p. 079, (2014).
- 2768 [92] S. Frixione, P. Nason, and C. Oleari, “Matching NLO QCD computations with
2769 Parton Shower simulations: the POWHEG method,” Journal of High Energy
2770 Physics, vol. 11, p. 070, (2007).
- 2771 [93] S. Agostinelli et al., “GEANT4: A Simulation toolkit,” Nuclear Instruments
2772 and Methods in Physics, vol. A506, pp. 250–303, (2003).
- 2773 [94] J.Allison et.al.,“Recent developments in Geant4”, Nuclear Instruments and
2774 Methods in Physics Research A 835 (2016) 186-225.
- 2775 [95] CMS Collaboration “Full Simulation Offline Guide”, <https://twiki.cern.ch/twiki/bin/view/CMSPublic/SWGuideSimulation>, last accessed 04.02.2018
- 2777 [96] A. Giammanco. “The Fast Simulation of the CMS Experiment” J. Phys.: Conf.
2778 Ser. 513 022012 (2014)
- 2779 [97] A.M. Sirunyan et. al. “Particle-flow reconstruction and global event description
2780 with the CMS detector”, JINST 12 P10003 (2017) <https://doi.org/10.1088/1748-0221/12/10/P10003>.
- 2782 [98] The CMS Collaboration. “ Description and performance of track and pri-
2783 mary vertex reconstruction with the CMS tracker”. JINST 9 P10009 (2014).
2784 doi:10.1088/1748-0221/9/10/P10009

- 2785 [99] J. Incandela. “Status of the CMS SM Higgs Search” July 4, 2012. Pdf slides.
2786 Retrieved from https://indico.cern.ch/event/197461/contributions/1478917/attachments/290954/406673/CMS_4July2012_Final.pdf
- 2788 [100] P. Billoir and S. Qian, “Simultaneous pattern recognition and track fitting by
2789 the Kalman filtering method”, Nucl. Instrum. Meth. A 294 219. (1990).
- 2790 [101] W. Adam, R. Fruhwirth, A. Strandlie and T. Todorov, “Reconstruction of
2791 electrons with the Gaussian sum filter in the CMS tracker at LHC”, eConf
2792 C 0303241 (2003) TULT009 [physics/0306087].
- 2793 [102] K. Rose, “Deterministic Annealing for Clustering, Compression, Classification,
2794 Regression and related Optimisation Problems”, Proc. IEEE 86 (1998) 2210.
- 2795 [103] R. Fruhwirth, W. Waltenberger and P. Vanlaer, “ Adaptive Vertex Fitting”,
2796 CMS Note 2007-008 (2007).
- 2797 [104] CMS collaboration, “Performance of CMS muon reconstruction in pp collision
2798 events at $\sqrt{s} = 7$ TeV ”, JINST 7 P10002 2012, [arXiv:1206.4071].
- 2799 [105] M. Cacciari, G. P. Salam, and G. Soyez, “The anti- k_t jet clustering algorithm,”
2800 Journal of High Energy Physics, vol. 04, p. 063, (2008).
- 2801 [106] B. Dorney. “Anatomy of a Jet in CMS”. Quantum Diaries. June
2802 1st, 2011. Retrieved from <https://www.quantumdiaries.org/2011/06/01/anatomy-of-a-jet-in-cms/>
- 2804 [107] The CMS Collaboration.“Event Displays from the high-energy collisions at 7
2805 TeV”, May 2010, CMS-PHO-EVENTS-2010-007, Retrieved from <https://cds.cern.ch/record/1429614>.

- 2807 [108] The CMS collaboration. “Determination of jet energy calibration and transverse
2808 momentum resolution in CMS”. JINST 6 P11002 (2011). <http://dx.doi.org/10.1088/1748-0221/6/11/P11002>
- 2810 [109] The CMS Collaboration, “Introduction to Jet Energy Corrections at
2811 CMS.”. <https://twiki.cern.ch/twiki/bin/view/CMS/IntroToJEC>, last ac-
2812 cessed 10.02.2018.
- 2813 [110] CMS Collaboration Collaboration. “Identification of b quark jets at the CMS
2814 Experiment in the LHC Run 2”. Tech. rep. CMS-PAS-BTV-15-001. Geneva:
2815 CERN, (2016). <https://cds.cern.ch/record/2138504>.
- 2816 [111] CMS Collaboration Collaboration. “Performance of missing energy reconstruc-
2817 tion in 13 TeV pp collision data using the CMS detector”. Tech. rep. CMS-PAS-
2818 JME16-004. Geneva: CERN, 2016. <https://cds.cern.ch/record/2205284>.
- 2819 [112] CMS Collaboration, “New CMS results at Moriond (Electroweak) 2013”,
2820 Retrieved from http://cms.web.cern.ch/sites/cms.web.cern.ch/files/styles/large/public/field/image/HIG13004_Event01_0.png?itok=L AwZzPHR
- 2823 [113] CMS Collaboration, “New CMS results at Moriond (Electroweak) 2013”,
2824 Retrieved from http://cms.web.cern.ch/sites/cms.web.cern.ch/files/styles/large/public/field/image/TOP12035_Event01.png?itok=uMdnSqzC
- 2827 [114] K. Skovpen. “Event displays highlighting the main properties of heavy flavour
2828 jets in the CMS Experiment”, Aug 2017, CMS-PHO-EVENTS-2017-006. Re-
2829 trieved from <https://cds.cern.ch/record/2280025>.

- 2830 [115] G. Cowan. “Topics in statistical data analysis for high-energy physics”.
2831 arXiv:1012.3589v1
- 2832 [116] A. Hoecker et al., “TMVA-Toolkit for multivariate data analysis”
2833 arXiv:physics/0703039v5 (2009)
- 2834 [117] L. Lista. “Statistical Methods for Data Analysis in Particle Physics”, 2nd
2835 ed. Springer International Publishing. (2017) <https://dx.doi.org/10.1007/978-3-319-62840-0>
- 2837 [118] I. Antcheva et al., “ROOT-A C++ framework for petabyte data storage, sta-
2838 tistical analysis and visualization ,” Computer Physics Communications, vol.
2839 182, no. 6, pp. 1384–1385, (2011).
- 2840 [119] Y. Coadou. “Boosted decision trees”, ESIPAP, Archamps, 9 Febru-
2841 ary 2016. Lecture. Retrieved from https://indico.cern.ch/event/472305/contributions/1982360/attachments/1224979/1792797/ESIPAP_MVA160208-BDT.pdf
- 2844 [120] J.H. Friedman. “Greedy function approximation: A gradient boosting ma-
2845 chine”. Ann. Statist. Volume 29, Number 5 (2001), 1189-1232. https://projecteuclid.org/download/pdf_1/euclid-aos/1013203451.
- 2847 [121] F. James, M. Roos, “MINUIT: Function minimization and error analysis”. Cern
2848 Computer Centre Program Library, Geneve Long Write-up No. D506, 1989
- 2849 [122] J. Neyman and E. S. Pearson, “On the problem of the most efficient tests
2850 of statistical hypotheses”. Philosophical Transactions of the Royal Society of
2851 London. Series A, Containing Papers of a Mathematical or Physical Character.
2852 Vol. 231 (1933), pp. 289-337

- 2853 [123] B. Hespel, F. Maltoni, and E. Vryonidou, “Higgs and Z boson associated pro-
 2854 duction via gluon fusion in the SM and the 2HDM”, JHEP 06 (2015) 065,
 2855 [https://dx.doi.org/10.1007/JHEP06\(2015\)065](https://dx.doi.org/10.1007/JHEP06(2015)065), arXiv:1503.01656.
- 2856 [124] ATLAS Collaboration, “Measurements of Higgs boson produc-
 2857 tion and couplings in diboson final states with the ATLAS
 2858 detector at the LHC”, Phys. Lett. B726 (2013) 88–119,
 2859 doi:10.1016/j.physletb.2014.05.011,10.1016/j.physletb.2013.08.010,
 2860 arXiv:1307.1427. [Erratum: Phys. Lett.B734,406(2014)].
- 2861 [125] CMS Collaboration, “Search for the associated production of a Higgs boson
 2862 with a single top quark in proton-proton collisions at $\sqrt{s} = 8$ TeV”, JHEP 06
 2863 (2016) 177,doi:10.1007/JHEP06(2016)177, arXiv:1509.08159.
- 2864 [126] B. Stieger, C. Jorda Lope et al., “Search for Associated Production of a Single
 2865 Top Quark and a Higgs Boson in Leptonic Channels”, CMS Analysis Note CMS
 2866 AN-14-140, 2014.
- 2867 [127] M. Peruzzi, C. Mueller, B. Stieger et al., “Search for ttH in multilepton final
 2868 states at $\sqrt{s} = 13$ TeV”, CMS Analysis Note CMS AN-16-211, 2016.
- 2869 [128] CMS Collaboration, “Search for H to bbar in association with a single top quark
 2870 as a test of Higgs boson couplings at $\sqrt{s} = 13$ TeV”, CMS Physics Analysis
 2871 Summary CMS-PAS-HIG-16-019, 2016.
- 2872 [129] CMS Collaboration, “Search for production of a Higgs boson and a single top
 2873 quark in multilepton final states in proton collisions at $\sqrt{s} = 13$ TeV”, CMS
 2874 Physics Analysis Summary CMS-PAS-HIG-17-005, 2016.

- 2875 [130] B. WG, “BtagRecommendation80XReReco”, February, 2017. <https://twiki.cern.ch/twiki/bin/view/CMS/BtagRecommendation80XReReco>.
- 2876
- 2877 [131] CMS Collaboration, “Identification of b quark jets at the CMS Experiment
2878 in the LHC Run 2”, CMS Physics Analysis Summary CMS-PAS-BTV-15-001,
2879 2016.
- 2880 [132] M. Peruzzi, F. Romeo, B. Stieger et al., “Search for ttH in multilepton final
2881 states at $\sqrt{s} = 13$ TeV”, CMS Analysis Note CMS AN-17-029, 2017.
- 2882 [133] CMS Collaboration, “Baseline muon selections for Run-II.” <https://twiki.cern.ch/twiki/bin/view/CMSPublic/SWGuideMuonIdRun2>, last accessed on
2883 24.02.2018.
- 2884
- 2885 [134] G. Petrucciani and C. Botta, “Two step prompt muon identification”, January,
2886 2015. <https://indico.cern.ch/event/368007/contribution/2/material/slides/0.pdf>.
- 2887
- 2888 [135] H. Brun and C. Ochando, “Updated Results on MVA eID with 13 TeV samples”,
2889 October, 2014. <https://indico.cern.ch/event/298249/contribution/3/material/slides/0.pdf>.
- 2890
- 2891 [136] K. Rehermann and B. Tweedie, “Efficient Identification of Boosted Semileptonic
2892 Top Quarks at the LHC”, JHEP 03 (2011) 059, [https://dx.doi.org/10.1007/JHEP03\(2011\)059](https://dx.doi.org/10.1007/JHEP03(2011)059), arXiv:1007.2221.
- 2893
- 2894 [137] CMS Collaboration. “Tag and Probe”, <https://twiki.cern.ch/twiki/bin/view/CMSPublic/TagAndProbe>, last accessed on 02.03.2018.
- 2895
- 2896 [138] B. Maier, “SingleTopHiggProduction13TeV”, February, 2016.
2897 <https://twiki.cern.ch/twiki/bin/viewauth/CMS/SingleTopHiggsGeneration13TeV>.
- 2898